III-2

Material Sciences

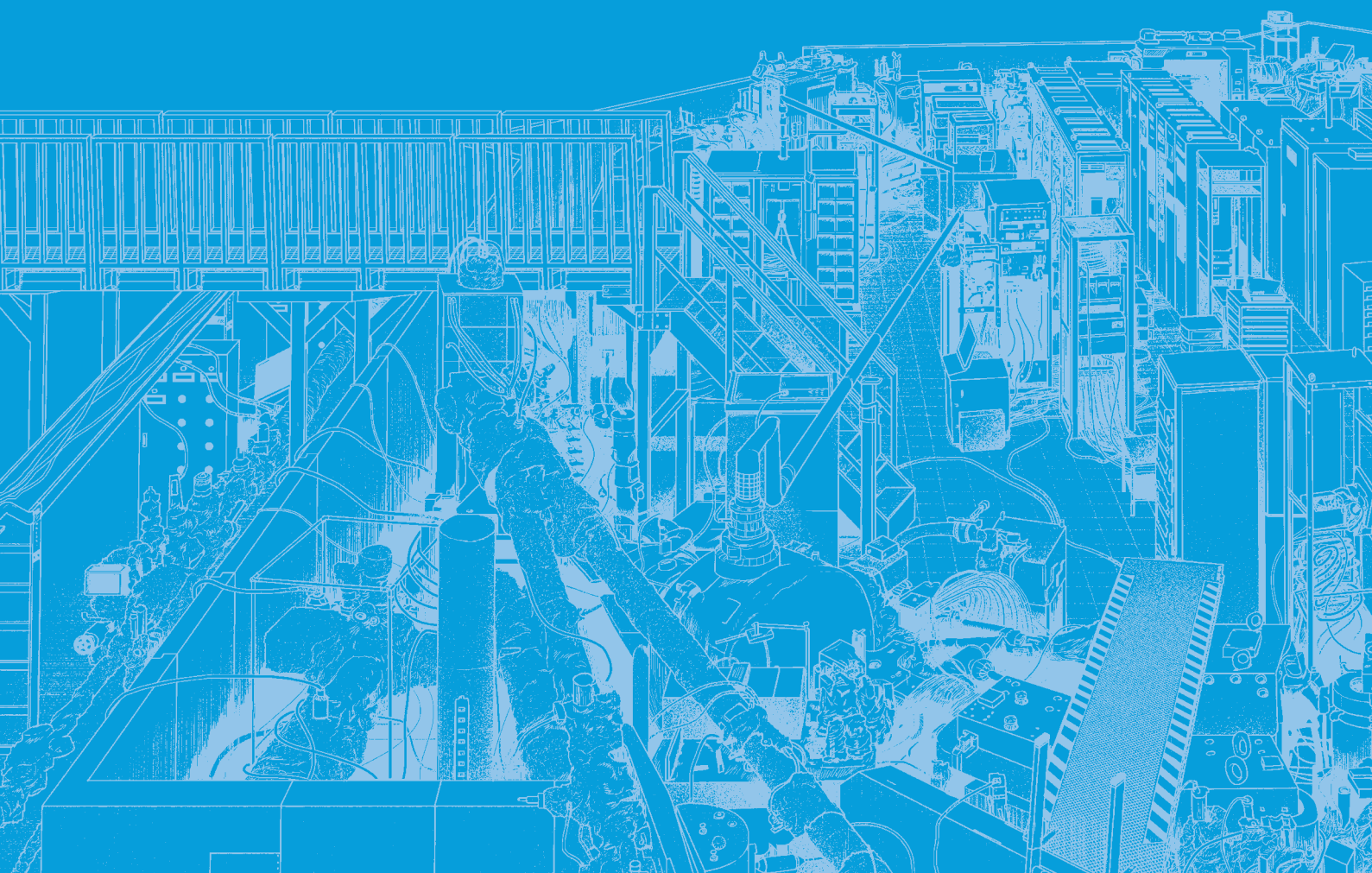

High light

BL4U

Observation of Charge Separation Reaction in a Ti-Mn Electrolyte for Redox Flow Batteries by STXM

E. Hosono[1,2,3], D. Asakura[1,2,3], A. Ohira[1,2], H. Yuzawa[4] and T. Ohigashi[4,5]

[1]*Global Zero Emission Research Center, National Institute of Advanced Industrial Science (AIST), Tsukuba, Ibaraki 305-8569, Japan*

[2]*Research Institute for Energy Conservation, AIST, Tsukuba, Ibaraki 305-8565, Japan*

[3]*AIST-UTokyo Advanced Operando Measurement Technology Open Innovation Laboratory (Operando-OIL), Kashiwa, Chiba 277-8565, Japan*

[4]*UVSOR Synchrotron Facility, Institute for Molecular Science, Okazaki 444-8585, Japan*

[5]*School of Physical Sciences, The Graduate University for Advanced Studies (SOKENDAI), Okazaki 444-8585, Japan*

Redox flow battery (RFB) is one of the candidates of large-scale energy storage device to utilize renewable energy. RFBs use the redox reaction of electrolytes [1], which is different from lithium-ion batteries using the redox reaction of the solid-state electrodes. To enhance the performances of RFBs such as cyclability, charge-discharge capacity, and cost, understanding the redox reaction is of particular importance. Electronic-structure analysis by synchrotron X-ray spectroscopy is essential to reveal the redox reaction.

In this study we focus on Ti-Mn RFB which involves sulfuric acid aqueous solution electrolyte with Ti and Mn ions [2]. The same Ti-Mn electrolyte is used for both positive and negative electrodes. The redox reaction has been thought to be

$$Mn^{2+} \Leftrightarrow Mn^{3+} + e^- \quad (1)$$

in the Ti-Mn electrolyte of the positive electrode and

$$(TiO)^{2+} + 2H^+ + e^- \Leftrightarrow Ti^{3+} + H_2O \quad (2)$$

in the Ti-Mn electrolyte of the negative electrode [2]. Besides, it has been reported that the Mn^{3+} ions in the charged electrolyte of the positive electrode (Eq. (1)) exhibits charge separation reaction as

$$2Mn^{3+} \rightarrow Mn^{2+} + Mn^{4+} \quad (3)$$

during the charge process [2]. Moreover, the Mn^{4+} ions are changed to MnO_2 which precipitates in the electrolyte of the positive electrode.

$$Mn^{4+} + 2H_2O \rightarrow MnO_2 + 4H^+ \quad (4)$$

This reaction is less reversible that is problematic for the cyclability. To further understand those reactions in Ti-Mn RFB, we demonstrate STXM measurements of the electrolytes [3]. The high spatial resolution of STXM is helpful to clarify the formation of precipitation.

To conduct soft X-ray spectroscopic measurements of liquid samples, we have developed a special cell as shown in Fig. 1 [3]. The Si_3N_4 thin-film window (100 nm) and UV curable resin bond separate liquid sample from the vacuum. A Ti-Mn electrolyte of the positive electrode was investigated by STXM at BL4U of UVSOR. The electrolyte had been charged up to 50 % of state of charge. The spatial resolution was around 100 nm.

Figure 2(a) shows the STXM image at the Mn L_3-edge. The bright area corresponds to a precipitate whose size is approximately 4 μm × 4 μm. The Mn L_3-edge absorption spectrum of the white area (I) shown in Fig. 2(b) is mostly attributed to Mn^{4+} state as compared with spectra of reference materials [4]. The surrounding area in Fig. 2(a) corresponds to the solution whose spectrum (area (II)) is attributed to Mn^{2+} state (Fig. 2(b)). Therefore, the charge separation reaction of Eq. (3) was successfully confirmed by STXM. Similar STXM experiments of different electrolytes will be performed to obtain strategies to suppress the formation of precipitations.

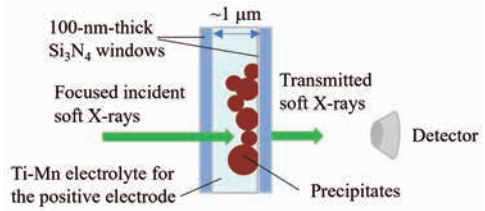

Fig. 1. A schematic image of the cell for the STXM measurements [3].

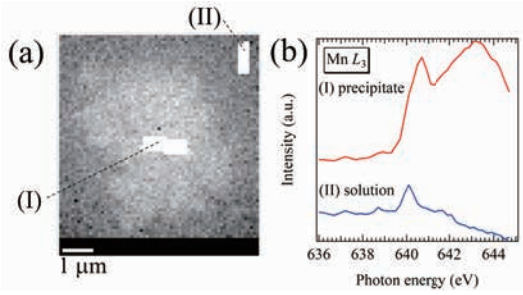

Fig. 2. (a) Mn L_3-edge STXM image and (b) spectra of selected area in the charged Ti-Mn electrolyte of the positive electrode [3].

[1] For example, T. Shigematsu, Curr. Opin. Electrochem. **18** (2019) 55.
[2] Y. R. Dong *et al*., ECS Trans. **69** (2015) 59.
[3] D. Asakura *et al*., Chem. Asian J. **18** (2023) e202201047.
[4] For example, R. Qiao *et al*., Nano Energy **16** (2015) 186.

BL7U

Temperature-dependent Electronic Band Structure of Organic Molecular Semiconductor

K. Fukutani [1, 2], F. Nishino[2], P. I. Jaseela[2], D. Okaue[3], K. Fukui[1,3], S. Makita[1], K. Tanaka[1,2] and S. Kera[1,2]

[1]*Institute for Molecular Science, Okazaki 444-8585, Japan*
[2]*The Graduate University for Advanced Studies (SOKENDAI), Okazaki 444-8585, Japan*
[3]*Graduate School of Engineering Science, Osaka University, Osaka 560-8531, Japan*

The organic molecular semiconductors are among the very promising materials in shaping the future of our electronic device applications in various aspects, including their physical flexibility, low cost of fabrication, high biodegradability in the environment, and the abundance of the constituent elements (mostly carbon and hydrogen) that are, in principle, inexhaustive. In fact, the organic molecular semiconductor crystals already play indispensable roles in our industry, and the continuing extensive researches have been ceaselessly improving their performances.

However, despite the success of organic molecular semiconductor devices, the knowledge of their electronic structure, one of the most fundamental building blocks for understanding and controlling their properties, is far from complete. Among such organic molecular semiconductors, single crystalline rubrene ($C_{42}H_{28}$) is known to exhibit exceptionally high carrier mobility (40 cm^2/Vs [1]) and is considered one of the most promising organic semiconductor materials for the next-generation electronics.

In this regard, we have been extensively investigating the electronic band structure of rubrene for the purposes of not only elucidating their band structures, but also for understanding the vibrational effects, arising from the intra-molecular and inter-molecular (phonon) degrees of freedom.

It is well known that many organic semiconductors exhibit a dual nature in their electronic transport properties, namely the (coherent) band transport and (polaronic) hopping transport, assisted by the electronic coupling to the aforementioned vibrations. Rubrene indeed falls into this category and its transport properties are believed to originate from the 'mixture' of both the band and the hopping transports. Since the respective contributions from each mechanism are believed to depend on temperature, it is clear that the direct experimental elucidations of the temperature-dependent band structure are essential for the full understanding of the origin of carrier transport in organic semiconductors.

However, there are very limited number of such direct measurements as with angle-resolved photoemission spectroscopy (ARPES) [2], most likely due to the numerous experimental difficulties, including the fabrication of large single crystals, removing of the sample charge-up effects and molecular damages caused by light irradiations.

In our experiments, we have successfully overcome these obstacles by utilizing BL7U at UVSOR and revealed the high-resolution temperature-dependent band structure of rubrene by ARPES. Figure 1 shows the band structure of rubrene observed at T = 300, 180, and 80 K along the π-stacking (Γ-Y) direction. Our data clearly shows the change in the band dispersion width as the temperature decreases. These data points towards the discernable change in the carrier effective masses, which play an important role in the determining the carrier mobilities. Furthermore, the band dispersion width appears to be 'locked' above T ~ 200 K, which is the temperature at which the structural anomaly [3] is observed. Our researches with these experimental results are expected to provide a key insight into the transport mechanisms of organic semiconductors.

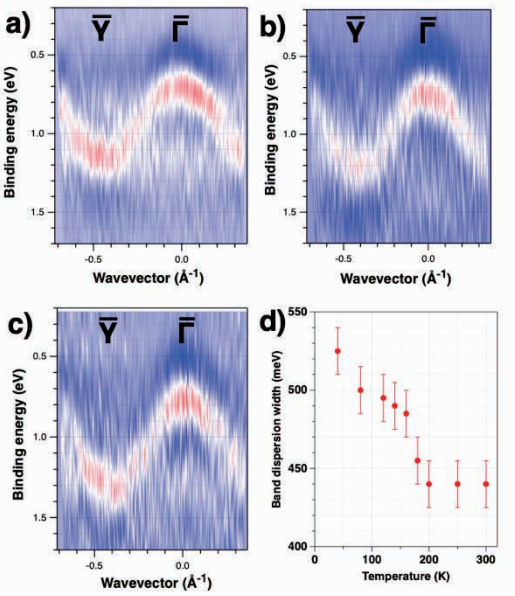

Fig. 1. Temperature-dependent ARPES data (second derivative plots) obtained along the Γ-Y direction at (a) T = 300 K, (b) 180 K and (c) 80 K. (d) shows the band dispersion widths as a function of temperature extracted from our measurements.

[1] J. Takeya *et al.*, Appl. Phys. Lett. **90** (2007) 102120.
[2] F. Bussolotti *et al.*, Nat. Commun. **8** (2017) 173.
[3] A. van der Lee *et al.*, J. Phys. Chem. Lett. **13** (2022) 406 .

BL1U

Gamma-induced Positron Annihilation Lifetime Spectroscopy of β-SiAlON:Eu Phosphor

M. Kitaura[1], S. Watanabe[2], H. Masai[3], Y. Taira[4,5], K. Takahashi[6], T. Takeda[6], N. Hirosaki[6], M. Tansho[7], K. Deguchi[7], S. Ohki[7] and A. Ohnishi[1]

[1]*Faculty of Science, Yamagata University, Yamagata 990-8560, Japan*
[2]*Institute of Innovative Research, Tokyo Institute of Technology, Tokyo 152-8550, Japan*
[3]*Department of Materials and Chemistry, National Institute of Advanced Industrial Science and Technology, Ikeda 563-8577, Japan*
[4]*UVSOR Synchrotron Facility, Institute for Molecular Science, Okazaki 444-8585, Japan*
[5]*School of Physical Sciences, The Graduate University for Advanced Studies, Okazaki 444-8585, Japan*
[6]*Research Center for Functional Materials, National Institute for Materials Science, Tsukuba, Ibaraki 305-0044, Japan*
[7]*High field NMR group, National Institute for Materials Science, Tsukuba, Ibaraki 305-0003, Japan*

Eu-doped β-SiAlON ($Si_{6-z}Al_zO_zN_{8-z}$; $0 \leq z \leq 4.2$) is well-known to be a green-emitting phosphor with high brightness, narrow line width, and excellent resistance to thermal quenching [1]. These features are indispensable for the development of next-generation phosphors to fabricate advanced wide gamut backlighting device. For this purpose, it is important to investigate the nature of lattice imperfections such as vacancies, interstitials, and unexpected impurities, because they affect adversely as so-called “killer” or “trap” responsible for luminescence quenching and afterglow.

Positron annihilation lifetime spectroscopy (PALS) is a unique experimental method that can probe vacancy-type defects with negative charge. In the present study, we investigated such vacancy-type defects in β-SiAlON:Eu phosphors by gamma-ray induced PALS (GiPALS) experiment [2]. GiPALS experiment was performed at the BL1U of UVSOR synchrotron facility. Positron annihilation lifetimes and relative intensities were analyzed using the software LT10 [3]. Positron annihilation lifetimes at the bulk and defect states were calculated by two-component density-functional-theory (TCDFT) calculations [4,5].

Figure 1 shows the GiPALS spectrum of a β-SiAlON:Eu phosphor. The composition was $Si_{5.97}Al_{0.03}O_{0.03}N_{7.97}Eu_{0.01}$. The data were obtained at room temperature. The GiPALS spectrum reproduced three exponential decay components indicated by broken lines. The first and second component with short and middle lifetime are attributed to the positron annihilation at the bulk and defect states in β-SiAlON, respectively. The third component with long lifetime originates in the formation of positroniums, which may arise from amorphous layer covering phosphor particles [6]. The relative intensity of the third component was negligibly small compared to other two. To estimate bulk lifetimes using experimental lifetimes and relative intensities, we adopted two-state trapping model, where the long lifetime component was not considered. The experimental bulk lifetime was estimated to be 265±18 ps. This value agreed with the bulk lifetime (= 271 ps) calculated for the relaxed lattice of a β-SiAlON ($Si_{95}Al_1O_1N_{127}$). This fact indicates the validation of our experiment and calculation. On the other hand, the lifetime of the middle lifetime component was not reproduced by DFT calculations for monovacancies at silicon and nitrogen sites. We suppose that the second component originates in defect complexes of multiple vacancies. The origin of the second component is now in investigation.

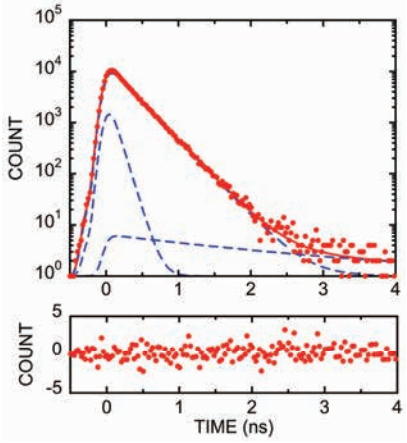

Fig. 1. (Upper) GiPALS spectrum of a β-SiALON:Eu phosphor. (Lower) Residual between the results of experiment and curve fit analysis.

[1] X. Zhang *et al*. Chem. Mater. **29** (2017) 6781.
[2] Y. Taira *et al*., Rev. Sci. Instrum. **84** (2013) 053305.
[3] D. Giebal and J. Kansy, Phys. Procedia **35** (2012) 122.
[4] P. Giannozzi *et al*. J. Phys.: Condens. Matter **21** (2009) 395502.
[5] X. Gonze *et al*., Comput. Phys. Commum. **248** (2020) 107042.
[6] N. Hirosaki *et al*., Appl. Phys. Lett. **86** (2005) 211905.

BL1U

In-situ Measurement of Defects Dynamics in Stress Applied Bulk Iron by Means of Gamma Ray Induced Positron Annihilation Spectroscopy

F. Hori [1], S. Araki[1], S. Hirayama[1] and Y. Taira[2]

[1]*Dept. of Quantum and Radiation Eng., Osaka Metropolitan University, Sakai, Osaka 599-8570, Japan*

[2]*UVSOR Synchrotron Facility, Institute for Molecular Science, Okazaki 444-8585, Japan*

The behavior of hydrogen atoms is attracting attention in a wide range of research fields such as high-strength structural materials and hydrogen storage materials. In such materials, hydrogen atom diffuses and has various interaction with defects, consequently it makes serious characteristic change. In particular, in the corrosion of metallic materials, it is known that the presence or absence of lattice defects in the material affects mechanical and physical properties of materials. On the point of view, positron annihilation techniques are useful to detect and estimate the behavior of vacancy type micro defects in materials. However, in order to investigate the dynamics of the internal defect behavior without destructing materials, more than mega electron volts positron is needed. Recently, the development of high-energy Gamma-ray induced positron spectroscopy (GiPS) has developed at some photon factories. Especially, direct incidence of high-energy gamma rays with the energy more than 1.022 MeV into the target material produces positrons in it and annihilated there. High-energy gamma rays from laser Compton scattering at synchrotron radiation facilities enables positron experiments to detect defects in bulk materials without sample destruction. In this study, in-situ positron annihilation lifetime measurement while applying stress to a bulk specimen have performed on the beam line BL1U at UVSOR.

Positron lifetime measurement has performed on pure iron bulk specimens processed into JIS standard tensile specimens, irradiated with 8 MeV electron, and irradiated with electron and then hydrogen introduced. Electron irradiation have done by linear accelerator at Kyoto University Reactor Research. Hydrogen was introduced into the sample by immersion in a 20% ammonium thiocyanate solution at 318 K for 14 days.

Figure 1 shows the results of the stress change after applying a stress of 88 MPa, corresponding to 90% of the yield stress, for all samples. It is clear that stress relaxation is suppressed by the presence of hydrogen and vacancies. In addition, the sample without defects relaxes greatly in a short period of time and almost no change can be confirmed after that, but the sample with vacancy and hydrogen shows a small amount of relaxation, but it relaxes slowly over a long period of time. Figure 2 shows the change of positron lifetimes and their relative intensities during relaxation after initial stress applied. The long lifetime of positron τ_2 increase to more than 170 ps after stress application in all samples, indicating that vacancies were formed even at stresses below the yield point. Also, τ_2 for hydrogen introduced sample slightly higher than that of pure Fe. This indicates the formation of vacancy clusters, such as di-vacancy, and the presence of hydrogen may facilitate the aggregation of vacancies. However, this is considered that the τ_2 slightly decreases taking long time afterwards indicates that these initially formed di-vacancies dissociate. Also, it found that the relative intensity I_2 corresponds to the defect concentration of τ_2 component, and the concentration change after stress addition also shows a slight decrease with relaxation time.

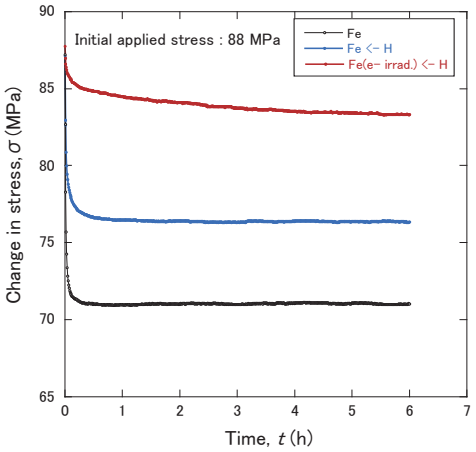

Fig. 1. Stress change after initial stress applied.

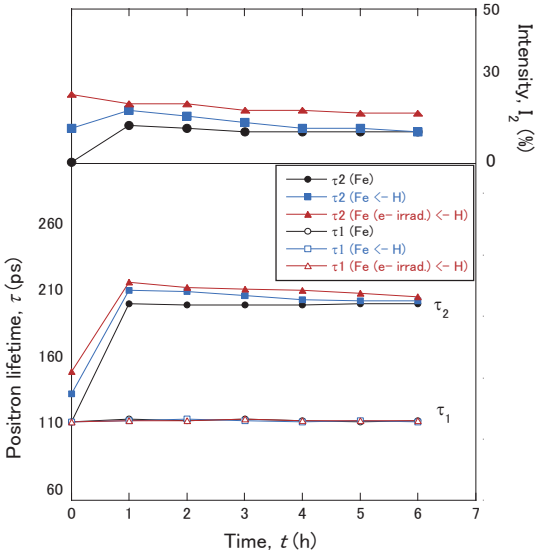

Fig. 2. Positron lifetimes and relative intensity I_2 change after initial stress applied.

BL1U

Gamma-ray Induced Positron Annihilation Lifetime Measurement of CeO_2 Catalyst Placed in a Quartz Tube

S. Dohshi[1], K. Maeda[1], Y. Taira[2] and T. Hirade[3]
[1]*Osaka Research Institute of Industrial Science and Technology*
2-7-1, Ayumino, Izumi, Osaka 594-1157, Japan
[2]*UVSOR Synchrotron Facility, Institute for Molecular Science, Okazaki 444-8585, Japan*
[3]*Japan Atomic Energy Agency, Ibaraki 319-1195, Japan*

In situ observation of the catalyst during catalytic reactions is very important for elucidating the reaction mechanism and preparing the highly active catalyst. Recently, it has been reported that the presence of oxygen vacancies in CeO_2 catalysts affect their catalytic activity [1]. Therefore, it becomes more and more important to analyze the behavior of oxygen vacancies of CeO_2 with high sensitivity during catalytic reactions.

Positron annihilation lifetime measurement is a powerful tool for the detection of lattice defects such as oxygen vacancies with high sensitivity. However, there have been no examples of positron annihilation lifetime measurements with controlling gas atmosphere and temperature. Typically, the catalytic reaction is performed in a quartz or alumina tube with controlling gas atmosphere and temperature. When gamma-ray induced positron annihilation lifetime measurement is performed under the same conditions as the catalytic reaction, positrons generated in the sample can be annihilated not only in the sample but also in the quartz tube, because of the presence of the quartz tube between the sample and the detector.

In this study, the effect of quartz tube on the positron annihilation lifetime of CeO_2 was investigated.

The pellet sample with 20 mm in diameter and 10 mm in thickness were prepared using CeO_2 nanoparticles with a primary particle size of ca. 2 nm.

We have set up a gamma-ray spectroscopy system at the laser-Compton scattering (LCS) beamline of BL1U at UVSOR-III [2], and measured the lifetime of the annihilation gamma-rays at room temperature using BaF_2 scintillation detector. We used the software Lifetime9 (LT9) to analyze the spectra.

Table 1 shows the positron annihilation lifetimes and relative intensities of CeO_2 catalyst with various measurement conditions. In case of the measurement without quartz tube, the positron annihilation lifetime was composed of two components (τ_1 and τ_2). These lifetimes were attributed to the positron annihilation in CeO_2 bulk and surface. On the other hand, in case of the measurement with quartz tube, the positron annihilation lifetime was composed of three components (τ_1, τ_2 and τ_3). The longest lifetime component (τ_3) can be attributed to the annihilation in the quartz tube, with a relative intensity (I_3) of about 1%, regardless of the gamma-ray beam diameter. Furthermore, the lifetimes and relative intensities of the other two components derived from CeO_2 (τ_1 and τ_2) did not change significantly when measured using quartz tubes. These results suggest that positron annihilation lifetime measurements can be performed in a quartz tube while controlling the gas atmosphere and temperature.

Next fiscal year, gamma-ray induced positron annihilation lifetime measurement will be performed with controlling the gas atmosphere and temperature to clarify the behavior of oxygen vacancies in CeO_2.

[1] X. Liu *et al*., J. Am. Chem. Soc. **131** (2009) 3140.
[2] Y. Taira *et al*., Rev. Sci. Instr. **84** (2013) 053305.

Table 1 Positron annihilation lifetimes and relative intensities of CeO_2 catalyst with various measurement conditions.

measurement conditions	τ_1 (ps)	I_1 (%)	τ_2 (ps)	I_2 (%)	τ_3 (ps)	I_3 (%)
without quartz tube	155±17	6.5±1.0	388.2±1.5	93.5±1.0	-	-
with quartz tube (γ-ray beam: 2 mm)	159±42	3.8±1.1	367.8±1.9	95.0±1.1	1386±46	1.2±0.1
with quartz tube (γ-ray beam: 3 mm)	142±44	4.2±1.7	362.5±4.0	94.4±1.7	1290±120	1.4±0.3

Formation of the stress-induced Vacancies in Iron by *in situ* Positron Annihilation Lifetime Spectroscopy

M. Fujinami[1], R. Awaji[1], A. Yabuuchi[2], T. Hirade[3], N. Oshima[4] and Y. Taira[5]
[1]*Department of Applied Chemistry and Biotechnology, Chiba University, Chiba 263-8522, Japan*
[2]*Institute for Integrated Radiation and Nuclear Science, Kyoto University, Kumatori 590-0494, Japan*
[3]*Nuclear Science and Engineering Center, Japan Atomic Energy Agency, Tokai 319-1195, Japan*
[4]*National Institute of Advanced Industrial Science and Technology, Tsukuba 305-8568, Japan*
[5]*UVSOR Synchrotron Facility, Institute for Molecular Science, Okazaki 444-8585, Japan*

Investigating the formation process of atomic vacancies by mutual cutting of dislocations is essential to understand the role of vacancies in the mechanical properties of metals. However, such vacancies have yet to be directly observed. The reason is that vacancies have a significant diffusion coefficient and are unstable.

Positron annihilation lifetime spectroscopy is the only method that allows direct observation of atomic vacancies. However, the conventional method using a radioactive isotope such as ^{22}Na as a positron source is difficult to measure *in situ* under various conditions due to the risk of radioactive contamination. If it becomes possible to measure the vacancies while applying stress, it will be possible to detect transient vacancies, which leads to the first detection of transient vacancy formation. It also provides essential fundamental knowledge for discussing the behavior of vacancy stabilization by impurities, including hydrogen. In this study, we attempted to directly detect vacancies formed in pure iron during tensile deformation *in situ* using the BL1U beamline, where positrons are created in the sample directly.

A 3-mm-thick tensile sample was mounted on a small tensile tester. The sample was subjected to tensile deformation up to a nominal strain of over 7% with a strain rate of 2.2×10^{-5} s^{-1}. Ten samples were measured under the same tensile deformation conditions to obtain enough counts of positron lifetime spectra.

Figure 1 shows the positron lifetime spectra of pure iron before and after tensile deformation. A longer lifetime component is observed in the positron lifetime spectrum when the sample is elongated to a nominal strain of ~7.3%. Figure 2 shows the change in mean positron lifetime during tensile deformation. The mean positron lifetime increases with increasing nominal strain. However, the change in mean positron lifetime obtained in this study differs significantly from the trend reported in an earlier study using the conventional method [1]. One possible reason for this difference is the difference between the conventional method, which observes a depth of about 0.1 mm from the sample surface, and this method, which observes the entire sample, including the deeper region. Further detailed analysis is currently underway.

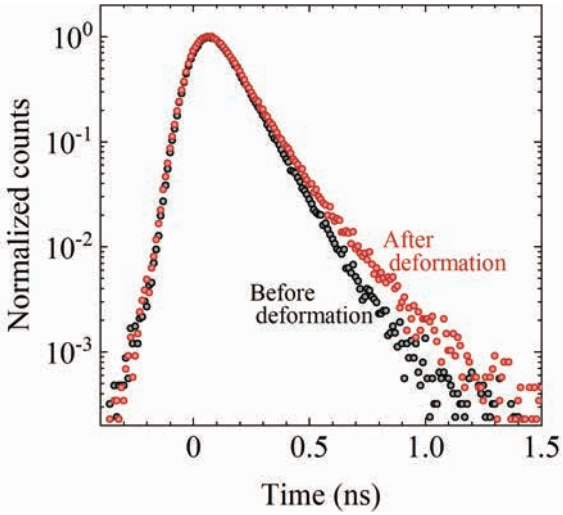

Fig. 1. Positron lifetime spectra of pure iron before and after tensile deformation with a nominal strain of ~7.3%.

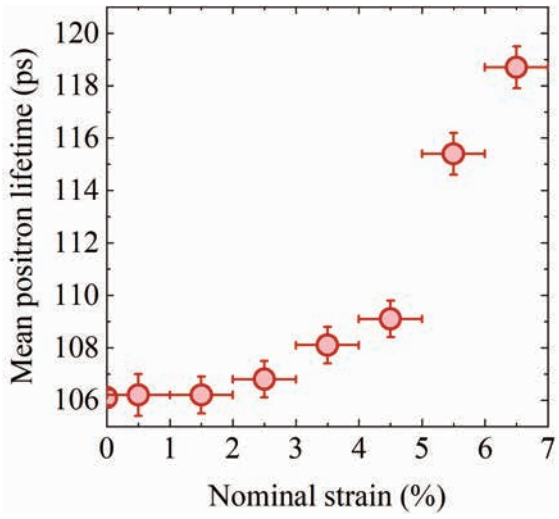

Fig. 2. Change in mean positron lifetime during tensile deformation.

[1] B. Somieski *et al.*, NDT & E Int. **27** (1994) 235.

BL1U

In-situ Measurements of Vacancies Formed in Pure Iron by Electrolytic Hydrogen Charging using gamma-ray-induced Positron Annihilation Lifetime Spectroscopy

A. Yabuuchi[1], T. Hirade[2], M. Fujinami[3], R. Awaji[3], N. Oshima[4], K. Takai[5] and Y. Taira[6]

[1]*Institute for Integrated Radiation and Nuclear Science, Kyoto University, Kumatori 590-0494, Japan*
[2]*Nuclear Science and Engineering Center, Japan Atomic Energy Agency, Tokai 319-1195, Japan*
[3]*Department of Applied Chemistry and Biotechnology, Chiba University, Chiba 263-8522, Japan*
[4]*National Institute of Advanced Industrial Science and Technology, Tsukuba 305-8568, Japan*
[5]*Department of Engineering and Applied Sciences, Sophia University, Tokyo 102-8554, Japan*
[6]*UVSOR Synchrotron Facility, Institute for Molecular Science, Okazaki 444-8585, Japan*

Recently, a fracture mechanism involving vacancies has been proposed as a new model to explain the hydrogen embrittlement of steels [1]. Therefore, many studies on hydrogen embrittlement have been performed using positron annihilation spectroscopy, a vacancy detection technique. However, the conventional positron annihilation technique is challenging to measure during hydrogen dosing in a liquid. The high-energy pulsed gamma-rays obtained at UVSOR make it possible to produce positrons directly inside a sample placed in a fluid and perform positron annihilation measurements. In this study, we attempted in-situ positron annihilation lifetime measurements during hydrogen charging in liquid to investigate hydrogen-induced vacancies in pure iron.

Six well-annealed pure iron plates with a purity of 99.99% and a thickness of 2 mm were arranged in the beam axis direction with a gap of 2 mm between them. This measurement geometry was chosen to achieve sufficient hydrogen introduction throughout the sample and still obtain a sufficient count rate of annihilation gamma-rays. For electrolytic hydrogen charging, the sample was immersed in 0.1 N NaOH solution containing 5 g/L NH_4SCN. A pulsed gamma-ray beam with a maximum energy of 6.6 MeV was injected to measure the positron lifetime.

Figure 1 shows the positron lifetime spectra of pure iron plate samples placed in air and the electrolyte solution. The spectrum obtained from the in-air measurement shows almost no lifetime component of positrons annihilated outside the sample. In contrast, a longer lifetime component originating from positron annihilation in the electrolyte solution appears in the spectrum obtained from the sample placed in the electrolyte solution. The change in positron lifetime in iron during hydrogen charging was investigated by analyzing such spectra. However, it was concluded that eliminating the electrolyte solution component from the spectra is essential for a detailed analysis of the iron sample components.

Figure 2 shows the calculated positron flux distribution when a gamma-ray beam is injected into an iron plate in water. Positrons are mainly produced in iron, which has a high specific gravity, but they are also produced to some extent in water. In addition, some of the positrons produced in iron are emitted out of iron and annihilated in water. Therefore, we consider improving the measurement geometry for the next beamtime.

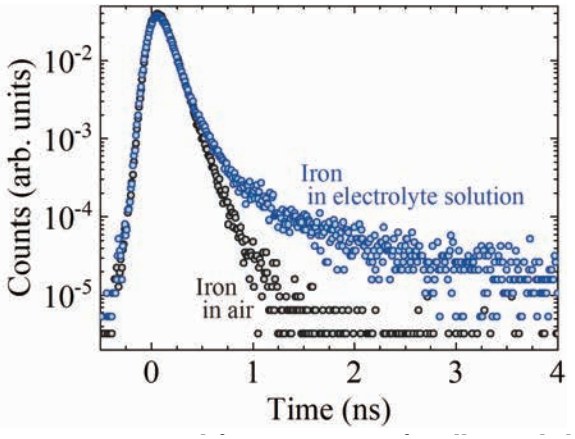

Fig. 1. Positron lifetime spectra of well-annealed pure iron measured in air or an electrolyte solution.

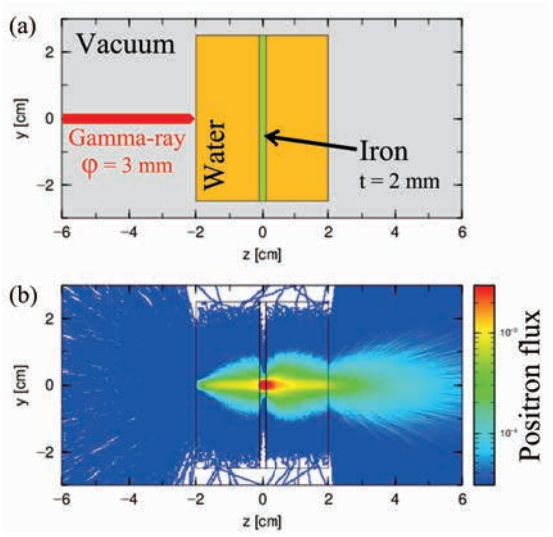

Fig. 2. (a) Geometry of the simulation model. (b) Calculated positron flux distribution.

[1] M. Nagumo, Mater. Sci. Technol. **20** (2004) 940.

Formation of Catalytically Active Mo_2C Species on H-MFI for Methane Aromatization Studied by Mo L-edge XANES

K. Kuramochi[1], Y. Sonobe[2], H. Shimura[2], Y. Kinoshiro[2], R. Yamazaki[1], Y. Uchimura[2] and H. Aritani[2]

[1]*Advanced Science Research Laboratory, Saitama Institute of Technology, Fukaya 369-0293 Japan*
[2]*Graduate School of Engineering, Saitama Institute of Technology, Fukaya 369-0293 Japan*

As a typical GTL (Gas-To-Liquid) catalyst, supported molybdenum on H-MFI zeolites show catalytically high and selective activity to convert methane to benzene directly. Although the GTL process is extremely innovative, it is an important subject to suppress deactivation as well as increase the yield of aromatics. For the Mo/H-MFI catalysts, definite deactivation due to coke deposition has been a major problem for enhancement of MTB reactivity. A cause of the deactivation strongly depends on both coke deposition onto strong acid sites over H-MFI and structural deactivation of carbonized Mo species. One of the most important subjects for catalytically high and durable activity is the elucidation of active Mo carbide (MoC_x) species and their structural stability. In this study, Mo L_{III}-edge XANES is applied to characterize the active MoC_x species on Mo/H-MFI during the methane aromatization.[1] The change of active Mo species during the reaction was investigated as a time course of XANES spectra.

Mo/H-MFI (Si/Al_2=23-30 in H-MFI, 5.0 wt% as MoO_3-loading) catalysts were prepared as described in the previous paper.[2] The methane dehydro-aromatization reactivity was evaluated at 1023 K. Mo L_{III}-edge XANES spectra were obtained in BL2A of UVSOR-IMS in a total-electron yield mode using the InSb double-crystal monochromator. A REX-2000 (Rigaku) software was used for normalization of each XANES spectra. The edge energy was obtained from the maximum of the first derivative of XANES.

Figure 1 shows the L_{III}-edge XANES of reference Mo compounds. The energy of the absorption edge becomes higher according to the higher oxidation state of molybdenum. For Mo-carbides, the edge energy in α-Mo_2C (fcc: 2526.55 eV) is significantly larger than that in β-Mo_2C (orthorhombic: 2524.45 eV). Since the difference of energy value should be due to the coordination number in Mo-C shells, the edge energy of XANES can be applied to characterize the local structure of Mo_2C species.

For evaluation of catalytic activity for methane aromatization at 973 K, it is concluded that Mo/H-MFI(Si/Al_2=30) shows the maximum benzene yield in 30 minutes as an initial streaming range. On the Mo/H-MFI catalysts, time course of L-edge XANES spectra are shown in Figure 2. Before the reaction (at 0 min.), the Mo/H-MFI catalyst has been pre-reduced with CO(2%)-He at 1023 K. At this time, Mo species have already reduced to form Mo^{4+} (due to MoO_2) and/or Mo^{2+} (α-Mo_2C). The edge of XANES shifts to the low energy side after the reaction for 10 minutes, indicating that further reduction of Mo proceeds to form β-Mo_2C like species with low crystallinity. Since the edge energy is kept on after 90 minutes (in the maximum activity) is exhibited, β-Mo_2C like species are possibly act as a highly active one for methane dehydrogenation. As the reaction time progresses, only a slight shift of the edge to the lower energy side can be seen. Therefore, it is presumed that the deactivation of reactivity after 30 minutes is caused mainly by carbon deposition on H-MFI support rather than excess reduction of Mo species.

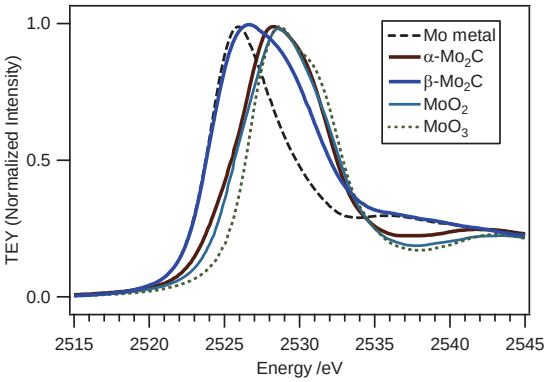

Fig. 1. Mo L_{III}-edge XANES spectra of reference Mo compounds.

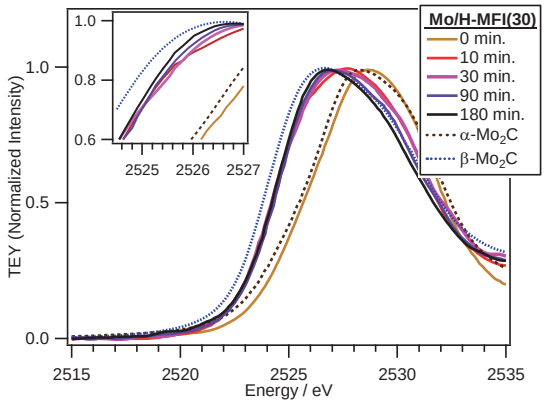

Fig. 2. Mo L_{III}-edge XANES spectra of Mo/H-MFI (Si/Al_2=30) catalyst after the reaction for each time (0 – 180 minutes).

[1] H. Aritani *et al.*, *UVSOR Activity Report 2021* **49** (2022) 58.
[2] H. Aritani *et al.*, J. Environm. Sci., **21** (2009) 736.

BL2A

Local Environment of Dopants in (*M*, Nb) co-doped TiO_2 (*M*=Fe, Ni)

H. Murata [1, 2], T. Nishio[2], Y. Nagatomo[2] and A. Nakahira[1, 2]
[1]*Department of Materials Science, Osaka Metropolitan University, Sakai 599-8531, Japan*
[2]*Department of Materials Science, Osaka Prefecture University, Sakai 599-8531, Japan*

Titanium dioxide (TiO_2) is a typical fine ceramic material used in a wide range of applications, such as photocatalysts, pigments and transparent conductors. TiO_2 has a several polymorphs with wide band gaps and absorb only UV light. Numerous studies have been carried out on cation and anion doping into TiO_2 to utilize visible light. However, most of them induce weak visible light absorption due to their small solid solubility limits. Co-doping into TiO_2 has been investigated [1] and combinations of dopants such as (Fe, Nb) and (Ni, Nb) significantly increase solid solubility limits [2-4]. However, local environments of the co-doped dopants int TiO_2 and their light absorption mechanism have not been clarified. In this study, local environments and electronic structures of (Fe, Nb) and (Ni, Nb) co-doped TiO_2 were investigated.

(Fe, Nb) and (Ni, Nb) co-doped TiO_2 samples were prepared by a conventional solid-state reaction method using TiO_2, Fe_2O_3, NiO and Nb_2O_5 as starting materials. The stating materials were ground and mixed by an alumina mortar and pestle. They were calcined in an alumina crucible at 1200 °C for 6 h. The samples were ground and mixed by the mortar and pestle again. Then, they were calcined in an alumina crucible at 1200 °C for 6 h.

Samples were characterized using X-ray diffraction (XRD), UV-Vis, ^{57}Fe Mössbauer spectroscopy, and X-ray absorption near edge structure (XANES). Ni-L_3 and Nb-L_3 XANES spectra were collected using the total electron yield method with a sample current at BL2A in UVSOR (Okazaki, Japan). The X-ray beam was monochromated using beryl and InSb double crystals for Ni-L_3 and Nb-L_3, respectively. NiO and Nb_2O_5 was used as reference materials.

XRD patterns of the samples can be assigned to rutile-type TiO_2 with peak shifts. They confirmed that (Fe, Nb) and (Ni, Nb) co-doped TiO_2 has large solubility limit over 50 cation%, where the dopants ratios are 1:1 and 1:2 for (Fe, Nb) and (Ni, Nb), respectively. Note that their lattice parameters increased linearly with the concentration of dopants.

^{57}Fe Mössbauer spectroscopy and Ni-L_3 XANES show that Fe and Ni in the samples are high-spin Fe^{3+} and Ni^{2+} in octahedral coordination, respectively. Nb-L_3 XANES of the samples have typical features of Nb^{5+} in octahedral coordination [5], as shown in fig. 1. These results indicate that large solid solubility limit of the co-doped TiO_2 is due to charge compensation between dopants.

Both of the co-doped TiO_2 samples exhibited visible light absorption. Based on the spin and valence states of dopants, the visible light absorptions are induced at different origins. The (Fe, Nb) co-doped TiO_2 has a narrowed band gap and weak spin forbidden d-d transitions. On the other hand, the (Ni, Nb) co-doped TiO_2 has a strong spin-allowed d-d transition. These different origins of visible light absorption fundamentally influence behaviors of excited careers and chromaticity. These results lead to a comprehensive understanding of the visible light applications such as photocatalyst and pigments.

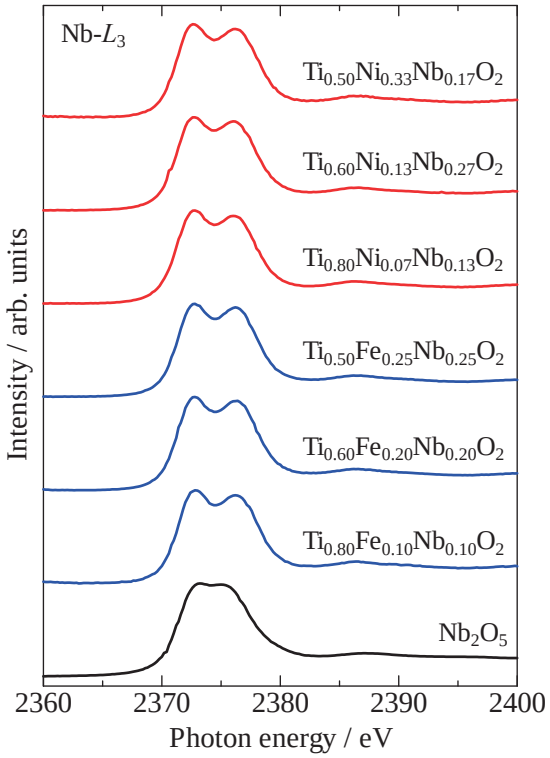

Fig. 1. Nb-L_3 XANES spectra of (Fe, Nb) and (Ni, Nb) co-doped TiO_2.

[1] A. S. M. Nur *et al.*, J. Water Process. Eng. **47** (2022) 102728.
[2] M. A. Tena *et al.*, Mater. Res. Bull. **27** (1992) 1301.
[3] B. Balzer and H. Langbein, Cryst. Res. Technol. **31** (1996) 93.
[4] M. Wenger and T. Armbruster, Neues Jahrb. Mineral. Monatsh. **5** (1993) 225.
[5] Y. Kubouchi *et al.*, X-ray Spectrom. **41** (2012) 259.

BL2A

XAFS Study of $MgAl_2O_4$ - $MgGa_2O_4$ Solid Solutions

S. Yoshioka [1], K. Yasuda[1], E. Kobayashi[2] and K. Okudaira[3]
[1]*Department of Applied Quantum Physics and Nuclear Engineering, Kyushu University, Fukuoka, 819-0395, Japan*
[2]*Kyushu Synchrotron Light Research Center, Saga 841-0005, Japan*
[3]*Graduate school of Advanced Integration Science, Chiba University, Chiba, 263-8522, Japan*

Spinel oxides with the general formula AB_2O_4 can be formed with various kinds of divalent A and trivalent B cations. Owing to their unique mechanical, electronic, and magnetic properties, the spinel oxides have gained considerable attention not only from the fundamental research fields but also from the industrial application point of view. Some spinel compounds accommodate a large degree of cationic disorder. The cationic disordering naturally affects the structural properties of the spinels. For example, magnesium aluminate ($MgAl_2O_4$) and magnesium gallate ($MgGa_2O_4$) are generally known as normal and inverse spinel structures, respectively. However, their inversion degrees for synthetic specimens were also reported to be fluctuating between 0 and 1, respectively, due to the cationic disordering. Recently, the structure of $MgAl_{2-x}Ga_xO_4$ was reported using first principles calculations and X-ray diffraction [1]. X-ray absorption spectroscopy (XAS) is a powerful structure characterization method that uses an X-ray probe to reveal local atomic coordination and electronic structures. In this study, we focus on the local structures in $MgAl_2O_4$ – $MgGa_2O_4$ solid solutions, particularly cationic-disordered structures.

The polycrystalline samples of $MgAl_{2-x}Ga_xO_4$ (x = 0, 0.5, 1.0, 1.5, and 2.0) were synthesized by a solid-state reaction. They were sintered in air at 1500 ºC for 10 h followed by furnace. Mg and Al *K*-edge XANES measurements were performed on BL2A beamline at UVSOR Synchrotron Facility, Okazaki, Japan, using the partial fluorescence yield method. A $KTiOPO_4$ double-crystal monochromator gives Mg and Al *K*-absorption edges in the energy regions 1290–1340 eV and 1540–1610 eV, respectively. The measurements of Mg and Al *K*-edge XANES spectra were carried out in vacuum at a pressure and temperature of 1×10^{-4} Pa and 20 ºC, respectively. Fluorescence X-rays of Mg K_α and Al K_α were collected utilizing an energy-dispersible silicon drift detector.

The Mg *K*-edge XANES spectra for $MgAl_2O_4$ and $MgGa_2O_4$ are shown in Fig. 1. The intensity of each spectrum was normalized to a value of 1 at the photon energy of 1330 eV after the removal of the background intensity. The Mg *K*-edge XANES of $MgGa_2O_4$ were clearly different from that of $MgAl_2O_4$. The spectrum difference between $MgAl_2O_4$ and $MgGa_2O_4$ suggests local structure difference between two specimens. Previous study using diffraction technique reported octahedral location of Mg in $MgGa_2O_4$ as an inverse spinel, whereas tetrahedral location of Mg in normal spinel of $MgAl_2O_4$. Detailed analyses on the local environment of Mg and Al in the $MgAl_{2-x}Ga_xO_4$ are in progress by combined use of the XANES and the first principles band structure calculations.

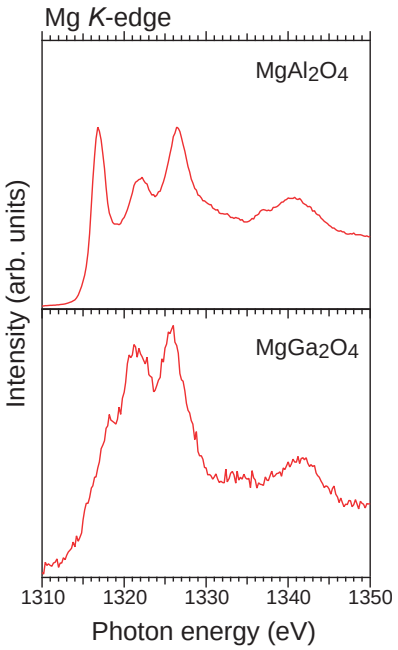

Fig. 1. Mg *K*-edge XANES spectra of $MgAl_2O_4$ and $MgGa_2O_4$

[1] G. Pilania, V. Kocekski, J. A. Valdez, C. R. Keller and B. P. Uberuaga, Commun. Mater. **1**, Article number: 84 (2020).

BL2A

NEXAFS Spectroscopy of Battery Materials Using a Transfer Vessel

A, Inoishi[1] and E. Kobayashi[2]
[1]*Institute for Materials Chemistry and Engineering, Kyushu University*
6-1 Kasuga-koen, Kasuga-Shi 816-8580, Japan
[2]*Kyushu Synchrotron Light Research Center, 8-7 Yayoigaoka, Tosu, Saga 841-0005, Japan*

To increase capacity in all solid-state lithium-ion batteries, it is better to remove as much of the solid electrolyte and conductive carbon contained in the electrode as possible. Recently, we reported the all-solid-state lithium batteries using electrochemical lithium insertion in some anode materials. We reported $Mg(BH_4)_2$, and MgH_2 anode materials.[1,2] In these conversion-type electrodes, $LiBH_4$ and LiH are generated as lithium salt during lithiation and ionic conduction paths are formed during the electrochemical reaction. Solid electrolyte is not required in these electrode mixture and reasonable battery performances were observed with the electrode composed of active material ($Mg(BH_4)_2$ or MgH_2) and acetylene black, without electrolyte powder. We call this new concept as "*in-situ* forming of solid electrolyte". Recently, we newly focused on $MgCl_2$ as a new anode active material. For the case of $MgCl_2$, it is assumed that LiCl is formed after lithiation as "*in-situ* formed electrolyte". In this study, we evaluated the mechanism of electrochemical reaction of $MgCl_2$ anode by X-ray adsorption spectroscopy.

Composite powder containing $MgCl_2$ was prepared by mechanical milling of $MgCl_2$ with acetylene black (AB) in a 70:30 mass ratio at 400 rpm for 30 min. Each all-solid-state cell ($Li/LiBH_4/MgCl_2$, AB) was assembled using an insulating cell die (Poly Ether Ether Ketone) sandwiched between two stainless steel rods under Ar. Discharge/charge measurements were conducted in a vacuum at a current density of 0.05 $mAcm^{-2}$ and at 120 °C. *Ex-situ* X-ray absorption spectroscopy (XAS) data for Mg K-edge and Cl K-edge were acquired at the BL2A of UVSOR Synchrotron Facility, Institute for Molecular Science. For the transportation to XAS, a sample transfer vessel was used.[3,4]

Initial lithiation capacity and delithiation capacity of the $Li/LiBH_4/MgCl_2$ cell were 465 $mAhg^{-1}$ and 321 $mAhg^{-1}$, respectively. The initial lithiation capacity was 82 % of the theoretical capacity of $MgCl_2$. In this electrode, solid electrolyte is not required in the electrode mixture. This indicates that lithium conduction path is formed from $MgCl_2$ by the electrochemical reaction. Mg K-edge X-ray adsorption spectroscopy for the $MgCl_2$ electrode before and after the discharge-charge were measured. $MgCl_2$ showed sharp peaks at 1310 eV. "Initial state" just after cell fabrication was similar spectrum with $MgCl_2$ chemical, indicating that "initial state" is still $MgCl_2$. After the initial lithiation, adsorption at 1302 eV was newly observed. This is also observed in Mg metal.[5] Therefore, $MgCl_2$ is reduced to form Mg metal during lithiation process. After the following delithiation, similar spectrum with initial state was observed, indicating that $MgCl_2$ is reversibly formed after the delithiation process. Cl K-edge X-ray adsorption spectroscopy for the $MgCl_2$ electrode before and after the discharge-charge were also measured. Initial state and delithiated state were similar spectra with that of $MgCl_2$. After lithiation, the main intense peak was slightly shifted to higher energy. This corresponds to the adsorption observed in LiCl.[6] From these results, it was confirmed that following reaction is occurred in the $MgCl_2$ anode as shown in Fig. 1.

$MgCl_2 + 2Li^+ + 2e^- \rightarrow 2LiCl + Mg$ (1)

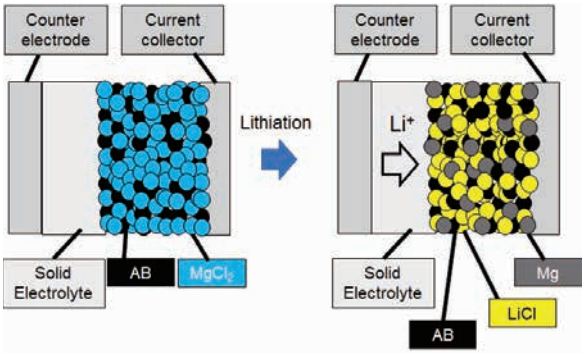

Fig. 1. Schematic view of "in-situ forming of solid electrolyte" in $MgCl_2$ electrode using $Li/LiBH_4/MgCl_2$ cell.

[1] H. Sato, R. Sakamoto, H. Minami, H. Izumi, K. Ideta, A. Inoishi, S. Okada, Chem. Commun, **57** (2021) 2605.
[2] A. Inoishi, H. Sato, Y. Chen, H. Saito, R. Sakamoto, H. Sakaebe, S. Okada, *RSC Advances*, **12** (2022) 10749.
[3] E. Kobayashi, J. Meikaku, T. Okajima, and H. Setoyama, Japanese Patent No. 5234994.
[4] E. Kobayashi, J. Meikaku, H. Setoyama, T. Okajima, J. Surf. Anal., **19** (2012) 2.
[5] J. W. Chiou, H. M. Tsai, C. W. Pao, K. P. Krishna Kumar, S. C. Ray, F. Z. Chien, W. F. Pong, App. Phys. Lett. **89** (2006) 043121.
[6] H. S. Lee, X. Q. Yang, J. McBreen, L. S. Choi, Y. Okamoto, J. Electrochem. Soc. **143** (1996) 3825.

BL3U

Direct Observation of Electrochemically Generated High Valent Iron-Oxo Species of μ-Nitrido-Bridged Iron Phthalocyanine Dimer Deposited on Graphite Surface by Soft X-ray Absorption Spectroscopy

Y. Yamada [1, 2] and M. Nagasaka[3]

[1]*Department of Chemistry, Graduate School of Science, Nagoya University, Furo-cho, Chikusa-ku, Nagoya 464-8602, Japan*

[2]*Research Center for Materials Science, Nagoya University, Furo-cho, Chikusa-ku, Nagoya 464-8602, Japan*

[3]*Institute for Molecular Science, Myodaiji, Okazaki 444-8585, Japan*

CH_4 is expected as a next generation carbon resource because it is abundant in nature as natural gas or methane hydrate. Therefore, development of novel catalysts that convert CH_4 into valuable raw chemicals efficiently is strongly desired. However, high chemical stability of CH_4 makes it highly challenging. We recently reported that a μ-nitrido-bridged iron phthalocyanine dimer closely stacked on a graphite surface **1**/G (Fig. 1a) efficiently convert CH_4 into methanol, formaldehyde, and formic acid in an acidic aqueous solution containing excess H_2O_2 at a temperature below than 100 °C. It was demonstrated that **1**/G showed especially potent CH_4 oxidation catalyst among a variety of molecule-based CH_4 oxidation catalysts and its catalytic activity was almost comparable to that of a natural particulate methane monooxgenase (pMMO)[1].

In order to advance the chemistry of **1**/G, we next attempted to develop the method for electrochemical generation of $\mathbf{1}_{oxo}$/G. It is expected that $\mathbf{1}_{oxo}$/G could be generated by oxidation of coordinating H_2O on the iron center of **1**(H_2O)/G in an aqueous solution (Fig. 1b). This method is expected to provide a more economically favored approach for CH_4 oxidation.

We first prepared a SiN membrane tip modified by **1**/G. A SiN membrane tip modified with 20 nm thickness of carbon membrane (cmSiN) was treated with a pyridine solution of **1**, followed by washing with trifluoroacetic acid and H_2O to give a SiN membrane tip modified by **1**/G (**1**/cmSiN). It was confirmed that **1** was successfully deposited on the carbon surface of cmSiN (Fig. 2a) by using cyclic voltammogram in an CH_3CN solution containing 100 mM $^n Bu_4N^+ \cdot PF_6^-$.

Electrochemical generation of the high-valent iron-oxo species from **1**(H_2O)/cmSiN (Fig. 2b) was monitored by O K-edge XAS spectra in a 100 mM phosphate buffer (pH = 7.0) by using a beamline equipped with a transmission-type liquid flow cell in BL3U of UVSOR [2]. The measurements were performed by changing the applied voltage to **1**(H_2O)/cmSiN. The spectra were obtained by the Lambert-Beer law, $\ln(I_0/I)$, where I_0 is the transmission signals of the cmSiN in buffer and I is those of **1**(H_2O)/cmSiN at different applied voltage in buffer.

It was found that the broad peak around 532 eV was apparently appeared when applying the voltage of 1.8 V vs. Ag/AgCl (Fig. 2c). Taking that DFT calculation indicated that the peak of O1s – π* of Fe=O for $\mathbf{1}_{oxo}$ should appear at around 529 eV, whereas the peaks for **1** having a coordinating H_2O should be observed at higher energy than 534 eV, it is considered that the peak appeared at around 532 eV is assignable to the excitation of O1s – π* of Fe=O of electrochemically generated high-valent iron-oxo species of **1**(H_2O)/cmSiN ($\mathbf{1}_{oxo}$/cmSiN). We are going to check the CH_4 oxidation activity of electrochemically generated $\mathbf{1}_{oxo}$/cmSiN.

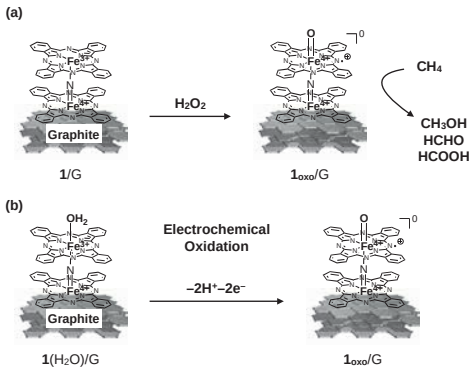

Fig. 1. Generation of $\mathbf{1}_{oxo}$/G from **1**/G (a) by using H_2O_2 or (b) by electrochemical oxidation.

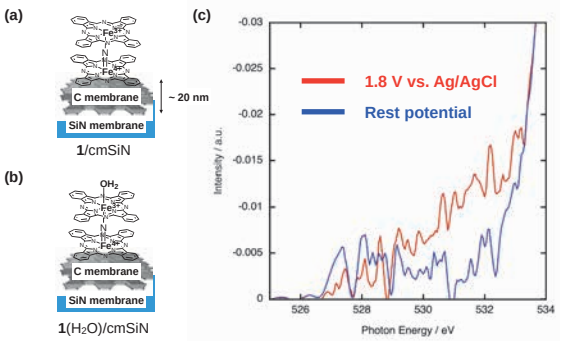

Fig. 2. Structures of (a) **1**/cmSiN and (b) **1**(H_2O)/cmSiN. (c) Comparison of O K-edge XAS spectra of **1**(H_2O)/cmSiN at rest potential (blue) and **1**(H_2O)/cmSiN at the applied potential of 1.8 V vs. Ag/AgCl.

[1] Y. Yamada, M. Nagasaka *et al.*, *JACS Au.* DOI : 10.1021/jacsau.2c00618.

[2] M. Nagasaka and N, Kosugi, *Chem. Lett.* **50** (2021) 956.

BL3U

Structural Analysis of fluoro-polymers Using Resonant Soft x-ray Scattering

K. Yamanoi [1, 2], M. Yamashita[1], Y. Yamamoto[1], H. Iwayama[3] and M. Noumi[2]
[1]*Institute of Laser Engineering, Osaka university, Suita, Osaka, 565-0871, Japan*
[2]*DAIKIN Industries Ltd, Settsu, Osaka, 566-8585, Japan*
[3]*UVSOR Synchrotron Facility, Institute for Molecular Science, Okazaki 444-8585, Japan*

Fluoropolymers or sometimes referred to as fluororesins have been widely used for chemical, electrical, and medical applications because of their high chemical resistance, mechanical strength, hydrophobicity, heat resistance, low surface energies, low coefficients of friction, and low dielectric constants [1-3]. These favorable properties stem from the electronic structure of the fluorine (F) atom, the stable carbon-fluorine (C-F) covalent bond, and the unique intramolecular and intermolecular interactions between the polymers' fluorinated segments and main chains [4]. Based on their structure and composition, fluoropolymers can be classified as partially fluorinated polymers or perfluoropolymers. Partially fluorinated polymers contain F and hydrogen (H) atoms in their structures, while perfluoropolymers only contain F atoms, i.e., the H atoms are replaced with F atoms. For example, polyvinylidene fluoride (PVdF) is a very processable and mechanically strong partially fluorinated polymer, whereas polytetrafluoroethylene (PTFE) is a chemically strong and heat-resistant perfluoropolymer.

Among their different applications, modified PTFE which includes oxygen component in the polymer is used to fuel injectors and as packing and linings of high-pressure vessels. Consequently, the ability to directly observe the oxygen related microscopic morphology is very important in revealing polymer function. As PTFE is known to have semi-crystalline, lamellar structures consisting of both amorphous and crystal phases [5], small-angle x-ray scattering (SAXS) technique is the most appropriate method to study the internal morphologies of these fluoropolymers within the 10 to 100-nm range. Additionally, the Resonant Soft X-ray Scattering (RSoXS) is attractive method to observe the structure related with specific chemical bond in mesoscopic region.

Previously, SAXS has been used to investigate the morphology of PTFE and their co-polymers under supercritical carbon dioxide condition [6]. In this research the RSoXS method was used in BL3U, UVSOR facility on the modified PTFE sample.

The sample was sliced to 1 μm thickness and sandwiched with Si_3N_4 membrane. Soft x-ray is irradiated on the sample through the Si_3N_4 membrane and the scattered soft x-ray is monitored by camera at the position of 2θ=7.5 and 30°. The x-ray energy is tuned at 540 eV which is resonant with oxygen bonging in polymer.

Figure 1 shows the results of scattering patterns of 540 eV comparing with the 528 eV which is not resonant with oxygen bonding.

We could observe the difference around the higher angle corresponding to smaller structure between resonant and non-resonant x-rays. This result shows the oxygen bonding related structure has the smaller crystal structure compared with others, however the scattered x-ray signal was weak since the sample was much thick. For the detailed discussion of oxygen bonding related structure, more thinner sample is required.

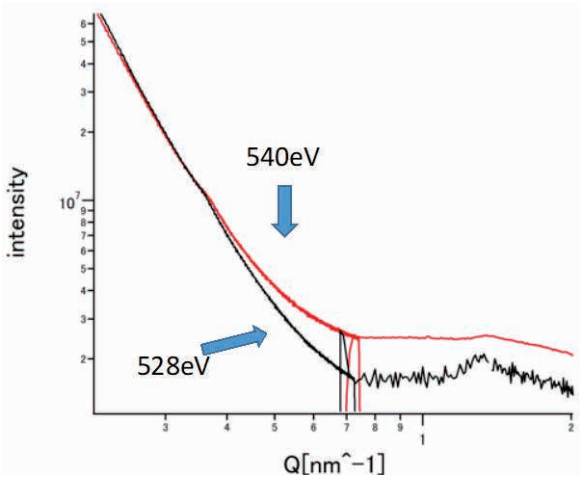

Fig. 1. Scattering patterns of RSoXS with 540 eV and 528 eV

[1] S. Ebnesajjad, P. R. Khaladkar, Fluoropolymer applications in the chemical processing industries (Second Edition), William Andrew Publishing (2017).
[2] Z. Cui, E. Drioli, Y. M. Lee, Prog. Polym. Sci. **39** (2014) 164.
[3] G. Eberle, H. Schmidt, W. Eisenmenger, IEEE Trans. Dielectr. Electr. Insul. **3** (1996) 624.
[4] H. Teng, Appl. Sci **2** (2012) 496.
[5] A. Marigo, C. Marega, R. Zannetti, G. Ajroldi, Macromolecules **29** (1996) 2197.
[6] K. Yamanoi, S. Shibuta, A. Shiro, M. Noumi, M. J. F. Empizo, M. Cadatal-Raduban, N. Sarukura, K. Nishikawa, and T. Morita, J. Supercrit. Fluids, May 2022 **vol. 184** (2022) 105555.

BL3U

Structure Analysis on Chiral Dark Conglomerate of Achiral Liquid Crystal Trimers by Resonant Soft X-ray Scattering (RSoXS) at UVSOR

Y. Takanishi[1], F. Araoka[2] and H. Iwayama[3,4]

[1]*Faculty of Science, Kyoto University, Kitashirakawa-oiwake, Sakyo, Kyoto, 606-8502, Japan*
[2]*RIKEN Center for Emergent Matter Science, Hirosawa 2-1, Wako, Saitama 351-0198, Japan*
[3]*UVSOR Synchrotron Facility, Institute for Molecular Science, Okazaki 444-8585, Japan*
[4]*School of Physical Sciences, The Graduate University for Advanced Studies (SOKENDAI), Okazaki 444-8585, Japan*

Spontaneous chiral symmetry breaking in soft matter is one of most attractive topics. Liquid crystal (LC) is a typical one of soft matter, and bent-core molecules show unique LC phases. The B4 phase is the lowest temperature phase observed in the bent-core liquid crystals, and it shows spontaneously chiral separated domains despite of achiral molecules. Recently it is reported that some kinds of rod-like LC trimers also show similar DC phase caused by unique molecular packing by designing intermolecular interactions. Yoshizawa's group studied intensively achiral LC trimers exhibiting DC phase. They systematically synthesized LC trimers, and reported that the DC phase is stabilized in (a) equimolecular mixture of nematic and smectic trimers, (b) binary mixtures of a nematic trimer with biphenyl units at the center and cyano-biphenyl compound and (c) a single asymmetric trimer.

In resonant X-ray scattering, using X-ray whose energy is coincident with a certain atom absorption edge, the structure factor becomes a tensor instead of the scalar in conventional X-ray diffraction. Carbon K-edge resonant soft x-ray scattering (RSoXS) has been applied to study, and successful in obtaining the precise structures of polymer blends, block copolymer, and LCs. Recently one of authors (YT) studied the binary system between a rod-like cholesteric LC mixture and a bent-core LC showing B4, and found a new smectic structure that does not appear in only constituent molecules with wide temperature range was unexpectedly discovered. Last year, the structure of helical nano-filament of B4 phase in the nano phase separation of cholesteric liquid crystal mixture and a bent-core molecule was analyzed using RSoXS to study the effect on the nano-helical filament in this mixture. We summarized that the pitch of helical filament decreases and coherence of helical structure increases, which would be caused by the interaction between bent-core and rod-like molecules.[1]

In this study, we report the local nano-structure analysis of DC conglomerate phase in achiral LC trimer using resonant soft-X-ray scattering (RSoXS) technique. Small angle and wide angle scattering were measured and alkyl chain length dependence of rod-like molecules was discussed.

The experiment was performed at BL3U of UVSOR. Used achiral liquid crystal trimers are I-(m,n), as shown in Fig. 1. In this study, m is fixed to 9, and n changes from 7~11. Samples used were filled in the isotropic phase between two pieces of 100 nm-thick Si_3N_4 membranes (Norcada). The scattering was detected by CCD (ANDOR DO940P-BN). Incident X-ray beam was tuned between 270~300eV. In these compounds, carbon K-edge energy was 284.5 eV.

Figure 2 shows 2D small-angle RSoXS images of (a) I-(9,7), (b)I-(9,9) and (c)I-(9,11). Resonant scattering peaks are clearly observed, and with the increase of spacer chain length n, the long-range periodicity corresponding to the peak increases from ca. 900~1300 nm. In I-(9,9), tubercle structures a are seen by STEM observation, but its diameter was about 200 nm, and hence our results suggest the existence of the longer-range periodic structure.

Figure 3 shows 2D wide-angle RSoXS images of (a) I-(9,7), (b)I-(9,9) and (c)I-(9,11). Even in these images, clear sharp peaks are observed, and the corresponding periodicity are ca. 70~80Å, which increases with the increase in the spacer chain length n. Since the layer thickness by conventional X-ray scattering are ca.40Å, these results indicate that LC trimers form intercalated bilayer structure.

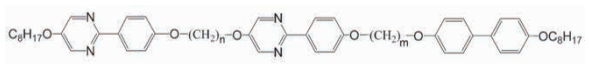

Fig. 1. Chemical structure of I-(m,n).

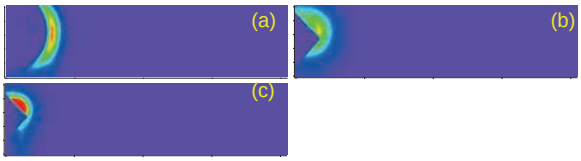

Fig. 2. 2D small-angle RSoXS images of (a)I-(9,7), (b) I-(9,9) and (c)I-(9,11).

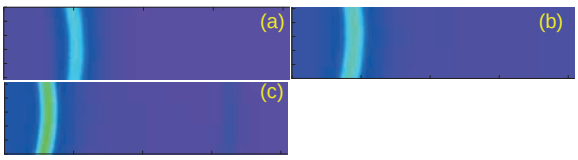

Fig. 3. 2D wide-angle RSoXS images of (a)I-(9,7), (b) I-(9,9) and (c)I-(9,11).

[1] Y. Takanishi, Soft Matter, **17** (2021) 563.

BL3B

Measurements of Fluorescence Lifetimes of Scintillators Adopted for a New in-beam Detector of the K_L^0 Rare Decay Experiment at J-PARC

K. Shintate, R. Abe, Y. Hayashi, T. Naito, S. Sakano, J. Ohashi, Y. Tajima and H.Y. Yoshida
Department of Physics, Yamagata University, 990-8560, Japan

J-PARC E-14 KOTO [1] is the experiment of searching for the direct CP violating decay $K_L \to \pi^0\nu\bar{\nu}$. This decay mode is considered to be sensitive to new physics beyond the Standard Model (SM), and its branching ratio is predicted to be 3.0×10^{-11} in the SM with about 2% theoretical uncertainly.

The cross-sectional view of the KOTO detector is shown in Fig.1. The upper limit currently obtained on the branching fraction of $K_L \to \pi^0\nu\bar{\nu}$ decay is 3.0×10^{-9} at the 90% confidence level [2].

One of the main backgrounds is caused by $K^{\pm}$ decays in the beam. To reduce this background by detecting $K^{\pm}$, we are planning to install an in-beam charged particle detector with a scintillator of 0.2 mm thickness named UCV (Upstream Charged Veto, Fig.2). The scintillator used for UCV is required to have sufficient light yield and short fluorescence lifetime. We measured fluorescence spectra and decay curves of the scintillator to evaluate the performance of UCV as a particle detector.

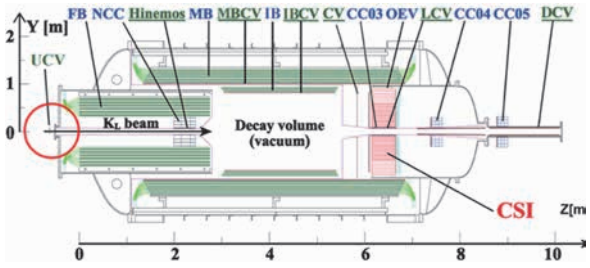

Fig. 1. Cross-sectional view of the KOTO detector. The beam enters from the left. Detector components with their abbreviated names written in blue (in green and underlined) are photon (charged-particle) veto counters. The UCV detector is installed at the upstream (left) end of the KOTO detector.

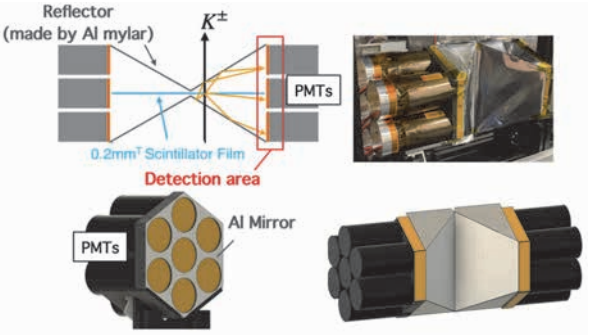

Fig. 2. The UCV detector. To install in the beam line, the scintillators are made as thin as 0.2mm thick and scintillating lights are detected by photomultiplier tubes (PMTs) using reflector sheets.

Fig. 3 shows the 2D fluorescence spectra of the UCV scintillator. Fig. 4 shows the decay curve for the 432 nm band under excitation at 284 nm. The blue line indicates experimental data. The red line is the fitting curve consists of two fluorescence lifetimes and reproduces the experimental data. The fitting results analyzed by using the data analysis framework named "ROOT" [3] are summarized in Table 1.

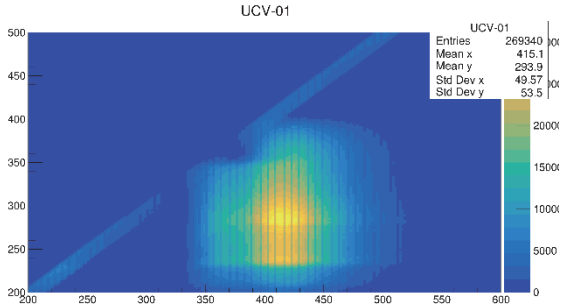

Fig. 3. 2D fluorescence spectra of the UCV scintillator. Y-axis is excitation wave length (nm), and x-axis is emission wave length (nm).

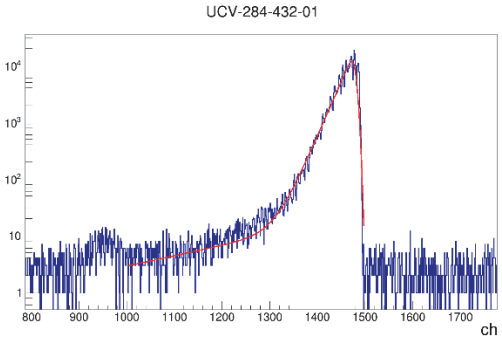

Fig. 4. Decay curve of the UCV scintillator for the 432 nm band under excitation at 284 nm.

Table 1. Fluorescence lifetimes of the UCV scintillator, determined from our data analysis.

Sample	λ_{EX} [nm]	λ_{EM} [nm]	τ_1[ns] (Ratio)	τ_2[ns] (Ratio)
UCV	284	432	1.9 (91.4%)	20.3 (8.6%)

[1] J. Comfort *et al.*, Proposal for $K_L \to \pi^0\nu\bar{\nu}$ Experiment at J-PARC (2006).
[2] J. Ahn *et al.* (KOTO Collaboration), Phys. Rev. Lett. **122** (2019) 021802.
[3] R. Brun and F. Rademakers, Nucl. Instrum. Methods Phys. Res. A **389** (1997) 81.

BL3B

Material Search of Li-Containing Halide Scintillators for Neutron Detection

C. Fujiwara[1,2], S. Kurosawa[2,3,4] and A. Yamaji[2,3]
[1]*Department of Materials Science, Graduate School of Engineering, Tohoku University, Sendai, Japan*
[2]*Institute for Materials Research (IMR), Tohoku University, Sendai, Japan*
[3]*New Industry Creation Hatchery Center (NICHe), Tohoku University, Sendai, Japan*
[4]*Institute of Laser Engineering, Osaka University, Osaka, Japan*

A remote real-time radiation detector consisting of a scintillator and optical fiber is required to achieve the decommissioning of the Fukushima Daiichi Nuclear Power Plant[1]. The scintillator for this application is required to have an emission wavelength of 550 nm or longer and high light output from the viewpoint of transmission efficiency in the optical fiber and reduction of optical fiber-derived noise[2][3]. In addition, neutrons-emitting debris is expected to be present inside the reactor, and neutron-sensitive scintillation materials are needed. Due to the above reason, we have developed Li_2HfI_6 as a candidate material [4], while Li_2HfI_6 contains a heavy element, Hf with a high detection efficiency for gamma rays. Therefore, in this study, Li_2ZrX_6 (X=Cl, Br, I) was prepared by replacing Hf with Zr, and its luminescence properties were investigated.

Li_2ZrX_6 crystal specimen was synthesized by the vertical Bridgman growth method in our laboratory using 99.9%-pure LiCl, LiBr and LiI powders, and 99%-pure $ZrCl_4$, $ZrBr_4$ and ZrI_4 powders were used. We measured the photoluminescence excitation and emission spectrum from 50 to 300K at UVSOR BL3B beam line.

As shown in Fig.1(a), Li_2ZrCl_6 showed broad luminescence with a peak at 570 nm at an excitation wavelength of 300 nm at 50K. Although the luminescence intensity decreased as the temperature increased, no significant change in both the excitation and emission wavelengths were observed. The emission wavelength was 580 nm at the excitation wavelength of 300 nm at room temperature. This wavelength range satisfies the above requirement, and Li_2ZrCl_6 can be a candidate material for neutron detection with optical fiber.

Fig.1(b) showed the emission spectrum of Li_2ZrBr_6 as a function of temperatures. Li_2ZrBr_6 shows a broad emission with a peak at 580 nm at an excitation wavelength of 305 nm at 50 K. When the temperature is increased, the emission intensity decreases, and the emission wavelength became shorter.

Fig. 1(c) shows the emission spectrum of Li_2ZrI_6, and Li_2ZrI_6 had red and near-infrared emission with the emission wavelength of 670 nm at an excitation wavelength of 430 nm at 50 K. However, the emission intensity decreases significantly as the temperature increases, and no emission is observed at room temperature.

From these results, $LiZrCl_6$ was found to be a candidate material for neutron detection using an optical fiber. In the future, we plan to investigate the light output by neutron excitation and conduct a detection test by connecting the optical fiber.

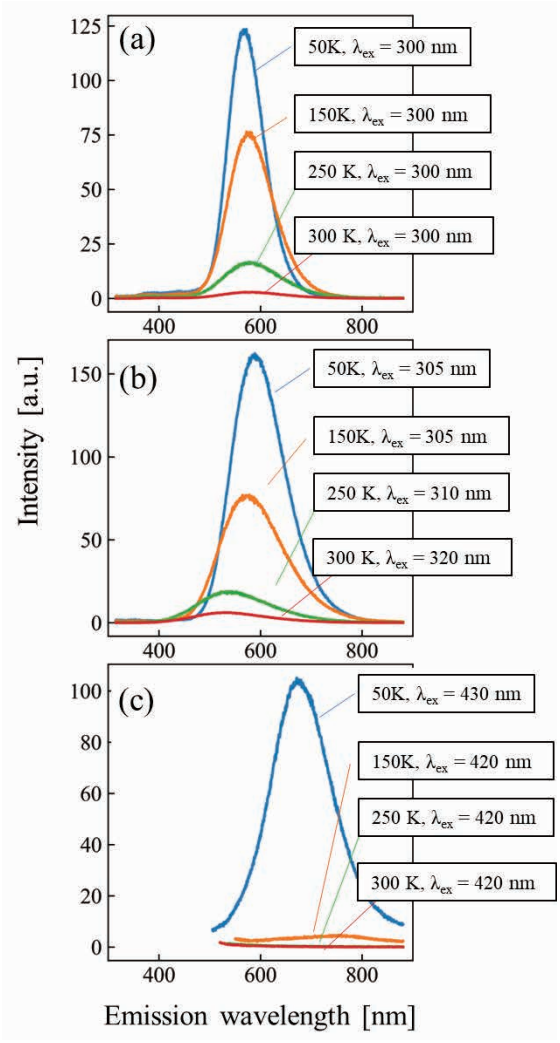

Fig. 1. Photoluminescence spectrum at each temperature for (a) Li_2ZrCl_6, (b)Li_2ZrBr_6, (c)Li_2ZrI_6

[1] I. Wakaida, Topic. Fukushima **70** (2015) 1.
[2] C. and H. Ltd, Opt. Quantum Electron **13** (1981) 85.
[3] H. Liu *et al.*, Rev. Sci. Instrum. **89** (2018) 083302.
[4] C. Fujiwara, K. Shunsuke, and Y. Akihiro, UVSOR Activity Report **49** (2021) 84.

BL3B

Optical Properties of Cs_2IrCl_6-CsCl Composite Phosphor

S. Kodama, S. Omiya, N. Shimoyama, T. Saito, I. Yanase and H. Takeda
Saitama University, Saitama 338-8570, Japan

Cs_2HfCl_6 was reported as the novel single-crystalline inorganic scintillator with a high light output and a good energy resolution [1]. Cs_2HfCl_6 exhibits the strong intrinsic luminescence at the blue region. Several luminescence origins were suggested for Cs_2HfCl_6 [2-3], however, the detailed mechanism was still unclear.

In this study, we focused on the charge transition transfer (CT) phenomena. Inorganic crystals which consist an isolated anion complex show the CT luminescence. In order to occur the CT luminescence, the peripheral electron orbital of the center metal ion in the anion complex should be empty. The crystal structure of Cs_2HfCl_6 consists Cs^+ ions and isolated $[HfCl_6]^{2-}$ anion complexes. In addition, the electron orbital of Hf^{4+} of $[HfCl_6]^{2-}$ anion complex is empty, thus we assumed that the intrinsic luminescence of Cs_2HfCl_6 can be attributed to be CT luminescence.

To distinguish the CT luminescence from other luminescence origins such as the self-trapped luminescence or the defect luminescence, therefore in this study, we synthesized Cs_2IrCl_6 and compared the optical properties with Cs_2HfCl_6. Although Cs_2IrCl_6 has the same crystal structure as Cs_2HfCl_6, the peripheral electron orbital of Ir^{4+} of $[IrCl_6]^{2-}$ is not empty, therefore, Cs_2IrCl_6 must not exhibit the CT luminescence. If some luminescence was observed in Cs_2IrCl_6, the CT luminescence should not occur in Cs_2HfCl_6.

Cs_2IrCl_6 was synthesized from the starting powders of CsCl and $IrCl_4$. The melted specimen included Cs_2IrCl_6 and CsCl phases, thus we represent the obtained specimen to be Cs_2IrCl_6-CsCl composite. Additionally, in order to compare the optical properties, non-doped CsCl and Ir:CsCl crystals were grown.

Figure 1 shows the photoluminescence spectra of Cs_2IrCl_6-CsCl composite, CsCl and Ir:CsCl. At 300K, all specimens showed the single emission peak at ~310 nm excited by 254 nm. In addition to ~310 nm band, all specimens showed another emission peak at ~420 nm at 300K. The emission peaks of Cs_2IrCl_6-CsCl composite and Ir:CsCl well corresponded to that of CsCl, therefore, Cs_2IrCl_6 was concluded to show no luminescence originated from the self-trapped excitons or defects. Based on the obtained results, the luminescence origin of Cs_2HfCl_6 might be assumed to be the CT luminescence.

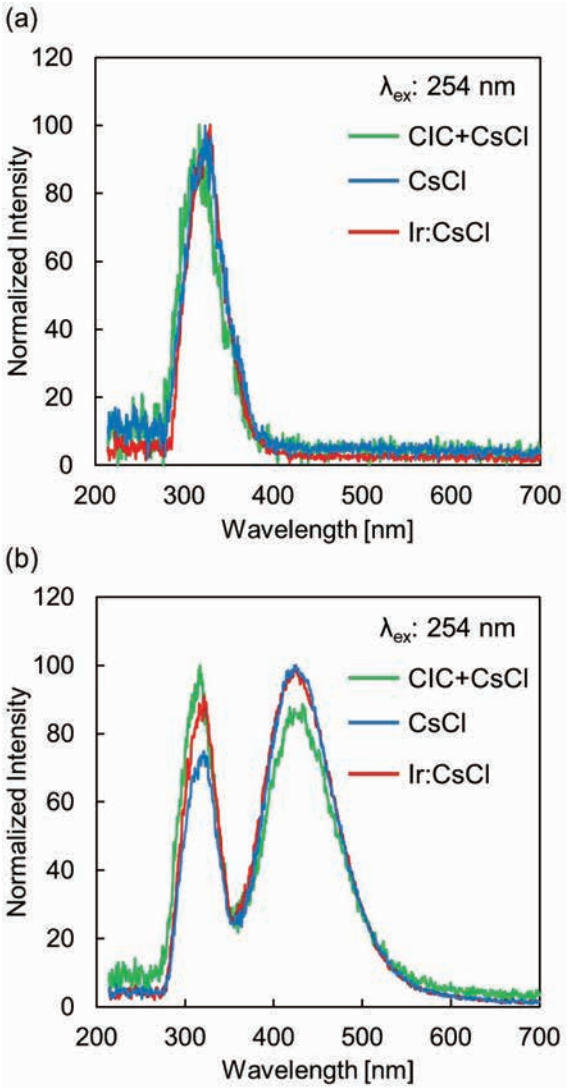

Fig. 1. Photoluminescence spectra of Cs_2IrCl_6-CsCl composite (represented as CIC+CsCl), CsCl and Ir:CsCl at (a) 300K and (b) 10K.

[1] A Burger *et al.*, Appl. Phys. Lett **107** (2015) 34.
[2] B. Kang and K. Biswas, J. Phys. Chem. C **120** (2016) 12187.
[3] R. Král *et al.*, J. Phys. Chem. C **121** (2017) 12375.

BL3B, 6B

Visible-to-Ultraviolet Spectral Change with the Current-Induced Local-to-Nonlocal Transition of SmS

H. Watanabe[1,2], S. Tatsukawa[2], K. Imura[3], H. S. Suzuki[4], N. K. Sato[5] and S. Kimura[1,2,6]
[1]*Graduate School of Frontier Biosciences, Osaka University, Suita 565-0871, Japan*
[2]*Department of Physics, Graduate School of Science, Osaka University, Toyonaka 560-0043, Japan*
[3]*Institute of Liberal Arts and Sciences, Nagoya University, Nagoya 464-8602, Japan*
[4]*Institute for Solid State Physics, The University of Tokyo, Kashiwa 277-8581, Japan*
[5]*Center for General Education, Aichi Institute of Technology, Toyota, 470-0392 Japan*
[6]*Institute for Molecular Science, Okazaki 444-8585, Japan*

Samarium monosulfide SmS exhibits the phase transition from a black-colored semiconductor to a golden-colored metal (BGT) by applying pressure above 0.7 GPa [1,2]. The origin of the BGT is now still under debate. Among the possible origins, the transition between Bose-Einstein condensation and BCS state of excitons is currently being discussed [3,4], but no definitive evidence has been obtained. Recently, Ando *et al.* reported the nonlinear relation between the voltage (V) and electric current (I) with increasing current at lower temperatures than 100 K, which suggests a drastic change in the electrical resistivity [5]. It is unclear whether the nonlinear V/I relation is related to pressure-induced BGT. To clarify the origin of the nonlinear V/I curve and its relation to the BGT, we have investigated the current and temperature dependencies of the reflectivity spectrum in the THz and IR regions. We have already reported the carrier character change from the high increasing rate (dN/dI) and the high relaxation time (τ) of carriers at the region of low temperature and low current to low dN/dI and low τ at high temperature or high current regions [6,7].

The origin of the character change of carriers can be attributed to an electron delocalization, in which the localized electrons trapped at Sm sites start moving by the applied current. In this case, the electronic structure is modified, and finally, the band gap is expected to be closed, but it has not been revealed. In the visible-ultraviolet region, there are excitations from occupied 4*f* states to the unoccupied 5*d* states. It is expected to be able to observe changes in the reflectivity spectrum due to the modification in the electronic structure, such as a band gap narrowing. To observe the current-induced spectral change in SmS, we measured the current dependence of the visible-ultraviolet reflectance at BL3B.

Single crystalline SmS with a typical sample size of 1×1×1 mm^3 was sandwiched by the electrodes connected to the current source. The sample was cooled down to 30 K during the experiment.

Figure 1 shows the applied current dependence of the visible-ultraviolet reflectivity spectrum. With increasing applied current, the intensity of a peak at 3 eV decreases, and a shoulder at about 6 eV shifts to low energy. In addition to the spectral change, an oscillation in reflectivity appeared between 4 to 6 eV, which is expected to be due to a change in the surface condition, but the exact origin is not clarified. From these results, although we observed a slight change in the reflectivity spectrum in the visible-ultraviolet region due to the current application, these could not suggest a drastic change in the electronic structure, such as a shift in the overall band structure due to a change of the band gap.

In summary, the application of electric current gives energy to the electrons, causing delocalization. However, the results suggest that the applied current does not influence the electronic structure far from the Fermi level.

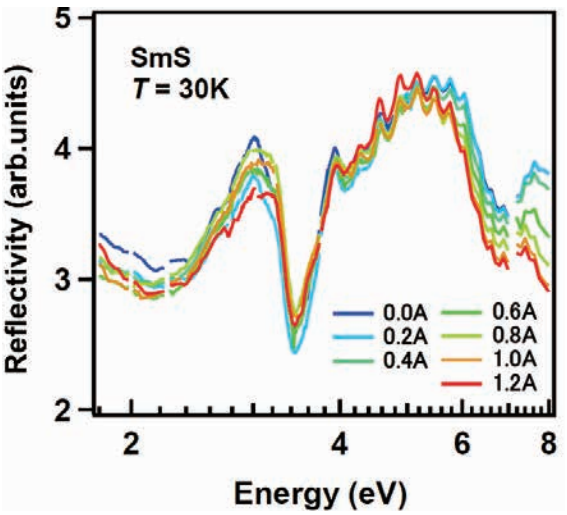

Fig. 1. Current dependence of the visible-to-ultraviolet reflectivity spectrum of SmS at 30 K.

[1] A. Jayaraman *et al.*, PRL **25** (1970) 1430.
[2] T. Mizuno *et al.*, JPSJ **77** (2008) 113704.
[3] B. I. Halperin and T. M. Rice, RMP **40** (1968) 755.
[4] S. Watanabe, JPSJ **90** (2021) 023706.
[5] H. Ando *et al.*, JPS Conf. Proc. **30** (2020) 011132.
[6] H. Watanabe *et al*, *UVSOR Activity Report 2021* (2022) 92.
[7] S. Kimura *et al.*, arXiv: 2302.12998 (2023).

BL3B

Exciton States of Cesium Silver Iodide Crystals

S. Ibuki and T. Kawai
Graduate School of science, Osaka Metropolitan University, Sakai 599-8531, Japan

In the past decade, ternary lead halides have attracted wide interest in the field of applications, including scintillator materials, photodetectors, and solar cells [1]. However, the environmental toxicity of the lead is among the significant concerns in this field. Therefore, considerable efforts have been devoted to developing alternative eco-friendly lead-free ternary metal halide. In this study, we focused on ternary sliver iodides such as $CsAg_2I_3$.

$CsAg_2I_3$ compounds were obtained by the Bridgman method from high purity CsI and AgI powders, which were mixed in a stoichiometric ratio. The thin crystals of $CsAg_2I_3$ were prepared by a cell method [2]. The quartz-cells with the narrow gap are made of a pair of two quartz plates. The melt of $CsAg_2I_3$ compounds was percolated into the gap of the quartz-cells through capillary action and the thin crystals were grown in the gap by natural cooling.

Figure 1 shows the reflection spectrum of the $CsAg_2I_3$ crystal at 12 K in the energy region of 3.5 ~ 6.5 eV. The sharp dispersion-like structures due to band-edge excitons are observed around 3.8 eV. Furthermore, the broad reflection peaks are observed around 4.6 and 5.1 eV. The energy values are consistent with those of the absorption bands reported in a previous paper [3].

Now, we confine one's attention to the dispersion-like structures due to the band-edge excitons around 3.8 eV. The reflection spectrum magnified around the dispersion-like structures is shown in Fig.2. Two dispersion-like structures are confirmed. We attempted to fit the reflection structures by using the simple oscillators model with two close-lying resonances. Then, the dielectric function is represented by the following expression:

$$\varepsilon(\omega) = \varepsilon_r + i\varepsilon_i = \varepsilon_b + \frac{f_1}{\omega_{ex1}^2 - \omega^2 - i\omega\gamma_1} + \frac{f_2}{\omega_{ex2}^2 - \omega^2 - i\omega\gamma_2}$$

where ε_r and ε_i are the real and imaginary parts of the dielectric constant, respectively, $\omega_{ex1,2}$ is the resonance frequency of the excitons, ε_b the background dielectric constant, $f_{1,2}$ oscillator strength, and γ the damping constant. The reflectance R is given by

$$R = \frac{1 + |\varepsilon| - \sqrt{2(|\varepsilon| + \varepsilon_r)}}{1 + |\varepsilon| + \sqrt{2(|\varepsilon| + \varepsilon_r)}}$$

where $|\varepsilon| = (\varepsilon_r^2 + \varepsilon_i^2)^{1/2}$. From the best-fitting analysis, which is shown by the broken curve in Fig.2, the resonance energies of the excitons were estimated to be 3.78 and 3.87 eV.

As future works, we are planning to investigate the optical properties of ternary sliver iodides such as Cs_2AgI_3.

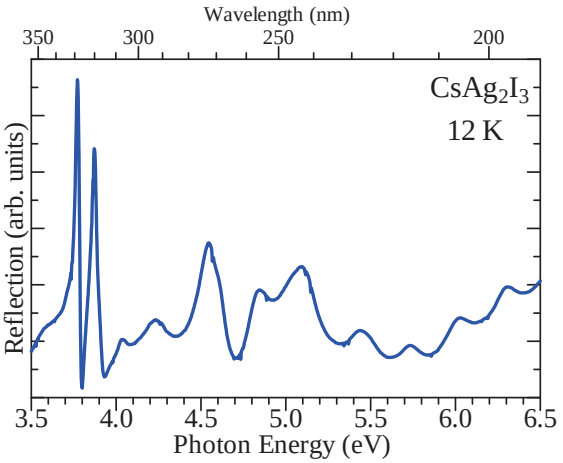

Fig. 1. Reflection spectrum of the $CsAg_2I_3$ crystal at 12K.

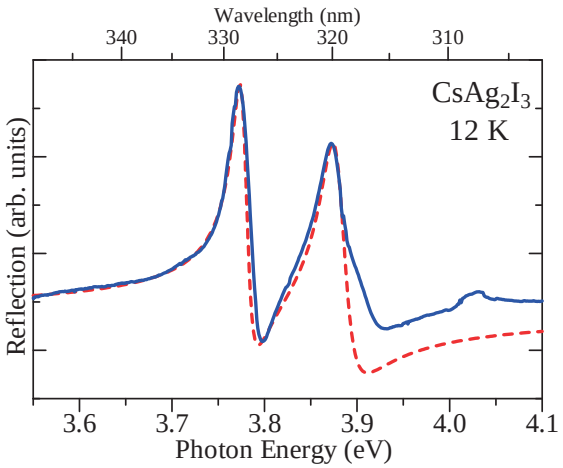

Fig. 2. Reflection spectrum of the $CsAg_2I_3$ crystals in the band-edge exciton region at 12 K. Broken curve is the fitting result calculated with the two-oscillator model.

[1] J. Yuan, *et. al*, Joule **4** (2020)1160.
[2] S. Hashimoto and M. Itoh, Jpn. J. Appl. Phys. **27** (1988) 726.
[3] V. K. Miloslavskii, *et. al*, Solid State Spectro. **80** (1996) 577.

BL3B

Temperature Dependence of Excitation Spectra in Er-doped $La_2Zr_2O_7$

M. Yoshino and M. Ito
Graduate School of Engineering, Nagoya University, Nagoya 464-8603, Japan

Based on our first-principles calculations, Er substituted for La in pyrochlore-type oxide, $La_2Zr_2O_7$ (LZO) has multiple stable positions with significant displacements from the original La position, and is expected to spread in a disc shape at room temperature. This combination of static and dynamic disorder produces diversity in the Er coordination environment, and the transition spectrum of Er^{3+} is expected to have a broad shape due to the overlap of each environment case. At low temperatures, the transition spectra become sharper due to the decrease in the dynamic disorder. Therefore, we measured the excitation spectra of Er-doped LZO from low temperature to room temperature. For comparison, we also measured Er-doped $Y_2Ti_2O_7$ (YTO) with pyrochlore-type structure, $Y_{0.5}Zr_{0.5}O_{1.75}$ (YZO) with defect fluorite structure, and $Y_3Ga_5O_{12}$ (YGG) with garnet-type structure. Er in YTO and YGG have small displacements, and Er in YZO has static disorder but less dynamic disorder, so the temperature dependence of their spectral shapes is expected to be small. Fig. 1 shows the excitation spectrum of LZO with emission wavelength of 560 nm. Results from 20 K to 100 K are shown here, but measurements were also performed up to 300 K. To examine the temperature dependence of the spectral shape, we normalized the spectra using the peak with the maximum intensity at 20 K. Fig. 2 and Fig. 3 show the results for YZO and YTO, respectively. In each case, the spectral shape becomes broader with increasing temperature. To compare their temperature dependences, we estimated the change in the height of the valley between peaks around 380 nm with respect to the 20 K case as shown in Fig. 4. It was found that LZO tends to have a larger change in the height of the valley than the other samples, resulting in broad spectra. This indicates that the temperature dependence is larger for LZO.

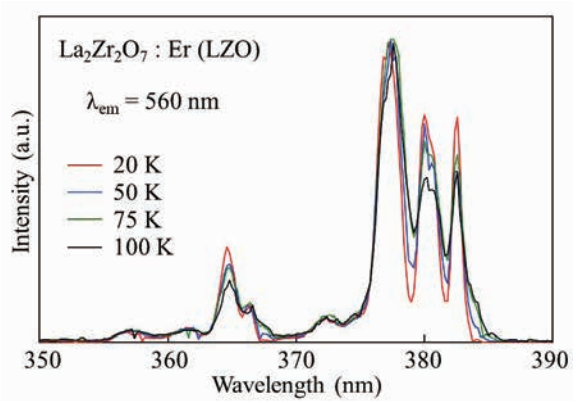

Fig. 1. Excitation spectra of $La_2Zr_2O_7$: Er (λ_{em} = 560 nm).

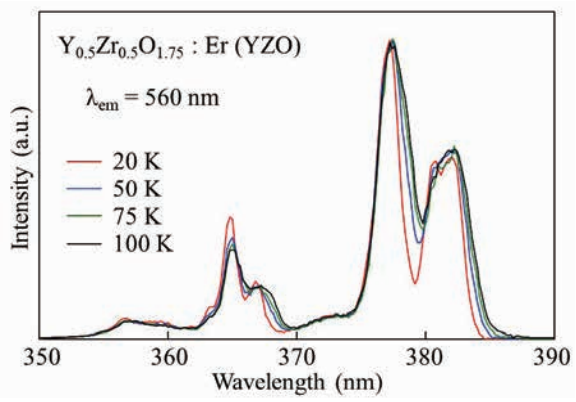

Fig. 2. Excitation spectra of $Y_2Zr_2O_7$: Er (λ_{em} = 560 nm).

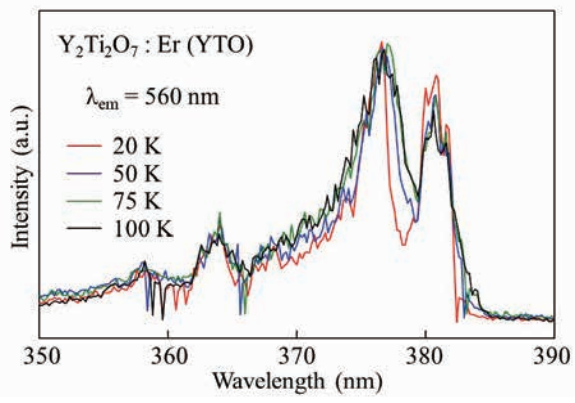

Fig. 3. Excitation spectra of $Y_2Ti_2O_7$: Er (λ_{em} = 560 nm).

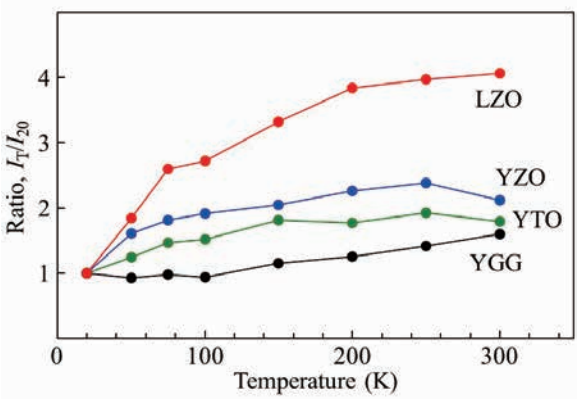

Fig. 4. Change in the height of the valley between peaks around 380 nm.

BL4U

Analysis of Cathode Materials for Li-Ion Batteries by STXM

E. Hosono[1,2,3], D. Asakura[1,2,3], H. Yuzawa[4], T. Ohigashi[4,5], W. Zhang[6], M. Kobayashi[7,8], H. Kiuchi[6] and Y. Harada[3,6,9]

[1]*Global Zero Emission Research Center, National Institute of Advanced Industrial Science and Technology (AIST), Tsukuba, Ibaraki 305-8569, Japan*
[2]*Research Institute for Energy Conservation, AIST, Tsukuba, Ibaraki 305-8565, Japan*
[3]*AIST-UTokyo Advanced Operando Measurement Technology Open Innovation Laboratory (Operando-OIL), Kashiwa, Chiba 277-8565, Japan*
[4]*UVSOR Synchrotron Facility, Institute for Molecular Science, Okazaki 444-8585, Japan*
[5]*School of Physical Sciences, The Graduate University for Advanced Studies (SOKENDAI), Okazaki 444-8585, Japan*
[6]*Institute for Solid State Physics (ISSP), The University of Tokyo, 5-1-5 Kashiwanoha, Kashiwa, Chiba 277-8581, Japan*
[7]*Department of Electrical Engineering and Information Systems, The University of Tokyo, 7-3-1 Hongo, Bunkyo-ku, Tokyo 113-8656, Japan*
[8]*Center for Spintronic Research Network, The University of Tokyo, 7-3-1 Hongo, Bunkyo-ku, Tokyo*
[9]*Synchrotron Radiation Research Organization, The University of Tokyo, 7-3-1 Hongo, Bunkyo-ku, Tokyo, 113-8656, Japan*

The development of clean energy devices is attracting attention toward the realization of a low-carbon society for preventing global warming. Since lithium ion batteries (LIBs) are expected to be broadly used for such as electric vehicles and stationary types for home use, their devices are the most actively investigated in both industry and academia fields. However, the market demand for improved performance of LIBs is still extremely high, and the development of innovative materials for LIBs is essential to exceed significantly the current performance. To solve this difficult problem, characterization of component materials for LIBs is crucially important.

We have been analyzing electrode active materials by absorption and emission spectroscopy using synchrotron soft X-rays in order to clarify the detailed electronic states of the materials. In addition, we have also been analyzing them by microscopic photoelectron spectroscopy using synchrotron soft X-rays. The LIBs are devices that stores energy by the insertion and diffusion of Li into the host crystal, which is strongly dependent on the local environment of the active materials. Therefore, local analysis can provide important information for understanding the charge-discharge mechanism. Photoelectron spectroscopy is a surface-sensitive method, while scanning transmission X-ray microscopy (STXM) is a bulk-sensitive method because of its transmission.

In this study, we applied STXM analysis to most famous LIB cathode material, $LiCoO_2$ (LCO). Figure 1 shows the Co L_3-edge X-ray absorption spectra (XAS) of the initial (dotted line) and charged (solid line) conditions of LCO. By using STXM, we were able to obtain XAS spectra of selected areas and visualize the distribution of the oxidation state of LCO. The details were reported in ref. [1].

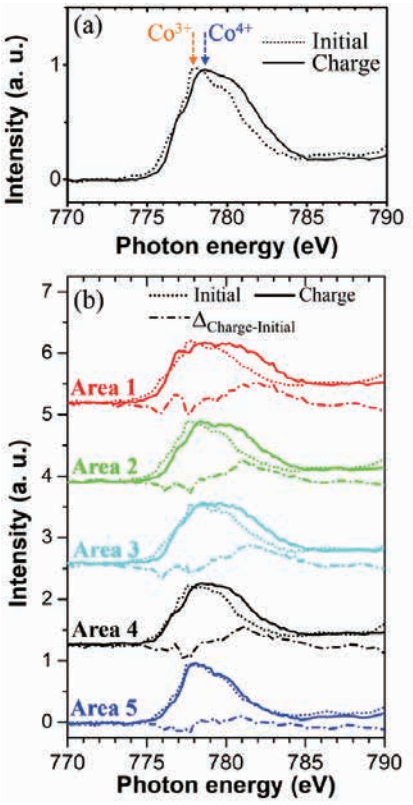

Fig. 1. Co L_3-edge XAS of the initial (dotted line) and charged (solid line) conditions of LCO. Panel (a) shows average spectra of selected particles including area 1-5 (circle areas: 300 nm diameter). Panel (b) shows extracted spectra from area 1-5, which exhibit different charging states (oxidation states) from each other.

[1] W.X. Zhang *et al.*, Sci. Rep. **13** (2023) 4639.

Unraveling the Origin of Irreversibility between the First and Second Charging Process in Primary Conversion Anode Particle

J. Kim [1], J. Chung[1], T. Ohigashi[2], H. Yuzawa[2] and J. Lim[1]
[1]*Department of Chemistry, Seoul National University; 1 Gwanak-ro, Gwanak-gu, Seoul 08826, Republic of Korea*
[2]*UVSOR Synchrotron Facility, Institute for Molecular Science, Okazaki 444-8585, Japan*

Among the various candidates for rechargeable lithium-ion battery anode, alpha-hematite (α-Fe_2O_3) has been actively investigated due to its high theoretical capacity (1007 mA·h/g), low processing cost, abundant remaining source, and nontoxicity. Despite these advantages, commercialization of α-Fe_2O_3 anode is challenging due to the fast capacity fading, particularly occurring in first and second charging process. A previous report proposed the three reaction pathways in the first charging process of α-Fe_2O_3 [1]. First step: monophasic insertion reaction; (1) $Fe_2O_3 + xLi^+ \rightarrow Li_xFe_2O_3$. Subsequent second and third steps: biphasic conversion reaction; (2) $Li_xFe_2O_3 + (2\text{-}x)\ Li^+ \rightarrow 2FeO + Li_2O$ and (3) $2FeO + 4Li^+ \rightarrow 2Fe + 2Li_2O$. From our electrochemistry data (**Fig. 1**), it shows that the voltage plateau in the first charging is attributed to (2) and (3) distinct conversion reactions. Since this conversion reaction produces an (ir)reversible reaction product (i.e., Li_2O), we hypothesize that the local reaction pathway of subsequent electrochemical cycles could be influenced by the site-specific Li_2O formation in first cycle. The Li_2O, well-known insulating material, increases reaction overpotential which allows the sluggish reaction kinetics of the host material.

To reveal this degradation mechanism, we note that the nanoscale chemical distribution of α-Fe_2O_3 single particle at first charged/discharged states should be identified. The compositional heterogeneity within the intraparticle in first charging process allows us to investigate non-uniform intraparticle distribution of Li_2O, which insulates the subsequent electrochemical reaction. Furthermore, to unravel reaction hysteresis in first battery cycle in Fig. 1, it is essential for capturing the chemical distribution of α-Fe_2O_3 at first discharged state which are entangled with the first charging process. Thus, we conducted ex-situ STXM measurement of first charged/discharged states of α-Fe_2O_3 at UVSOR BL4U.

Fig. 2 shows chemical composition maps at pristine, first charged state, and first discharged state, revealing that chemical distribution of Fe phases is inhomogeneous within the single particle. In Fig 2b, fully charged Fe phase (Fe^0) was partially formed and randomly distributed, suggesting that insulating Li_2O species was generated in the first charge regardless of any specific location. In Fig. 2c, the discharging end phase was not fully recovered to the pristine state (Fe^{3+}). This observation correlates with some previous reports [2, 3], claiming that existence of various discharging reaction pathways; (4) $2Fe + 3Li_2O \rightarrow Fe_2O_3 + 6Li^+$, (5) $Fe + Li_2O \rightarrow FeO + 2Li^+$ and (6) $3Li_2O + 2Fe \rightarrow 1.5LiFeO_2 + 0.5Fe$. From our results, we conclude that intraparticle heterogeneity evolves in first charging process (conversion reaction) and this inhomogeneity could be affected by the distribution of the reaction product (Li_2O), resulting in irreversibility of (dis) charging process.

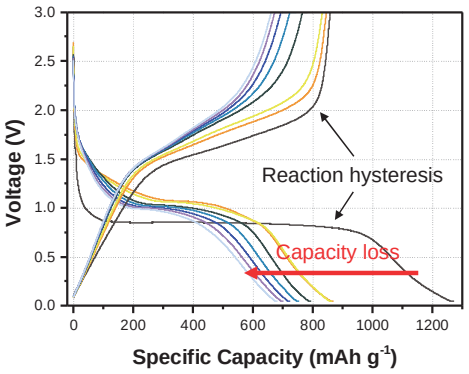

Fig. 1. Charge/discharge profiles of the synthesized α-Fe_2O_3 at 0.1 C current rate. (Unpublished)

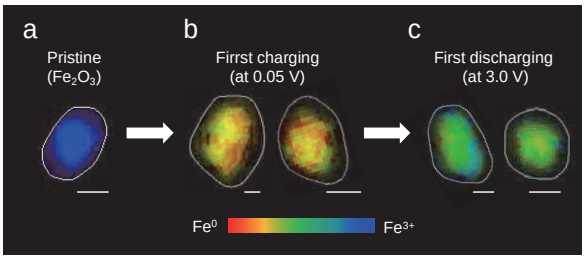

Fig. 2. Chemical composition maps at **a.** pristine, **b.** first charged state (0.05 V vs. Li/Li^+), and **c.** first discharged state (3.0 V vs. Li/Li^+). Scale bars below each image are 1 um.

[1] A. Banerjee, *et al.*, Nano Energy **2** (2013) 890.
[2] T. C. Christie, *et al.*, Journal of Materials Chemistry **22** (2012) 12198.
[3] Su. Qingmei, *et al.*, ACS Nano **7** (2013) 9115.

BL4U

Chemical Bonding Structures of SBR/BR Interfaces

T. Ejima[1] and Y. Tamura[2]
[1]*SRIS, Tohoku University, Sendai 980-8577, Japan*
[2]*ENEOS Materials Corp., Yokkaichi 510-0871, Japan*

Rubber materials used in tires often have multiple elastomers to achieve desired properties. Combining styrene-butadiene rubber (SBR) and butadiene rubber (BR) can enhance skid and rolling resistance, but increasing styrene content can reduce low-temperature performance. By using high cis-1,4 BR instead of BR and adding it to SBR, the glass transition temperature (Tg) can be controlled, and low-temperature performance can improve [1-3]. The study used SBR and BR to fabricate interface structures with NEXAFS spectra, clarifying chemical bonding states. Understanding these states can clarify complex elastomer properties.

The preparation of the samples involved compounding SBR-A, SBR-B, and BR with a 75 ml plast mill (Toyo Seiki). The difference of the types of SBR is the difference of the crosslink density: The A type SBR (SBR-A) is normal one and the B type has a high crosslink density (SBR-B). The prepared samples were then cut into sheet shapes, and these sheets were subsequently laminated together to form a SBR-A/BR interface sheet and a SBR-B/BR interface sheet. Furthermore, a sample SBR-B/BR was kneaded by compounding SBR-B and BR at a ratio of 70:30. The resulting SBR-A/BR and SBR-B/BR interface sheets and kneaded SBR-B/BR sheet were sliced using an ultramicrotome, placed on an electron microscope grid, fixed to a dedicated STXM sample holder. The thickness of the sample was fixed at 100 nm.

The soft X-ray image of the SBR-B/BR interface sample shows the existence of a region near the interface that exhibits a spectral structure different from that of the SBR-B and BR used to prepare the sample The two-dimensional (2D) soft X-ray absorption distributions of the SBR-B phase, the BR phase, and the residual phase are shown in Fig. 1(a). In the figure, the absorption intensity of the BR phase is shown in red, the SBR-B phase in blue, and the residual phase in green. The respective absorption intensities are represented by the respective color gradations. The simultaneously obtained spectra of the BR phase, the SBR-B phase, and the residual phase are shown in Fig. 1 (b). The color of the spectra corresponds to the color in the soft X-ray image of Fig. 1(a). The spectral intensities are normalized by the background before and after the absorption edge.

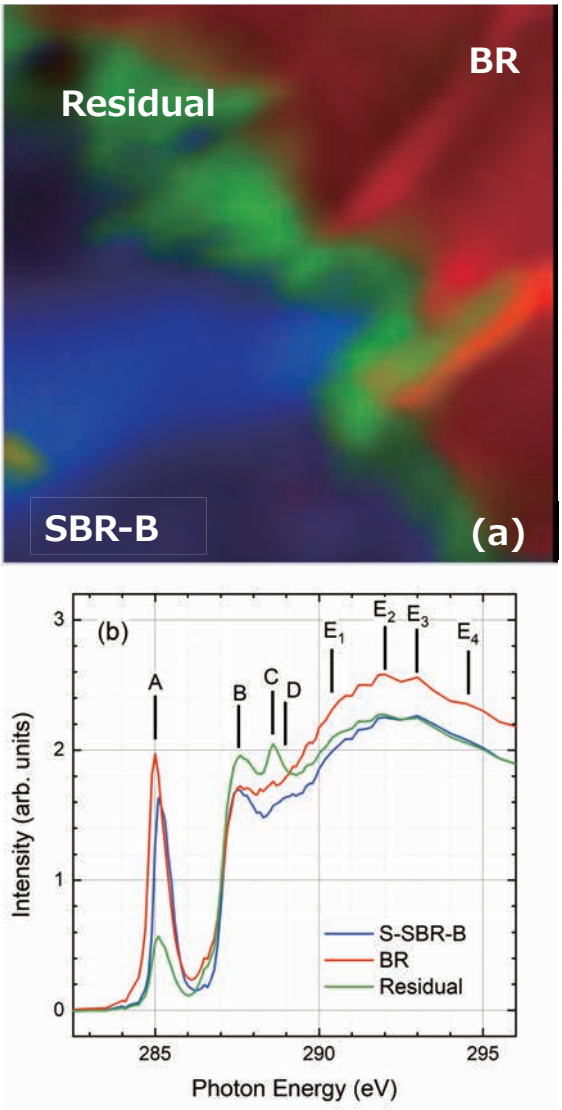

Fig. 1. (a) Material separation image of S-SBR-B/BR interface sample, (b) NEXAFS spectra of each material obtained in (a).

[1] A. J. Marzocca, *et al.*, Polym. Int. **49** (2000) 216.
[2] J. M. Massie, *et al.*, Rubber Chem. Technol. **66** (1993) 276.
[3]H. H. Le, *et al.*, Macromol. Mater. Eng. **298** (2013) 1085.

BL4U

Observation of Distribution of Sulfur and cross-linking Reagent in Vulcanized Rubber by Using STXM

T. Ohigashi[1, 2, 3], F. Kaneko[4], H. Yuzawa[2] and H. Kishimoto[4]

[1]*Institute of Material Structure Science, High Energy Accelerator Research Organization, Tsukuba 305-0801, Japan*

[2]*UVSOR Synchrotron Facility, Institute for Molecular Science, Okazaki 444-8585, Japan*

[3]*School of Physical Sciences, The Graduate University for Advanced Studies (SOKENDAI), Tsukuba 305-0801, Japan*

[4]*Sumitomo Rubber Industries Ltd., Kobe 651-0072, Japan*

In recent years, SDGs (Sustainable Development Goals) is a keyword to represent attitude of our daily life. Especially, reduction of mass consumption is a critical issue. Rubber is one of the important resources and its demand is assumed to increase especially according to growth of car industries. To reduce its consumption, establish of LCA (Life Cycle Assessment) of rubber industrialization and further improvement of functionality of rubbers, such as wear- and destruction-resistant, are essential.

Rubber is generally heterogeneous network structure, which is produced by rubber polymer and cross-linking agent (vulcanization). Since the remained cross-linking reagent in this structure is heterogeneously distributed, it gathers internal stress of rubber deformation to cause the destruction. Therefore, dispersion of a cross-linking reagent in the rubber is an important parameter to determine mechanical character of rubber. However, it is not easy to observe the dispersion because the cross-linking reagent in rubber is so small amount and is consisted of light elements.

We have been characterized rubber by using scanning transmission X-ray microscopy (STXM) at BL4U [1,2]. STXM is a powerful tool to obtain 2-dimensional X-ray absorption spectroscopy by near edge X-ray absorption fine structure (NEXAFS) with high spatial resolution around 30 nm. Moreover, STXM gives much less radiation damage to the sample than by electron microscopy. Therefore, STXM is the best approach for this study. In this report, the distribution of cross-linking reagent in vulcanized rubber is investigated by STXM.

The sample is styrene-butadiene rubber with zinc oxide,sulfur,N-cyclohexyl-2-Benzothiazolylsulfenamide (CBS), 3-diphenylguanidine (DPG) as cross-linking reagents. The rubber was cut as 200 nm-thick by ultramicrotome and was placed on a TEM grid. As reference samples, CBS, DPG and 2-mercaptobenzothiazole (MBT) were dispersed in acetone and were drop-casted onto TEM grids with support membrane. X-ray absorption images of unvulcanized and vulcanized rubbers taken at 400 eV are shown in Fig. 1. In these images, dark spots show higher absorption than matrix and are considered as distribution of cross-linking reagents. By comparing Figs. 1(a) and 1(b), dark spots decrease in size and become more dispersive through a vulcanization process. Normalized N *K*-edge NEXAFS spectra of reference samples of CBS (blue), DPG (green), MBT (red) and the dark spot (black; shown by an arrow in Fig. 1(b)) are shown in Fig. 2. Although the signal of the dark spot is quite low, the dark spot seems to be consisted of mixture of CBS, DPG and MBT. Especially, the sharp peak of MBT at 400.8 eV contributes to that of the dark spot. MBT was produced by vulcanization process and contributed to the distribution of cross-linking reagent.

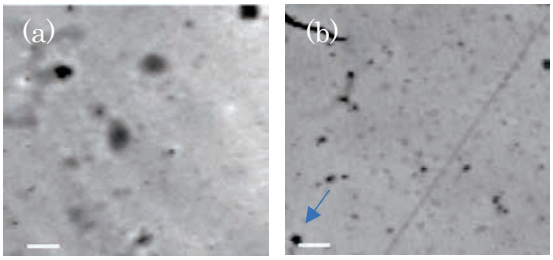

Fig. 1. X-ray absorption image of (a) unvulcanized and (b) vulcanized rubbers taken at 400 eV. Scale bars are 5 μm.

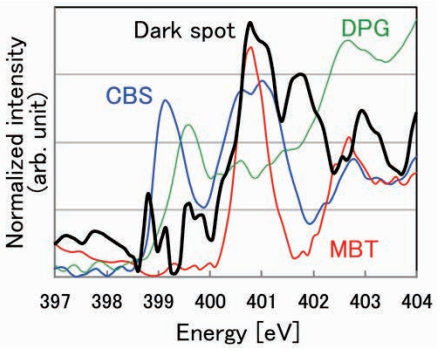

Fig. 2. N *K*-edge NEXAFS spectra of CBS (blue), DPG (green), MBT (red) and a dark spot (shown in Fig. 1 by an arrow). The spectra are normalized by max and minimum.

[1] T. Ohigashi, F. Kaneko, H. Yuzawa and H. Kishimoto, *UVSOR Activity Report 2021*, **49** (2022) 73.
[2] T. Ohigashi, *et al*., J. Electron Spectrosc. Relat. Phenom. **266** (2023) 147356.

BL4U

Scanning Transmission X-ray Microscopy of Hydrogen Evolution Electrocatalysts on Graphene Oxide Membranes

C. O. M. Mariano[a], J. S. D. Rodriguez[a,b], R. H. Clemente[a], T. Ohigashi[c,d], H. Yuzawa[c], W. H. Hsu[e], J. Shiue[f] and C. H. Chuang[a,*]

[a]*Department of Physics, Tamkang University, Tamsui, New Taipei City 251301, Taiwan*
[b]*Institute of Chemistry, Leiden University, Leiden, 2300 RA, The Netherlands*
[c]*Institute for Molecular Science, Okazaki 444-8585, Japan*
[d]*Photon Factory, Institute of Materials Structure Sciences, High Energy Accelerator Research Organization, Tsukuba 305-0801, Japan*
[e]*Institute of Physics, Academia Sinica, Nankang, Taipei 11529, Taiwan*
[f]*Institute of Atomic and Molecular Sciences, Academia Sinica, Daan, Taipei 106319, Taiwan*

The oxygen functional groups present in GO have effects on the HER activity of cobalt catalyst (Co_xO_y) and should be studied for its specific role thoroughly. GO has several oxygen functional groups, i.e., carboxyl (-COOH), carbonyl (C=O), hydroxyl (-OH), and epoxide groups (C-O-C). These functional groups are important because they can interact with the cobalt ions, which increases the catalytic activity for the HER. The oxygen functional groups of GO can be identified using such as fourier-transform infrared spectroscopy, raman spectroscopy, and X-ray photoelectron spectroscopy, but to acquire additional information about the spatial distribution of these functional groups, scanning transmission X-ray microscopy (STXM) must be used [1].

This study aims to understand the relationship between the oxidation state of Co_xO_y supported on GO membranes (called as Co/GO), for their catalytic activities. Fig. 1(a) shows the surface morphology of the dropcast GO membranes measured using the tapping mode of AFM. The vertical difference along the line profile (red arrow) was noted as 46 nm because a random flake stacking of the GO on the Au mesh behaves like a rough surface after drying. Fig. 1(b) exhibits a SEM image for the Co_xO_y grown on GO membranes, and Fig. 1(c) shows a high magnification image of Co/GO to display the 3D wrinkle flower structure of electrodeposited (ED) Co.

To identify the nanoscale distribution of these heterogeneous materials, STXM was measured in the energy regions of C *K*-edge, O *K*-edge, and Co *L*-edge XANES. The area-selected spectra are marked as “1”, “2”, and “3” owing to the prominent contrast in the OD image at C/O *K*-edges and Co *L*-edge, as for the total absorbance amount of Co/GO membranes. From the C *K*-edge XANES of Fig.1(d), the oxygen functional groups (C-O-C, C=O of COOH, and C=O) in the GO membranes were assigned based on our previous result [1]. The feature at 284.9 eV was assigned to the formation of doubly coordinated carbon, because of the ring opening and modifying π^* bond [2]. The intensive feature at 288.4 eV is known as HO-C=O (π^*)/defect state and its low-energy shoulder nearby at 287.4 eV is assigned to C-O-C (π^*) state; furthermore, the most intensive feature and its shoulder are identified as O-C(O)-O/C=O (π^*) of the GO edge at 290.2 eV and HO-C=O (σ^*) state at 289.5 eV [1,2,3]. C-OH (π^*) at 286.5 eV appears in the raw GO membranes [1] but is absent in Co/GO membranes.

Fig. 1(e) exhibits the area-selected O *K*-edge XANES spectra of Co/GO and GO. Compared the spectrum Co/GO with that of GO, the signal of O 2*p*-Co 3*d* (π^*) and Co-4*s* (σ^*) newly centered at PEs of 531.5 eV and 539.5 eV [3,4]. The surface oxidation (i.e., C=O and C-O-C) of the GO membranes also emerges among the feature centered at 531.5 eV [1]. Furthermore, it is critical to see one shoulder at the 534.4 eV, mainly considered a water signal[5]. Fig. 1(f) shows Co *L*-edge XANES spectra, which are composed of spectral components of Co^0, Co^{2+}, and Co^{3+} states. The octahedral (Oct.) symmetrical Co^{2+} state composes of two features at 775.0 and 776.2 eV. The metal species of cobalt has one primary absorption at 776.2 eV because its energy levels are continuous. The Oct. symmetrical Co^{3+} state offers two additional features at 777.3 and 779.6 eV, with a higher energy range than the other cobalt species[3]. The rising shoulder shows the gains of metal cobalt and Oct. Co^{3+} states due to the chemical reduction and growth along the continuous electrodeposition process, consistent with the result on the G membranes (Co/G) in Fig. 1(f) [3].

The Co/GO membranes became a great variety in the oxidation state and lattice structure at the interface, compared to the raw GO surface. The mapping and spectroscopic information at different positions helps us to understand the chances of ED Co_xO_y growth on the confirmed GO membranes.

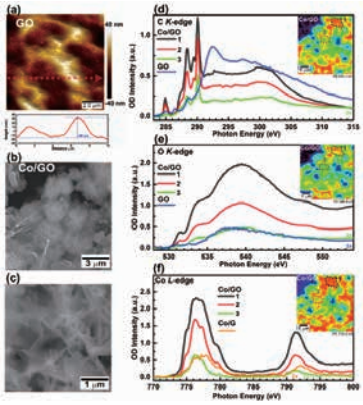

Fig. 1. (a) AFM image of GO membranes and certain curve of its height line profile along the red dotted arrow. (b)(c) SEM image of electrodeposited Co-GO membranes. (d)-(f) XANES spectra of selected areas at C *K*-edge, O *K*-edge, and Co *K*-edge.

[1] J.S.D. Rodriguez *et al.*, Carbon N Y. **185** (2021) 410.
[2] J.J. Vélez *et al.*, Electrochem. Soc. **160** (2013) C445.
[3] J.-J.V. Vélez *et al*,. Chin. J. Phys. **76** (2022) 135.
[4] J. Wang *et al.*, Energy Environ. Sci. **6** (2013) 926.
[5] J.W. Smith *et al.*, Chem. Rev. **117** (2017) 13909.

BL4B

Examination of Methods for Inner Structures of Magnetic Thin Films at UVSOR BL4B by Reflection XMCD Measurement Setup

K. Yamamoto, H. Iwayama, O. Ishiyama and T. Yokoyama
Institute for Molecular Science, Okazaki 444-8585, Japan

Complex depth-structured magnetic thin films/ multilayers exhibit a wide range of magnetic phenomena due to interlayer interactions[1]. In addition, multilayer structures are used to achieve useful properties in recording media, an application area of great importance for magnetic materials. It has been possible to elucidate the evolution mechanism of the magnetic structure of thin films by directly observing the magnetic distribution in the depth direction of these magnetic multilayers.

We have installed an experimental setup for the reflection X-ray magnetic circular dichroism (XMCD) method [2] in the soft X-ray region at BL4B, and experiments have been performed on test samples. The sample and detector can be rotated independently to obtain the reflectivity. The magnetic field was about 0.35T and the measurements were performed at room temperature. The magnetic field was applied by two pairs of opposing Nd magnets. The magnets can be rotated and the relative position between the magnetic field and the sample was kept constant. The setup is shown schematically in Fig. 1. We used a photodiode (AXUV100G, Optodiode inc.) for our measurements last year. In order to measure the lower signals in the higher angle regions and to eliminate the fluorescence of oxygen from the substrates, we introduced a silicon drift detector (FASTSDD, Amptek). The detector temperature was controlled by water cooling and the noise level was kept constant at lower levels and the detector and samples can be rotated arbitrary in the vacuum chamber shown in Fig. 2.

We used off-axis components of X-rays from the bending magnet to obtain circularly polarised light. The X-rays are elliptically polarised. The intensity of the XMCD was measured by changing the direction of the magnetic field.

When measurements were performed on a reference sample, a vibrational structure was observed due to interference between the cap layer and the underlying layer. By changing the direction of the magnetic field, differences corresponding to XMCD were observed. The same measurements were also made near the absorption edge and spectroscopic information was extracted. However, structural information is not well obtained compared to hard x-rays. Using an X-ray tube light source, we also performed hard x-ray reflectometry. Both soft and hard X-ray results could be reproduced by simulations based on a full-matrix algorithm, taking into account the magneto-optical effects of elliptically polarized X-rays. Although there have been previous studies using XMCD of reflectance, few have extended this method to obtain spectroscopic information. In order to analyze depth-resolved magnetization information, spectroscopic measurements were performed to obtain the photon energy dependence and the reflection angle dependence.

Combining this study with a light source that can arbitrarily modulate polarization would provide a method to reveal more detailed properties.

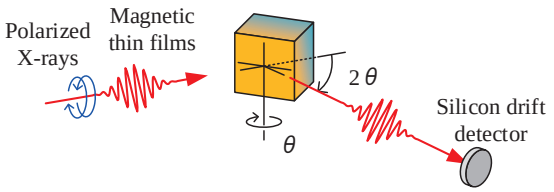

Fig. 1. The illustration for the XMCD reflectivity measurements.

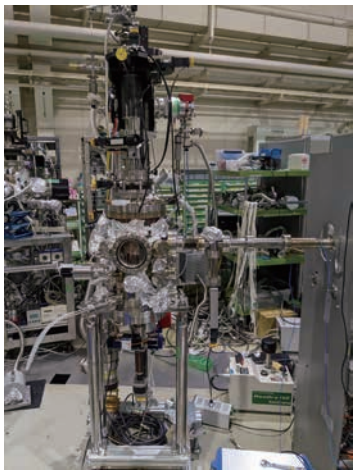

Fig. 2. The vacuum chamber for the maeasurements in UVSOR BL4B.

[1] F. Hellman *et al.*, Rev. Mod. Phys. **89** (2017) 025006.
[2] S. Macke and E. Goering, J. Phys. Condens. Matter. **26** (2014) 363201.

BL4B

$L_{2,3}$-edge X-ray Absorption Spectra of Transition Metal in Wurtzite-AlN

S. Imada

Faculty of Electrical Engineering and Electronics, Kyoto Institute of Technology, Kyoto 606-8585, Japan

3d-TM doped AlN ($Al_{1-x}TM_xN$) is promising for light-emitting, spintronic, and photoelectric conversion materials [1,2]. For these applications, it is indispensable to reveal the electric structure, including ligand field and charge transfer multiplets. For this purpose, TM $L_{2,3}$-edge X-ray absorption structure (XAS) and resonant X-ray emission scattering (RIXS) spectroscopies are powerful tools. So far, however, a comprehensive and systematic study of these important systems still needs to be included.

We synthesised and investigated the band structures of $Al_{1-x}TM_xN$ using Al and N K-edge XAS [2-4]. This study investigated TM $L_{2,3}$-edge XAS structures of $Al_{1-x}TM_xN$ films with various TM concentrations ($0.02<x<0.08$), focusing on Ti, V and Mn for the first time. For example, with low concentrations $x<0.05$, the average distance between TMs is larger than 7.5Å; we expect to observe a well-localised electronic structure. Looking ahead, we can even prepare films including other TMs with concentrations well above 0.1 (<6Å) to reveal interactions between TMs, which are necessary to understand for spintronic and photoelectric conversion use.

Here we show an example of the TM concentration dependence of the XAS structure for $Al_{1-x}Ti_xN$. Our previous study [2] revealed that the $Al_{1-x}Ti_xN$ films with $x \geqq 0.083$ showed photoconductivity under blue-green light irradiation, while the film with $x<0.083$ did not. The Ti $L_{2,3}$-edge XAS spectra of $Al_{1-x}Ti_xN$ films showed structural change at x=0.083 (Fig.1). Our previous study on Ti K-edge extended X-ray absorption fine structure (EXAFS) did not show any evidence of local crystallographic structure change at the concentration. Thus, we tentatively conclude that the observed change in $L_{2,3}$-edge XAS implies delocalisation of Ti 3d electrons starts at around x=0.083. To reveal the origins of the spectral change in detail, we will conduct L-edge RIXS measurements and partial RIXS yield (PRIXSY) analyses, which will give us new insights into XAS structure interpretation.

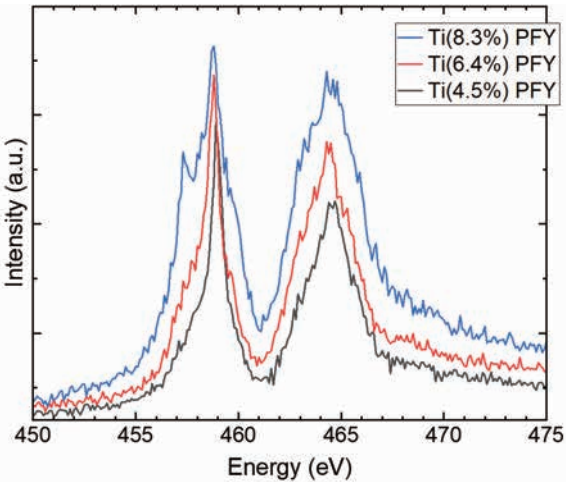

Fig. 1. Ti $L_{2,3}$-edge X-ray absorption spectra of $Al_{1-x}Ti_xN$ films (x= 0.083, 0.064, and 0.045) These spectra were measured in partial fluorescence yield (PFY) mode.

[1] S. S. Khludkov *et al.*, Russian Physics Journal **63** (2020) 2013.
[2] N. Tatemizo *et al.*, J. Mater. Chem. A **5** (2017) 20824.
[3] N. Tatemizo *et al.*, Sci. Rep. **10** (2020) 1819.
[4] S. Imada *et al.*, Matr. Adv. **2** (2021) 4075.

BL4B

C K-edge XAFS Measurement of Carbon Containing Porous Silica

S. Dohshi
Osaka Research Institute of Industrial Science and Technology
2-7-1, Ayumino, Izumi, Osaka 594-1157, Japan

Porous silica with only micropores of less than 1 nm in diameter has been successfully synthesized by using collagen fibers or denatured collagen as a template [1]. As a result of a detailed study of the process of removing collagen as a template by calcination, we found that the porous silica with a small amount of carbon (hereafter denoted as carbon containing porous silica) showed white luminescence under UV light irradiation [2]. The emission spectrum of the prepared carbon containing porous silica under UV excitation shows a continuous spectrum over the visible light region, and this carbon containing porous silica is expected to be used as a white light source material with high color rendering property. The author investigated the mechanism of white luminescence of carbon-containing porous silica. Since porous silica without carbon does not show white light luminescence property under UV light irradiation, it is clear that carbon in porous silica contributes to luminescence property. However, the local structure of carbon in porous silica has not yet been elucidated because the carbon content is very low, about 0.1%. Therefore, in this study, we attempted to elucidate the local structure of carbon in porous silica by C K-edge XAFS measurement using BL4B of UVSOR III. We optimized the sample preparation method and measurement conditions.

Fig. 1 shows the experimental setup at BL4B and the sample holder for C K-edge XAFS measurement. The powder sample was fitted onto carbon tape or indium foil. The measurement was performed by fluorescence mode (using SDD detector).

When the sample was fixed on the carbon tape, the spectra derived from the carbon tape were observed, and almost no spectra derived from the sample were observed. On the other hand, when the sample was fixed on indium foil, the spectra derived sample was obtained. It was also found that the X-ray irradiation angle to the sample had a significant effect on the intensity of the spectra.

In the next fiscal year, we will measure the C K-edge XAFS measurement using pelletized sample under the optimized conditions.

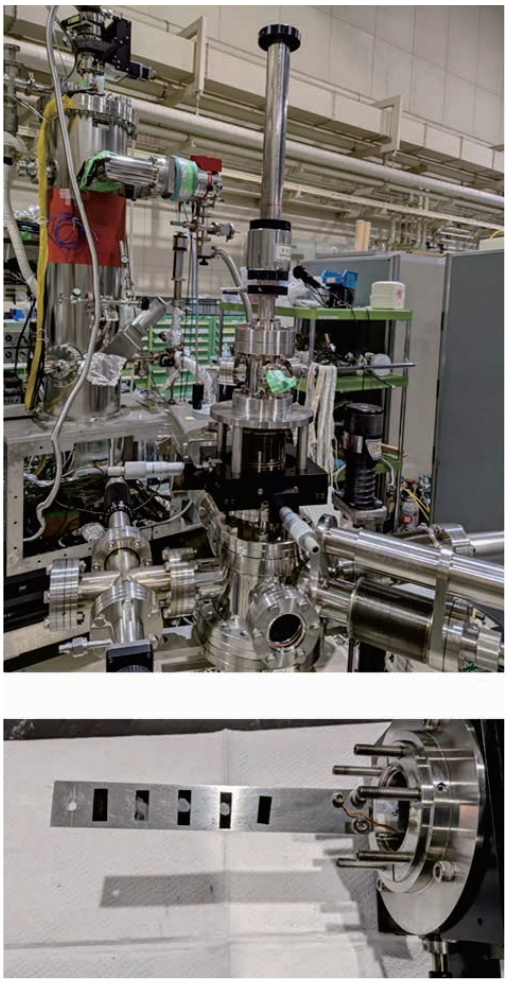

Fig. 1. The experimental setup at BL4B and the sample holder for C K-edge XAFS mesurement.

[1] S. Dohshi, J. Soc. Leather Technol. Chem, **95** (2011) 200.
[2] S. Dohshi *et al*., J. Soc. Mater. Sci., Jpn., **68** (2019) 549.

BL5U

Evolution of the Electronic States by Electron Doping in a Kagome Superconductor KV_3Sb_5

T. Kato[1], K. Nakayama[1], Y. Li[2,3,4], Z. Wang[2,3,4], S. Souma[5,6], K. Tanaka[7,8], T. Takahashi[1], Y. Yao[2,3] and T. Sato[1,5,6,9]

[1]*Department of Physics, Graduate School of Science, Tohoku University, Sendai 980-8578, Japan*
[2]*Centre for Quantum Physics, Key Laboratory of Advanced Optoelectronic Quantum Architecture and Measurement (MOE), School of Physics, Beijing Institute of Technology, Beijing 100081, P. R. China*
[3]*Beijing Key Lab of Nanophotonics and Ultrafine Optoelectronic Systems, Beijing Institute of Technology, Beijing 100081, P. R. China*
[4]*Material Science Center, Yangtze Delta Region Academy of Beijing Institute of Technology, Jiaxing, 314011, P. R. China*
[5]*Advanced Institute for Materials Research (WPI-AIMR), Tohoku University, Sendai 980-8577, Japan*
[6]*Center for Science and Innovation in Spintronics (CSIS), Tohoku University, Sendai 980-8577, Japan*
[7]*UVSOR Synchrotron Facility, Institute for Molecular Science, Okazaki 444-8585, Japan*
[8]*School of Physical Sciences, The Graduate University for Advanced Studies (SOKENDAI), Okazaki 444-8585, Japan*
[9]*International Center for Synchrotron Radiation Innovation Smart (SRIS), Tohoku University, Sendai 980-8577, Japan*

Recent discovery of a new kagome-lattice material AV_3Sb_5 (A = K, Rb, and Cs) is attracting great attention. While most of the kagome-lattice materials studied so far have been magnetic, AV_3Sb_5 is unique in that it is paramagnetic and shows superconductivity with T_c of 0.93-2.5 K. AV_3Sb_5 also undergoes a charge-density wave (CDW) transition below T_{CDW} = 78-103 K, accompanied by the unit-cell doubling with the 2×2×2 periodicity. This CDW state shows an intriguing interplay with the superconductivity and hosts exotic properties such as strong anomalous Hall effect, possible time-reversal symmetry breaking, and nematicity. From the electronic structure point of view, AV_3Sb_5 is a multiband/multi-orbital superconductor characterized by the formation of multiple Fermi surfaces originating from Dirac-cone, saddle-point, and free-electron-like bands. Given the multiband character, it is essential to understand which bands/orbitals are responsible for the CDW and superconductivity. A useful means to clarify this point is to control the energy position of bands relative to the Fermi level (E_F) by carrier doping [1] because the CDW and superconductivity would be sensitive to the band filling.

In this study, we have performed an angle-resolved photoemission spectroscopy (ARPES) study on K-dosed KV_3Sb_5. We have successfully controlled electron doping level by K dosing and determined the doping-induced evolution of the band structure.

High-quality single crystals of KV_3Sb_5 were grown by the self-flux method. K dosing was carried out by using K dispenser (SAES Getters) in an ultrahigh vacuum. High-resolution ARPES measurements were performed by using a MBS-A1 spectrometer at BL5U with linearly-polarized energy-tunable photons.

A comparison of Fermi surfaces in pristine [2] and K-dosed KV_3Sb_5 [Figs. 1(a) and 1(b), respectively] shows that a circular-shaped electron pocket at the Γ point expands with the K dosing, indicative of the electron doping. We have estimated the amount of energy shift for each band and found band/orbital-dependent electron doping effect. In addition, we determined the evolution of CDW gap size with electron doping. Our results suggest an important role of the saddle-point band for the occurrence of CDW.

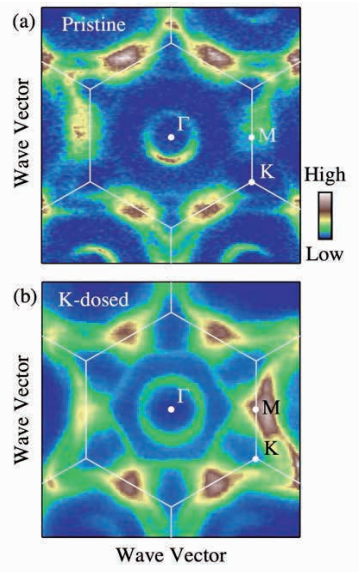

Fig. 1. (a), (b) ARPES intensity plots at E_F in freshly cleaved and K-dosed KV_3Sb_5, respectively

[1] K. Nakayama *et al.*, Phys. Rev. X **12** (2022) 011001.
[2] T. Kato *et al.*, Commun. Mater. **3** (2022) 30.

BL5U

Evolution of Electronic Correlations and Excitonic Properties Near semiconductor-excitonic Insulator Transition

K. Fukutani[1, 2], K. Kiyosawa[3], C.I. Kwon[4,5], J.S. Kim[4,5], K. Tanaka[1,2] and S. Kera[1,2,3]

[1]*Institute for Molecular Science, Okazaki 444-8585, Japan*

[2]*The Graduate University for Advanced Studies (SOKENDAI), Okazaki 444-8585, Japan*

[3]*Graduate School of Science and Engineering, Chiba University, Chiba 263-8522, Japan*

[4]*Center for Artificial Low-Dimensional Electronic Systems, Institute for Basic Science, Pohang, Korea*

[5]*Pohang University of Science and Technology, Pohang, Korea*

In semiconductors, external stimuli, such as light irradiations are known to create bound pair of an electron and a hole. This quasi-particle is known as excitons, and are known to play principal roles in various quantum devices, including solar cells, light emitting diode (LED), and excitonic lasers etc. The efficient creation of excitons and the manipulations of their properties are among the central interest in the current semiconductor industry.

Recently, what is called an *excitonic insulator* has been experimentally identified. This new class of materials is either a narrow-gap semiconductor or a shallow-overlap semimetal in their normal phase and, at sufficiently low temperature, the electrons and holes are spontaneously paired into excitons via quantum condensation process.

Ta_2NiSe_5 is one of the most extensively studied excitonic insulators [1], along with 1*T*-$TiSe_2$. What differentiates Ta_2NiSe_5 from 1*T*-$TiSe_2$ is the fact that the former exhibits a direct band gap and does not accompany the change in the structural periodicities (charge density wave transition). Thus, from the point of view of excitonic instability, Ta_2NiSe_5 is ideal platform to study the nature of excitonic insulator and the transition to/from the normal phase.

The recent extensive researches have revealed that Ta_2NiSe_5 is classified into Bose-Einstein condensate (BEC)-type excitonic insulator, while it is near the crossover regime between BEC and BCS transitions.

Theoretically, in the BEC-type excitonic insulator, the excitons are created *above* the transition temperature (T_c) and as they cool down below T_c, those "preformed excitons" undergo the condensation and acquire the macroscopic coherence [2]. The temperature (and band gap) regime where such steady-state excitons exist without forming a condensate is called "preformed exciton phase" and its existence has been recently verified [3].

Such phase of steady-state excitons represents the inverted ground state from the normal semiconductors (i.e., the excitons are formed in the *ground state*, while the external stimuli are required to dissociate them into free carriers) and provides a particularly unique playground for future electronics applications.

The purpose of this research project is to explore the excitonic insulator phase diagram both in terms of temperature and the bandgap to evaluate the properties of the steady-state excitons, including its binding energy, Bohr radius and their relative density (compared to the free carriers), in order to understand the formation process of this new ground state.

With these goals, we have performed high-resolution angle-resolved photoemission spectroscopy (ARPES) at BL5U for the chalcogen-substituted compounds $Ta_2Ni(Se_{1-x}S_x)_5$ with particular focus at the composition $x \sim 0.6$, where the material is believed to be very close to the transition between a BEC-type excitonic insulator and a normal semiconductor. Figure 1 shows the temperature-dependent ARPES spectra for this composition. It can be seen that at $T \sim 120$ K, the material exhibits a flat-top valence band, characteristic of excitonic insulator phase. As the temperature rises, at $T \sim 200$ K, the clear signature of exciton appears near the valence band maximum and at $T \sim 350$ K, the valence band maximum is no longer flat, reminiscent of the normal semiconductor Ta_2NiS_5, and the weakened exciton signal moves towards the Fermi level with the valence band. These observations possibly indicates that as the temperature increases, the electronic correlations, which are keeping the excitons bound, are weakening at the same time as the exciton binding energy decreases. The experimental results obtained here are expected to give new insights into the formation path of excitons.

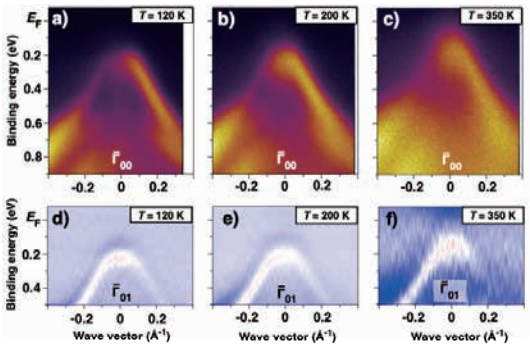

Fig. 1. Temperature-dependent ARPES data from $Ta_2Ni(Se_{1-x}S_x)_5$ at $x \sim 0.6$ measured at (a) $T \sim 120$ K, (b) 200 K and (c) 350 K. The second derivative plots from Γ_{01} are shown on the bottom panel (d-f).

[1] Y. Wakisaka *et al.*, Phys. Rev. Lett. **102** (2009) 026402.
[2] Y.F. Lu *et al.*, Nat. Commun. **8** (2017) 14408.
[3] F.X. Bronold *et al.*, Phys. Rev. B **74** (2006) 165107.
[4] K. Fukutani *et al.*, Nat. Phys. **17** (2021) 1024.

BL5U

Polarization-dependent Angle-resolved Photoemission Study of MAX Phase Compound Zr_3SnC_2

M. Mita[1], D. Pinek[2], M. Nakatake[3], K. Tanaka[4,5], T. Ouisse[2] and T. Ito[1,6]
[1]*Graduate School of Engineering, Nagoya University, Nagoya 464-8603, Japan*
[2]*Grenoble Alpes, CNRS, Grenoble INP, LMGP, F-38000 Grenoble, France*
[3]*Aichi Synchrotron Radiation Center, Seto, 489-0965, Japan*
[4]*UVSOR Facility, Institute for Molecular Science, Okazaki 444-8585, Japan*
[5]*The Graduate University for Advanced Studies, Okazaki 444-8585, Japan*
[6]*Synchrotron radiation Research center, Nagoya University, Nagoya 464-8603, Japan*

MAX phase compounds, i.e., $M_{n+1}AX_n$ where M is a transition metal, A belongs to groups 13-16 and X is the C or N element, have recently been attracted much attention due to their possible application for new class of two-dimensional systems called MXenes by removing A atoms [1]. On the other hand, the bulk electronic structure of MAX phase has been studied mostly by calculations, mainly because of lack of well-established single crystalline samples. In this study, we have performed angle-resolved photoemission spectroscopy (ARPES) on MAX phase compound Zr_3SnC_2, in which relatively higher two-dimensionality than 211 phase due to the thicker MX layer as well as the strong spin-orbit coupling effect due to the 4d transition metal Zr were expected.

ARPES measurements were performed at the UVSOR-III BL5U. Data were acquired at T = 30 K with hν = 76 eV which enables us to trace around the ΓKM plane with inner potential of V_0=17.7 eV estimated from the photon energy dependent measurement (not shown). With using linear horizontally (LH), vertically (LV) and circularly right (CR), left (CL) polarized photons, we have obtained the orbital and orbital-angular-momentum (OAM) dependent ARPES images. It should be noted that each ARPES images were obtained without changing the photon incident angle relative to the sample surface by utilizing two-dimensional mapping lens mode of MBS A-1 analyzer.

Figure 1 shows the obtained Fermi surface (FS) image on the ΓKM plane. The band structure along the ΓM line is shown in Fig. 2 (a) together with the DFT calculation of Sn-terminated surface. Six-folded symmetry of hole-pockets α and β has clearly been observed in consistent with the DFT calculation. In addition, three-fold symmetry around the K point of the small triangular-shape FS γ formed by so-called saddle-like surface state (SS) at the M point also has been elucidated in Fig.1. With respect to this SS, even orbital symmetry has been recognized with almost the same circular dichroism (Fig. 2(b) and (c)). On the other hand, opposite OAM sign without changing orbital symmetry with respect to the MK line has been observed at the high-binding energy region. The results might suggest the change of chirality of OAM at the high-energy bound states at the Sn-terminated surface of Zr_3SnC_2. To elucidate the relation between the observed anomalies and the spin-orbit coupling effect, further studies are intended.

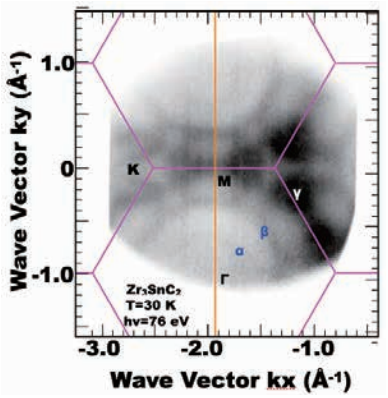

Fig. 1. (a) Fermi surface (FS) image on ΓKM plane of Zr_3SnC_2.

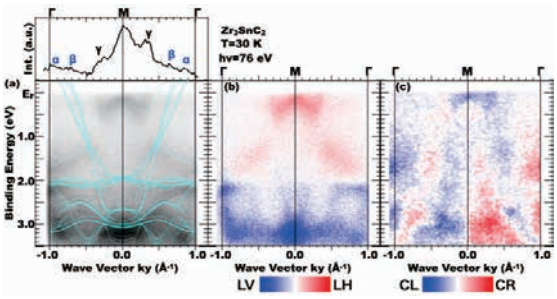

Fig. 2. (a) Band structure along the ΓM line of Zr_3SnC_2 obtained by LH polarized photons. Solid lines are DFT calculation for Sn-terminated surface. (b,c) orbital (b) and OAM (c) dependent ARPES image of Zr_3SnC_2 along the ΓM line, which is obtained by subtracting the ARPES results of linearly (LH−LV) and circularly (CR−CL) polarized photons, respectively.

[1] M. Basoum, *MAX phases* (Wiley, Weinheim 2013).

BL5U, 7U

Electronic Structure of a Layered Magnetic Semiconductor $CeTe_{1.83}Sb_{0.17}$

T. Nakamura[1,2], H. Murakawa[2], Y. Chen[2], H. Sugihara[2], K. Tanaka[3], N. Hanasaki[2] and S. Kimura[1,2,3]

[1]*Graduate School of Frontier Biosciences, Osaka University, Suita 565-0871, Japan*
[2]*Department of Physics, Graduate School of Science, Osaka University, Toyonaka 560-0043, Japan*
[3]*Institute for Molecular Science, Okazaki 444-8585, Japan*

The metal-insulator transition through charge density wave (CDW) formation has been a central topic of solid-state physics. While many materials have been reported to exhibit CDW, $CeTe_2$, a family of rare-earth dichalcogenide, has attracted considerable interest due to its high transition temperature that reaches 1000 K [1,2] as well as magnetic ordering below 4 K [3]. Recently, $CeTe_{1.83}Sb_{0.17}$, which shows a huge anisotropic magnetoresistance ratio as high as 7500 thanks to the extremely low carrier density, has been synthesized by a chemical vapor transport technique [4]. Due to the partial substitution of Te with Sb, an extra charge carrier removes by hole doping. However, the detail of the electronic band structure of this sample has not been observed yet. In this study, we have measured the angle-resolved photoelectron spectroscopy (ARPES) of the $CeTe_{1.83}Sb_{0.17}$ to investigate the electronic structure.

The single-crystalline $CeTe_{1.83}Sb_{0.17}$ was cleaved under ultra-high vacuum conditions. Due to the difficulty of cleavage, the ARPES measurable domain size was less than 100×100 μm^2. However, the micro-focused beam from UVSOR-III BL5U made it possible to observe the electronic structure in a piece of domains.

Figure 1 shows the resonant angle-integrated photoelectron spectra of $CeTe_{1.83}Sb_{0.17}$, taken with the energy of 122 eV, corresponding to the resonant energy of the Ce 4*d*-4*f* absorption. In contrast to the non-resonant condition ($h\nu$ = 110 eV), the sharp peak at a binding energy of 1.7 eV originates from the Ce $4f^0$ final states after photoexcitation was observed in the resonant condition, indicating that the Ce 4*f* states are fully localized.

Figure 2 shows the ARPES intensity plot along Γ-M at 15 K. Several hole bands near the Γ point are observed. Among them, the apex of band H1, which is at the outermost part of the measurement range, seems to be in an unoccupied state, indicating that it exhibits metallic properties even though extremely low carrier densities are confirmed in the transport measurements. Further experimental studies such as polarization dependence and bulk sensitive measurement using higher energy photons would help to elucidate the orbital character of bands in the electronic structure of $CeTe_{1.83}Sb_{0.17}$.

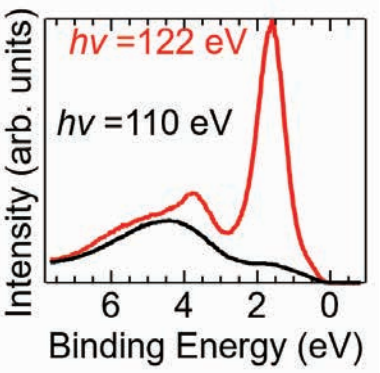

Fig. 1. Resonant angle-integrated photoelectron spectra of $CeTe_{1.83}Sb_{0.17}$ at 15 K. The excitation energies of 110 and 122 eV correspond to the off- and on-resonance conditions at the Ce 4*d*-4*f* absorption edge.

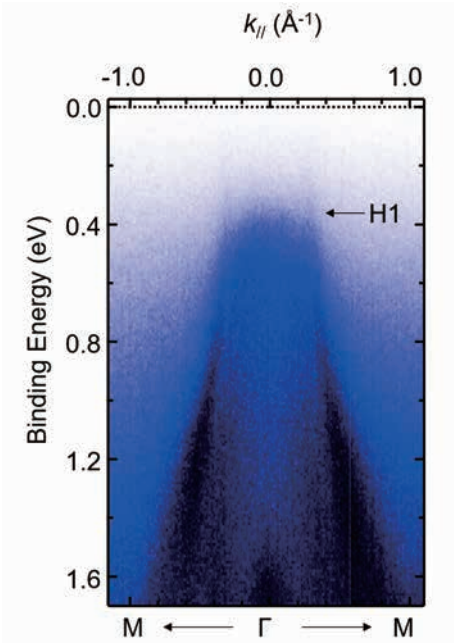

Fig. 2. ARPES intensity plot of $CeTe_{1.83}Sb_{0.17}$ along Γ-M taken with 103 eV at 15 K.

[1] J. G. Park *et al.*, Physica B **241-243** (1998) 684.
[2] M. H. Jung *et al.*, J. Phys. Soc. Jpn. **69** (2000) 937.
[3] M. H. Jung *et al.*, Phys. Rev. B **67** (2003) 212504.
[4] H. Murakawa *et al.*, Phys. Rev. Mater. **6** (2022) 054604.

BL5U

Synchrotron ARPES Study of Nodal Dirac Semimetal Candidate LaTeBi

R. Saitou[1], N. Kataoka[1], H. Kageyama[1], R. Kondo[1] and T. Yokoya[1,2]
[1]*Graduate School of Natural Science and Technology, Okayama University, Okayama 700-8530, Japan*
[2]*Research Institute for Interdisciplinary Science, Okayama University, Okayama 700-8530, Japan*

$LnTe_{1+x}Sb_{1-x}$ (Ln: lanthanides) is a layered material consisting of alternative stack of a layer of LnTe and a layer of a single Sb square lattice. It is theoretically predicted as a nodal line semimetal [1]. In addition, by selecting a magnetic element as Ln, it is possible to break the time-reversal symmetry. Therefore, it is a material that has the potential to access novel topological phases [2-5]. Our research group are making an effort to control the physical properties of related materials by introducing magnetic elements, substituting Sb with Bi, and changing carrier concentration [6] for the purpose of observing the exotic transport properties peculiar to Dirac electrons. In the present study, we have performed synchrotron angle-resolved photoemission spectroscopy (ARPES) to clarifying the electronic structure of the non-magnetic phase and check the relative energy relationship between the Fermi energy (E_F) and Dirac nodes in a related material, $LaTe_{1+x}Bi_{1-x}$, which possesses single square lattices composed of Bi atoms, having a stronger spin-orbit interaction than Sb.

$LaTe_{1+x}Bi_{1-x}$ single crystal samples (x = 0.025) were prepared by a self-flux method. ARPES measurements were performed at BL5U of UVSOR III. Linear polarized light of 32-124 eV energies were used. The energy resolution was set to ~ 40 meV. All samples were cleaved in situ on the (001) plane in an ultrahigh 4vacuum of less than 5.0 x 10^{-9} Pa and were measured at 20 K.

Figure 1 shows the valence band dispersion of $LaTe_{1+x}Bi_{1-x}$ along the Γ-X direction in the Brillouin zone (BZ), measured with the photon energy of 94 eV. White regions, which are the higher-intensity regions, correspond to band dispersions. The band dispersions are symmetric with respect to the high symmetry points: Γ and X of the bulk BZ of $LaTe_{1+x}Bi_{1-x}$. This indicates that the band dispersions reflect intrinsic electronic structure of the sample. Importantly, one can observe weak structures near E_F on both sides of the X points, where Dirac nodal lines are expected to be located theoretically. To look at the electronic structures more in detail, an energy and momentum enlarged intensity map is shown in Fig. 2. We now clearly observe two electron-pockets-like structures. These band dispersions are consistent with the calculated band dispersions. However, at the X point, the intensity at E_F is very small, indicating that the starting point of the theoretically expected Dirac nodal line at the X point is not located below E_F for the measured sample. The energy position of the Dirac nodal line at the X point with respect to E_F is found to be calculation dependent. However, an implication from this study is that the electron concentration is not enough. To achieve the interesting physical properties originating from the topological electronic structure in the sample, further electron doping is necessary.

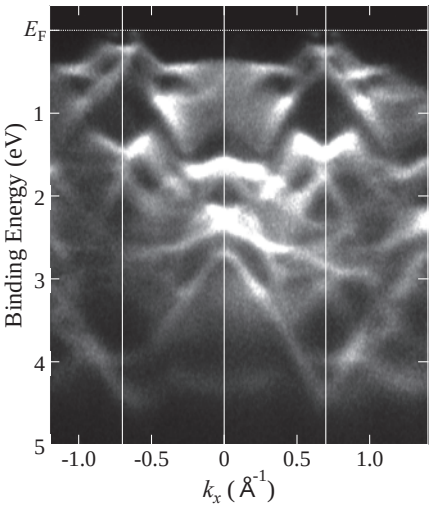

Fig. 1. ARPES intensity map of $LaTe_{1+x}Bi_{1-x}$ measured with 94 eV photons and at 20 K.

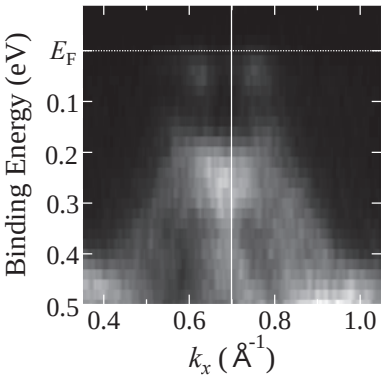

Fig. 2. Enlargement of Fig.1 for the region near E_F and the X point.

[1] A. Weiland *et al*., APL Mater. **7** (2019) 101113.
[2] Y. Wang *et al*., Phys. Rev. B **103** (2021) 125131.
[3] S. Yue *et al*., Phys. Rev. B **102** (2020) 155109.
[4] P. Gebauer *et al*., Chem. Mater. **33** (2021) 2420.
[5] L. M. Schoop *et al*., Sci. Adv. **4** (2018) eaar2317.
[6] R. Kondo, in preparation.

BL5U,7U

Re-examination of the Phase Diagram of the high-T_c Cuprate Superconductor $Bi_2Sr_2CaCu_2O_{8+\delta}$ Studied by ARPES

Y. Tsubota[1], Y. Miyai[2], S. Nakagawa[5], S. Ishida[4], S. Kumar[2], K. Tanaka[3], H. Eisaki[4], T. Kashiwagi[5], M. Arita[2], K. Shimada[1,2] and S. Ideta[1,2]

[1]*Graduate School of Advanced Science and Engineering, Hiroshima Univ., Japan*
[2]*Hiroshima Synchrotron Radiation Center (HiSOR), Hiroshima Univ., Japan*
[3]*UVSOR-III Synchrotron, Institute for Molecular Science, Japan*
[4]*National Institute of Advanced Industrial Science and Technology (AIST), Japan*
[5]*Graduate School of Science and Technology, Tsukuba Univ., Japan*

It has been known that the cuprate superconductors show a high superconducting (SC) transition temperature (T_c) and exotic physical properties. However, the SC mechanism has been unclear yet. In order to understand the mechanism of high-T_c cuprates, $Bi_2Sr_2CaCu_2O_{8+\delta}$ (Bi2212) is one of the promising candidates to study the electronic structure and reveal the physical properties. Bi2212 has two CuO_2 planes in the unit cell and shows the high T_c around 95 K at the optimally doped sample. Superconductivity occurs upon hole doping into the CuO_2 plane and the amount of hole doping can control T_c, and therefore, carrier doping (hole/electron concentration) plays an important key parameter in cuprates [1, 2]. The electronic phase diagram of hole-doped high-T_c cuprate superconductors plotted as a function of temperature and carrier concentration has been reported as an empirical and universal phase diagram which is a dome-like shape centered at ~0.16 of hole concentration [1]. However, previous ARPES experiments suggest that its empirical phase diagram is not universal and shifted toward overdoped region [2-4]. Therefore, in the present study, we have performed an angle-resolved photoemission spectroscopy (ARPES) measurements to study whether the phase diagram changes depending on sample compositions and hole concentration or not.

In this study, we have performed ARPES measurements systematically to directly investigate the electronic structure of the underdoped, optimally doped, and overdoped Bi2212. ARPES experiments were carried out at BL5U and BL7U. We measured overdoped sample: $Bi_{2.1-x}Pb_xSr_2CaCu_2O_{8+\delta}$ (x = 0.66, T_c ~ 70 K) in the SC and the normal states at BL7U and 5U. We measured underdoped, optimally doped, and overdoped samples: underdoped $Bi_2Sr_2CaCu_2O_{8+\delta}$ (T_c ~ 75 K), optimally doped $Bi_2Sr_2CaCu_2O_{8+\delta}$ (T_c ~ 92 K), overdoped $Bi_2Sr_2CaCu_2O_{8+\delta}$ (T_c ~ 74 K) and optimally doped $Bi_{2.1-x}Pb_xSr_2CaCu_2O_{8+\delta}$ (x = 0.66, T_c ~ 97 K) in the SC and the normal states. High quality single crystals of Bi2212 were cleaved *in-situ* in the ultrahigh vacuum ~5×10^{-9} Pa.

Figure 1 (a) shows the Fermi surface taken at $h\nu$ = 17.8 eV and T = 30 K in the SC state for optimally doped $Bi_2Sr_2CaCu_2O_{8+\delta}$. Fermi surface is clearly observed in wide momentum space.

We have analyzed the ARPES spectra from the nodal to the antinodal region for each sample and determined the Fermi momentum (k_F) for each Fermi surface by fitting of momentum-distribution curves (MDCs) with single Lorentzian or double Lorentzian. Around the nodal region, k_F is defined at Fermi level (E_F) by single Lorentzian. In the offnodal to the antinodal region, k_F is defined at the momentum which shows the gap minimum by double Lorentzian. The k_F points are plotted as shown by red dots (Fig. 1. (a)). We have fitted Fermi surface shape (red dots) by tight binding model (white curve) and estimated the hole concentration of each sample from the Fermi surface area and compared them quantitatively. Figure 1 (b) shows the new phase diagram re-examined by the present ARPES study. As a result, the phase diagram (Fig. 1. (b)) is different from the previous one which was reported by Tallon *et al* [1]. We have figured out that the phase diagram changes depending on sample compositions and hole concentration. As a future work, we continue to study the electric structure of underdoped and overdoped samples to make an entire phase diagram of Bi2212.

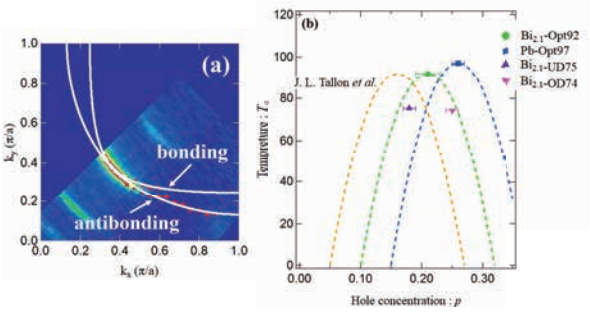

Fig. 1. (a) Fermi surface of optimally doped $Bi_2Sr_2CaCu_2O_{8+\delta}$ in the superconducting state (30 K). (b) The new phase diagram of Bi2212 in the present ARPES study.

[1] J. L. Tallon *et al*., Phys. Rev. B **51** (1995) 12911.
[2] I. M. Vishik *et al*, Proc. Nat. Acd. Sci. **6** (2012)18332-18337.
[3] R. Sobota *et al*, J. Phys. Soc. Jpn. **88** (2019) 064711.
[4] H. Sakamoto *et al*, J. Phys. Soc. Jpn. **85** (2016) 104710.

BL5U

Alkaline-metal-dependent Electronic States in V-based Kagome Metals

T. Kato[1], K. Nakayama[1], Y. Li[2,3,4], Z. Wang[2,3,4], S. Souma[5,6], K. Tanaka[7,8], T. Takahashi[1], Y. Yao[2,3] and T. Sato[1,5,6,9]

[1]*Department of Physics, Graduate School of Science, Tohoku University, Sendai 980-8578, Japan*
[2]*Centre for Quantum Physics, Key Laboratory of Advanced Optoelectronic Quantum Architecture and Measurement (MOE), School of Physics, Beijing Institute of Technology, Beijing 100081, P. R. China*
[3]*Beijing Key Lab of Nanophotonics and Ultrafine Optoelectronic Systems, Beijing Institute of Technology, Beijing 100081, P. R. China*
[4]*Material Science Center, Yangtze Delta Region Academy of Beijing Institute of Technology, Jiaxing, 314011, P. R. China*
[5]*Advanced Institute for Materials Research (WPI-AIMR), Tohoku University, Sendai 980-8577, Japan*
[6]*Center for Science and Innovation in Spintronics (CSIS), Tohoku University, Sendai 980-8577, Japan*
[7]*UVSOR Synchrotron Facility, Institute for Molecular Science, Okazaki 444-8585, Japan*
[8]*School of Physical Sciences, The Graduate University for Advanced Studies (SOKENDAI), Okazaki 444-8585, Japan*
[9]*International Center for Synchrotron Radiation Innovation Smart (SRIS), Tohoku University, Sendai 980-8577, Japan*

Kagome lattice offers a fertile playground to explore exotic quantum phases such as Weyl semimetals, density-wave orders, fractional charge, and superconductivity, owing to the interplay between electron correlation effects and unique band structures such as flat bands, Dirac cone bands, and van Hove singularities. Recently-discovered AV_3Sb_5 (A = alkali metal), in which V atoms form an ideal two-dimensional kagome lattice, provides an excellent opportunity to investigate charge-density wave (CDW) in the kagome lattice. The CDW state of AV_3Sb_5 is characterized by three-dimensional lattice distortions with 2×2×2 or 2×2×4 periodicity depending on the A element. The transition temperature T_{CDW} varies with the A element from 78 K to 103 K. AV_3Sb_5 also exhibits superconductivity in the CDW phase (T_c = 0.92–2.5 K). Besides the CDW and superconductivity in the bulk, AV_3Sb_5 shows an A-element-dependent charge order at the surface. To clarify the origin of these A-element dependent physical properties, elucidation of the bulk and surface band structures is urgently required.

In this study, we have performed high-resolution angle-resolved photoemission spectroscopy (ARPES) measurements of a series of AV_3Sb_5 (A = K, Rb, and Cs). High-quality single crystals of KV_3Sb_5, RbV_3Sb_5, and CsV_3Sb_5 were grown by the self-flux method. High-resolution ARPES measurements were performed by using a MBS-A1 spectrometer at BL5U with linearly-polarized energy-tunable photons of 90-150 eV.

Figures 1(a) and 1(b) show the ARPES intensity plots measured along the high-symmetry line of the bulk Brillouin zone in KV_3Sb_5 [1] and CsV_3Sb_5, respectively. While the band dispersions show overall similarity between the two compounds, a closer look reveals A-element dependence in the energy positions of the electron-like band at the Γ point and the Dirac point at the K point. High-resolution measurements at low temperatures show doubling of some energy bands, indicative of CDW-induced electronic reconstruction. We performed first-principles band calculations to understand the origin of A-element-dependent band structures and their relationship with physical properties in AV_3Sb_5.

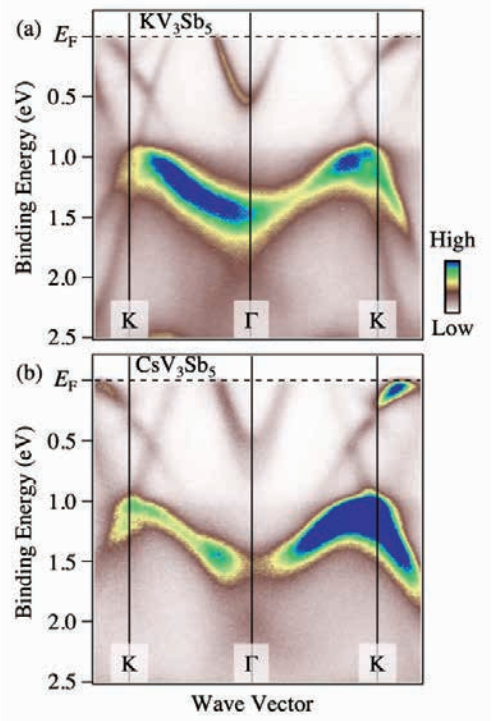

Fig. 1. (a) ARPES intensity along the ΓK cut in KV_3Sb_5 plotted as a function of binding energy and wave vector. (b) Same as (a) but for CsV_3Sb_5.

[1] T. Kato *et al.*, Commun. Mater. **3** (2022) 30.

BL5U

Verification of the Intrinsic Electron Doping Effect in T'-type Cuprate high-temperature Superconductors

M. Miyamoto[1], M. Horio[1], K. Moriya[2], A. Takahashi[3], K. Tanaka[4], Y. Koike[3], T. Adachi[2] and I. Matsuda[1]

[1]*Institute for Solid State Physics, The University of Tokyo, Kashiwa, Chiba 277-8581, Japan.*
[2]*Department of Engineering and Applied Sciences, Sophia University, Tokyo 102-8554, Japan.*
[3]*Department of Applied Physics, Tohoku University, Sendai 980-8579, Japan.*
[4]*UVSOR Facility, Institute for Molecular Science, Okazaki 444-8585, Japan.*

It is believed that in cuprate high-temperature superconductors, superconductivity appears when the carrier is doped by elemental substitution. However, in the electron-doped cuprates $R_{2-x}Ce_xCuO_4$ (R: rare earth) with a T'-type structure, As-grown samples don't show superconductivity and reduction annealing is essential for it, regardless of Ce doping level [1,2]. This is probably due to the presence of excess oxygen on the apical site from the CuO_2 plane in As-grown samples. A crucial role of this reduction annealing has been thought to remove the apical oxygen [3]. In thin-film samples with large surface area relative to volume, the apical oxygen was reduced more efficiently, resulting in a non-doped superconductor [4]. On the other hand, ARPES measurement performed on Pr_2CuO_4 thin films reviled that the carrier concentration was comparable to that of Ce-doped superconductor samples [5]. Therefore, the nature of the electronic structure in T'-type cuprates remains elusive. And it is important to investigate the carrier concentration dependence in isolation from the actual crystal structure degrees of freedom.

In recent years, several studies have shown that the carrier concentration in cuprate high-temperature superconductors can be controlled by alkali metal adsorption [6,7,8]. And our group has previously used a similar technique for a Mott insulator $Ca_3Ru_2O_7$ with successful carrier dosing [9]. This method can dope electrons on the sample's surface without changing its crystal structure, Ce concentration, and oxygen amount. That is, if this method is effective enough, we can distinguish the effects of apical oxygens from that of carrier concentration.

We have carried out the ARPES measurement on $Pr_{1.22}La_{0.7}Ce_{0.08}CuO_4$ As-grown samples at BL5U at 8 K and dosed K on them. To verify the K deposition, we recorded the core level peaks of K 3p and O 2s (Fig.1). The figure shows K was dosed effectively. Fig.2 shows the energy distribution curves at the nodal cut before and after dosing of K. After 10 minutes of dosing, the quasi-particle spectrum around the Fermi level enhanced, and the nodal gap looks closing. After experimenting with various deposition times and deposition counts, we currently concluded that fewer and longer depositions lead to more electron electrons being doped.

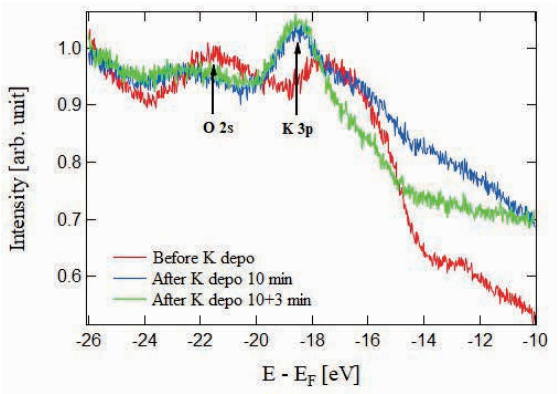

Fig. 1. Energy distribution curves around the K core level

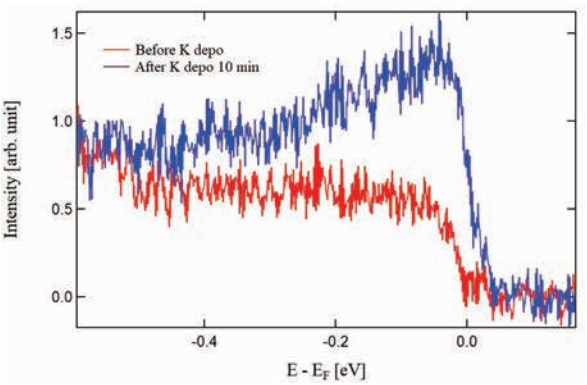

Fig. 2. Energy distribution curves at nodal cut

[1] Y. Tokura, *et al*. Nature **337** (1989) 345.
[2] H. Takagi *et al*. Phys. Rev. Lett. **62** (1989) 10.
[3] M. Horio *et al*. Nat. Commun. **7** (2016) 10567.
[4] O. Matsumoto *et al*. Physica C **469** (2009) 924.
[5] M. Horio *et al*. Phys. Rev. B **98** (2018) 020505(R)
[6] Q. Gao *et al*. Chinese Phys. Lett. **37** (2020) 087402.
[7] S. Kunisada *et al*. Science **369** (2020) 833.
[8] C. Hu *et al*. Nat. Commun. **12** (2021) 1356.
[9] M. Horio *et al*. UVSOR activity report 2021 **49** (2021) 79.

BL5U

Polarization Dependent Orbital States in $Mn_{3-x}Ga$ Studied by angle-resolved Photoemission Spectroscopy

J. Okabayashi[1], Y. Miura[2], K. Tanaka[3], K. Z. Suzuki[4] and S. Mizukami[4]

[1]*Research Center for Spectrochemistry, The University of Tokyo, Bunkyo-ku, Tokyo 113-0033, Japan*
[2]*National Institute for Materials Science (NIMS), Tsukuba, 305-0047, Japan*
[3]*UVSOR Synchrotron Facility, Institute for Molecular Science, Okazaki 444-8585*
[4]*WPI Advanced Institute for Materials Research, Tohoku University, Sendai 980-8579, Japan*

Magnetic ordered alloys have attracted significant attention for use as spintronics materials because they are highly likely to exhibit perpendicular magnetic anisotropy (PMA). Tetragonal $Mn_{3-x}Ga$ alloys are widely recognized as hard magnets which exhibit highly anisotropic, ferrimagnetic, and metallic properties [1]. We have investigated the mechanism of PMA and large coercive fields in $Mn_{3-x}Ga$ by x-ray magnetic circular and linear dichroisms (XMCD / XMLD) [2]. The origin of PMA in $Mn_{3-x}Ga$ alloys can be explained by the quadrupole contribution along the *z*-axis by the charge distribution. The specific crystalline structures provide the elongated *c*-axis direction, which induces the anisotropic chemical bonding, resulting in the anisotropy of electron occupancies in 3*d* states. However, orbital magnetic moments in the Mn sites are almost quenched because of the half-filled occupation.

Although the site-specific charge distributions can be accessed by x-ray absorption spectroscopies, the origin of quadrupole-induced PMA from the viewpoint of the band structures in $Mn_{3-x}Ga$ alloys is not fully understood. Here, we employ the angle-resolved photoemission spectroscopy (ARPES) to unveil the anisotropic band structures in $Mn_{3-x}Ga$ by the comparison with the density-functional theory (DFT) calculations. Especially, in order to clarify the anisotropic electronic structures, the polarization dependent APRES are necessary.

30-nm-thick $Mn_{3-x}Ga$ samples were prepared on MgO (001) substrate using sputtering technique. On the surface of $Mn_{3-x}Ga$ layer, the Mg and MgO capping layers were deposited. The MgO layer was removed by Ar-ion sputtering and the Mg layer was removed by annealing just before the ARPES measurements. We construct the method to remove the Mg layer which does not react chemically with Mn atoms at the interface. Clear low-energy electron diffraction (LEED) patterns were also obtained.

ARPES was performed at BL5U, UVSOR, where the photoemission chamber is connected to the sample preparation chamber. The measurement conditions were set at 15 meV energy resolution and 10 K. Linear polarized beams of *s*- and *p*-polarization were used to detect the orbital symmetry. We employ the photon energy ranges of 60 – 80 eV to enhance the Fe 3*d* photo-ionization cross section, where the Γ-X(M) line is scanned by the angular mode of ±15°.

Figure 1 shows the Fermi surface mapping taken at photon energy of 70 eV. Assuming the inner potential of 10 eV and the work function of 5 eV with the lattice constant along c-axis as 3.90 Å, Γ point can be accessed at 70 eV photon energy. Figures 1(a) and 1(b) show the vertical (*s*-polarized) and horizontal (*p*-polarized) cases in Mn_3Ga. Four-hold symmetric lines are detected. High intensity spots appear at the Γ point and they have a character of *yz* orbital because it can be detected by the *s*-polarized beam in vertical geometry and reproduced by the density-functional-theory (DFT) calculations.

We discuss the quadrupole formation. In the DFT calculations, the virtual spin-flip transitions from occupied up-spin *yz* to down-spin z^2 orbitals correspond to the finite matrix element to the PMA in the perturbation. Therefore, occupied *yz* orbitals detected by ARPES contribute to spin-flipped *yz*-z^2 oblate quadrupole charge distribution, resulting in the PMA. Our finding explains the origin of PMA in $Mn_{3-x}Ga$ comes from not orbital moment anisotropy but elongated charge distribution through the spin-flipped transition in specific orbitals [3], whose results are also supported by XMCD and XMLD [2].

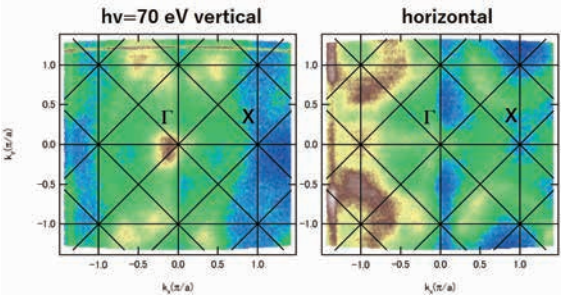

Fig. 1. ARPES images of Mn_3Ga taken at hv=70 eV using (a) *s*-polarized beam and (b) *p*-polarized beam.

[1] S. Mizukami *et al.*, *Scr. Mater.* **118** (2016) 70.
[2] J. Okabayashi *et al.*, *Sci. Rep.* **10** (2020) 9744.
[3] Y. Miura and J. Okabayashi, *J. Phys.: Cond. Mater* **34** (2022) 473001.

BL5U

Impact of Electron Scattering on Seebeck Coefficient

K. Kandai[1], K. Kuga[1, 3], M. Matsunami[1, 2, 3, 4] and T. Takeuchi[1, 2, 3, 4]
[1]*Toyota Technological Institute, Nagoya 468-8511, Japan*
[2]*Research Center for Smart Energy Technology, Toyota Technological Institute, Nagoya 468-8511, Japan*
[3]*CREST, Japan Science and Technology Agency, Tokyo 102-0076, Japan*
[4]*MIRAI, Japan Science and Technology Agency, Tokyo 102-0076, Japan*

The thermoelectric power generation has been considered as one of the most important technologies for constructing a sustainable society. The thermoelectric devices can directly convert heat and electricity using Seebeck and Peltier effects. The maximum efficiency of thermoelectric generator at an absolute temperature T is expressed as an increasing function of the dimensionless figure of merit $ZT = S^2T/\rho\kappa$, where S, ρ, and κ are the Seebeck coefficient, electrical resistivity, and thermal conductivity, respectively, of constituent materials [1].

In the research field of thermoelectric materials, the thermoelectric properties, particularly for Seebeck coefficient, are frequently interpreted and predicted on the basis of electronic structure calculated with density function theory (DFT). However, the Seebeck coefficient of the materials with unconventional electronic structures, such as strongly correlated electron systems (SCES), cannot be accurately described in terms of only the electronic density of states obtained with first-principles DFT calculations. In the theoretical point of view, the main reason is that the energy dependence of relaxation time in the scattering process of conduction electrons is not considered [2, 3]. Although the first principles calculations incorporating dynamical effects are now in progress, it is still difficult to accurately treat an electron correlation effect. In any case, it is necessary to experimentally evaluate the energy dependence of the relaxation time to verify how it affects the Seebeck coefficient. The strong electron correlation is considered as one of the key concepts for developing next-generation thermoelectric materials because some SCES materials possess superior thermoelectric performance. Therefore, for constructing the guiding principle to develop high-performance thermoelectric materials using SCES, it is very important to identify the origin of the preferable thermoelectric properties.

The main purpose of this research is to establish a methodology for experimentally evaluating the energy dependence of the relaxation time of conduction electrons using angle-resolved photoemission spectroscopy (ARPES). As a first step toward achieving this purpose, we select the elemental Cu metal as a sample because the Cu can be expected to show no significant energy dependence of relaxation time of conduction electrons based on its simple electronic structure and band dispersion.

Clean (110) surface of single crystalline Cu was prepared by *in-situ* Ar sputtering and subsequent annealing under ultra-high vacuum condition. The ARPES measurements were performed in the energy range of 32-160 eV at the undulator beamline BL5U of UVSOR facility.

Figure 1 shows the ARPES image of Cu (110) surface at 9 K measured with the photon energy of 100 eV. The free electron-like parabolic dispersion of the (bulk) conduction band is clearly observed in the energy range down to -3 eV below the Fermi level. The energy dependent relaxation time of conduction electrons can be estimated from the peak width both of energy distribution curves and momentum distribution curves. As expected, we confirmed that the energy dependence of the relaxation time shows less significant variation across the Fermi level.

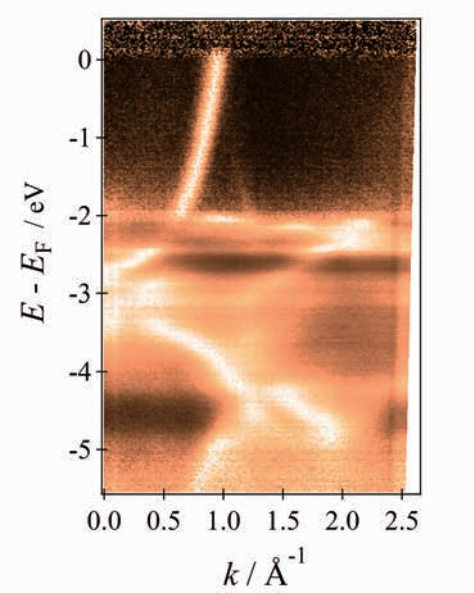

Fig. 1. ARPES image of Cu (110) surface at 9 K measured with 100 eV.

[1] T. Takeuchi, J. Thermoelectrics Soc. Jpn. **9** (2012) 1.
[2] Y. Xia *et al.*, Phys. Rev. Applied **11** (2019) 024017.
[3] B. Xu *et al.*, Phys. Rev. B **102** (2020) 155128.

BL5U

Temperature Dependence of the Band Folding in $TiSe_2$

S. Tanaka[1], K. Ueno[2], K. Fukutani[3] and K. Tanaka[3]
[1]*Sanken, Osaka University, Ibaraki 567-0047, Japan.*
[2]*Graduate School of Science and Engineering Saitama University, Saitama 338-8570, Japan.*
[3]*UVSOR Synchrotron Facility, Institute for Molecular Science, Okazaki 444-8585, Japan.*

Layered material $TiSe_2$ is one of the Transition-Metal-Dichalcogenide (TMDC) and has extensively studied for decays as a typical system of Charge-Density-Wave (CDW) transition. Although excitonic condensation is considered to be the most important factor in the CDW transition in $TiSe_2$ thanks to many experimental and theoretical studies, there are still many unanswered concerns regarding the electrical and atomic structure upon the CDW transition at ~200K. In this article, we use angle-resolved photoelectron spectroscopy (ARPES) to examine how $TiSe_2$'s electronic structures change with temperature. We focus on the specifics of the band folding brought on by the reconstruction of the (2x2x2) superstructure as a result of the CDW transition.

Figs.1 displays the ARPES spectra at 190K (a) and 8K (b) with photon energies of 46eV. The electron pocket at M-points (commonly referred to as the conduction band) and the hole pocket at Γ points (commonly referred to as the valence band) combine to form bands close to the Fermi level in $TiSe_2$. As a result of the CDW transition, where the M point of the original lattice is folded to the Γ point in the rebuilt lattice, our measurements show that the replica of the valence band at the Γ point is clearly visible at the M point at 8K. This is in agreement with how the Brillouin zone was recreated when the CDW transition created the (2x2x2) superlattice. The replica of the conduction band at the M point, on the other hand, is faintly visible even at 8K. We discovered that this replica's intensity greatly fluctuates with photon energy and is quite low at hν=46eV. Moreover, the intensity distribution at the M point significantly changes at two temperatures (see the third panel from the top). This can be explained by the Fermi surface modulation along the k_z line due to the CDW transition.

Together with the production of replicas and changes in the intensity distribution, the energetic profile of the band changes with temperature. At low temperatures, the valence band's energy location is visibly moved downward (see the second panel from the top). This is a defining trait of the bigger gap development brought on by the CDW transition's associated excitonic condensation. The replica located at M at 9K is also energetically displaced to the original valence band at the same temperature. Although the specifics are still being examined, it might also be linked to the modulation of the band along the k_z line.

It should be noted that the replica at M can be dimly detected at 190K, which is considerably lower than the reference's CDW transition temperature. We looked more closely at how the ARPES spectra change with temperature and discovered that the reported temperature of the CDW transition is around the transition temperature determined by energetic profile, which is substantially higher than that determined by replica intensity. Investigations are currently ongoing to determine the physical cause of this behavior.

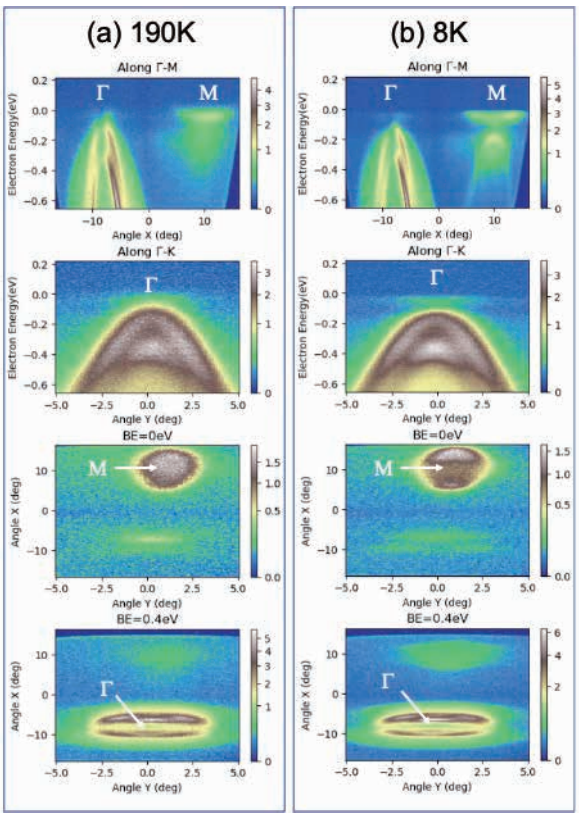

Fig. 1. ARPES spectra of $TiSe_2$ taken at 190K (a) and 8K (b). Upper two panels for (a) and (b) show the intensity maps along the energy-angle axes. Lower two show the iso-energy intensity maps along the x- and y-angles at the binding energies of 0eV and 0.4eV.

BL5U

Doping-Dependent ARPES Study of Nodal Dirac Semimetal Candidate LaTeSb and LaTeBi

R. Saitou[1], N. Kataoka[1], T. Wakita[1], H. Kageyama[1], R. Kondo[1] and T. Yokoya[1,2]
[1]*Graduate School of Natural Science and Technology, Okayama University, Okayama 700-8530, Japan*
[2]*Research Institute for Interdisciplinary Science, Okayama University, Okayama 700-8530, Japan*

$LnTe_{1+x}Sb_{1-x}$ (Ln: lanthanides) is a layered material consisting of alternative stack of a layer of LnTe and a layer of a single Sb square lattice. It is theoretically predicted as a nodal line semimetal [1]. In addition, by selecting a magnetic element as Ln, it is possible to break the time-reversal symmetry. Therefore, it is a material that has the potential to access novel topological phases [2-5]. Our research group are making an effort to control the physical properties of related materials by introducing magnetic elements, substituting Sb with Bi, and changing carrier concentration [6] for the purpose of observing the exotic transport properties peculiar to Dirac electrons. In the present study, we have performed synchrotron angle-resolved photoemission spectroscopy (ARPES) to experimentally observe the electronic structure of the non-magnetic phase and check whether the carrier concentration can be controlled by changing the Te concentration.

$LaTe_{1+x}Sb_{1-x}$ (x = -0.1 and 0.2) and $LaTe_{1+x}Bi_{1-x}$ (x = 0.2) single crystal samples were prepared by a self-flux method. ARPES measurements were performed at BL5U of UVSOR III. Linear polarized light of 70-110 eV energies were used. The energy resolution was set to ~ 40 meV. All samples were cleaved in situ on the (001) plane in an ultrahigh vacuum of less than 5.0 x 10^{-9} Pa and were measured at 20 K.

Figure 1(a) shows the valence band dispersion of $LaTe_{1.2}Bi_{0.8}$ along the Γ-M direction in the Brillouin zone (BZ), measured with the photon energy of 94 eV. White regions, which are the higher-intensity regions, correspond to band dispersions. The band dispersions of the two samples are symmetric with respect to the high symmetry points: Γ and M of the bulk BZ of $LaTe_{1+x}Bi_{1-x}$. This indicates that the band dispersions reflect intrinsic electronic structure of the sample.

Figure 1(b) is the valence band dispersion of $LaTe_{1.025}Bi_{0.975}$ measured with the same experimental condition. Although there are small differences in the intensity distribution between the two ARPES maps, which may originate from the difference in the condition of the measured surface, the band dispersions of the two maps look very similar with each other. On the other hand, from a careful comparison, it was found that the energy positions of the structures in the x = 0.2 sample shift to the higher biding energy side by ~ 100 meV. Two guidelines to demonstrate the energy shift of structures at the Γ point were shown with orange dotted lines. This indicates that increasing Te concentration works as electron doping and one can control the relative energy between the Dirac nodal line and the Fermi level (E_F) by changing the relative concentration between Te and Bi. Since the energy position of the Dirac nodal line in the x = 0.025 sample was found to be located above E_F, the Dirac nodal line in the x = 0.2 sample may be located closer to E_F or just at E_F. Further ARPES studies along the X-R line in the Brillouin zone, where the Dirac nodal line is expected to is located by band structure calculations, is planned to confirm this anticipation.

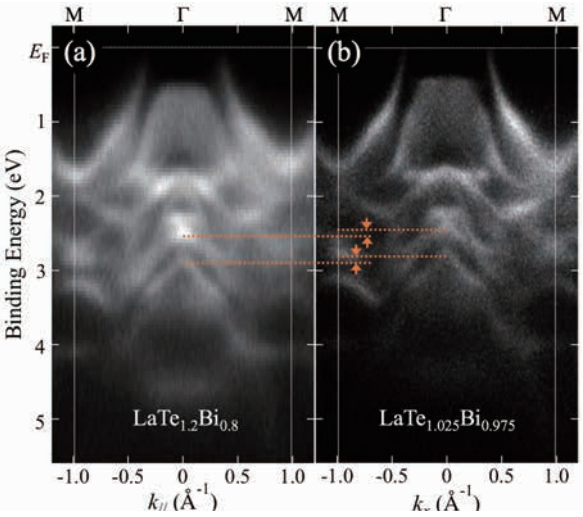

Fig. 1. Comparison of ARPES intensity maps along the Γ-M direction of $LnTe_{1+x}Bi_{1-x}$ between (a) x = 0.2 and (b) x = 0.025, measured with 94 eV photons and at 20 K.

[1] A. Weiland *et al*., APL Mater. **7** (2019) 101113.
[2] Y. Wang *et al*., Phys. Rev. B **103** (2021) 125131.
[3] S. Yue *et al*., Phys. Rev. B **102** (2020) 155109.
[4] P. Gebauer *et al*., Chem. Mater. **33** (2021) 2420.
[5] L. M. Schoop *et al*., Sci. Adv. **4** (2018) eaar2317.
[6] R. Kondo, in preparation.

BL5U, 7U

Symmetry Reduction of the Electronic Structure in Heavily Overdoped Pb-Bi2201 Observed by Angle-resolved Photoemission Spectroscopy

Y. Miyai[1], T. Kurosawa[2], M. Oda[3], M. Arita[4], K. Tanaka[5], S. Ideta[4] and K. Shimada[4]

[1]*Graduate School of Science, Hiroshima University, Higashi-Hiroshima 739-8526, Japan*
[2]*Fuculty of Science and Engineearing, Muroran Institute of Technology, Muroran, 050-8585, Japan*
[3]*Department of Physics, Hokkaido University, Sapporo 060-0809, Japan*
[4]*Hiroshima Synchrotron Radiation Center, Hiroshima University, Higashi-Hiroshima 739-8526, Japan*
[5]*UVSOR-III Synchrotron, Institute for Molecular Science, Okazaki, 444-8585, Japan*

High transition-temperature (T_C) cuprate superconductors have attracted much interest since their discovery in 1986 for their high superconducting transition temperature as well as unusual physical properties such as a pseudogap state and a nematic phase [1, 2]. Superconductivity occurs in the CuO_2 plane and the Cu $3d_{x^2-y^2}$ state forms the Fermi surface (FS). One can expect a four-fold symmetry of the FS because the CuO_2 plane is tetragonal. However, symmetry reduction of the electronic structure has been reported in Bi-based cuprate superconductors recently [2, 3]. Similar symmetry reduction or *nematicity* was found in iron-based superconductors, the electronic states break the four-fold rotational symmetry of the lattice [4, 5]. Although nematicity in electron liquids has attracted much interest, the rotational symmetry breaking in the electronic states for high-T_C cuprate superconductors has not been clarified yet.

Here, we have examined the symmetry of the electronic structure of heavily overdoped $(Bi,Pb)_2Sr_2CuO_{6+\delta}$ (Pb-Bi2201) ($T_C < 2.5$ K) using high-resolution angle-resolved photoemission spectroscopy (ARPES). We selected Bi2201 because it has a single CuO_2 plane and one can exclude the complexity of the electronic structure such as bilayer splitting derived from two CuO_2 planes. Furthermore, the pseudogap disappears in the heavily overdoped sample and one can clearly see the entire FS in the normal state without Fermi arc.

Figures. 1(a) and 1(b) show the FS obtained by rotating the sample around the two nodal directions taken at $h\nu = 60$ eV and $T = 20$ K with the *s*-polarization geometry. We have found that the value of $2k_F$ (k_F: Fermi momentum) for the two nodal directions are different; $2k_F^{(1)} = (7.996 \pm 0.003) \times 10^{-1}$ Å^{-1} (Fig. 1(a)) and $2k_F^{(2)} = (8.572 \pm 0.003) \times 10^{-1}$ Å^{-1} (Fig. 1(b)). This difference independents of temperature from $T = 20$ K to 260 K. In addition, we reveal that the energy dependence of the quasiparticle lifetime broadening is also different for these two nodal directions. The situation is similar for the samples with $T_C = 4$, 6, and 10 K. Our results indicate C_4 symmetry breaking of the electronic structure in the CuO_2 plane in the heavily overdoped Pb-Bi2201, which might be related to a charge order formation in the heavily overdoped Pb-Bi2201 as observed by resonant inelastic X-ray scattering [6], and/or the nematic phase associated with the Pomeranchuk instability as suggested by Raman scattering measurements on Bi2212 [7].

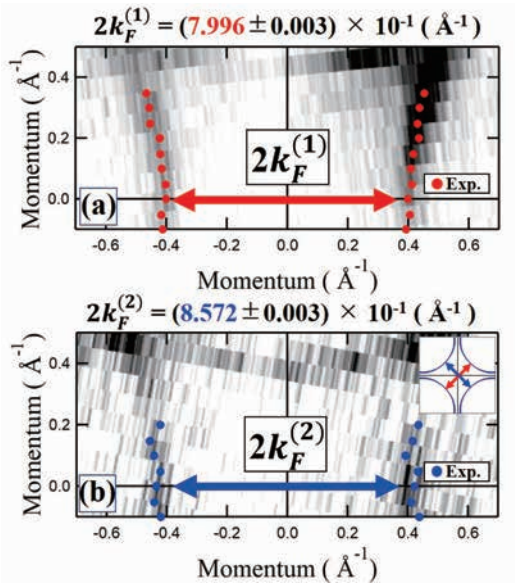

Fig. 1. (a), (b) Fermi surface mapping obtained by rotating around the two nodal directions taken at $h\nu$ = 60 eV and T = 20 K with the *s*-polarization geometry. Red and blue markers indicate the Fermi surface points determined from the peaks of the momentum distribution curves. We determine $2k_F$ values ($2k_F^{(1)}$ and $2k_F^{(2)}$) for the two nodal directions as shown in the inset of panel (b).

[1] M. Hashimoto *et al.*, Nat. Phys. **10** (2014) 483.
[2] S. Nakata *et al.*, npj Quantum Mater. **6** (2021) 86.
[3] Y. Zheng *et al.*, Sci. Rep. **7** (2017) 8059.
[4] H. C. Xu *et al.*, Phys. Rev. Lett. **117** (2016) 157003.
[5] J-H. Chu *et al.*, Science **329** (2010) 824.
[6] Y. Y. Peng *et al.*, Nat. Mater. **17** (2018) 697.
[7] N. Auvray *et al.*, Nat. Commun. **10** (2019) 5209.

BL6B

Far- and Mid-infrared Absorption on the Single-crystal Pentacene

Y. Nakayama[1, 2], K. Yamauchi[1], Y. Baba[1] and J. Miyamoto[1]
[1]*Department of Pure and Applied Chemistry, Tokyo University of Science, Noda 278-8510, Japan*
[2]*Institute for Molecular Science, Okazaki 444-8585, Japan*

Electronic coupling with molecular vibrations and/or lattice phonons is one of the key issues for the consideration of charge carrier transport in organic semiconductor solids. In the present work, we conducted infrared absorption measurements on the pentacene single-crystal (PnSC) samples as a model case of high-mobility organic semiconductors for the elucidation of the electron-vibration coupling in well-defined solid-state molecules.

Infrared absorption measurements were carried out at BL6B. A Si bolometer or a HgCdTe detector was used for the signal detection in a wave number range of 100 – 700 cm^{-1} (FIR) or 700 – 7000 cm^{-1} (MIR), respectively. Details of the PnSC samples and measurement geometry were the same as reported previously [1]. The data were collected by changing the sample azimuthal angle by 180° in 15° and 45° intervals for the FIR and MIR measurements, respectively. In this report, angularly averaged spectra were used for the analyses. Spectra measured through a diamond plate were adopted as blank spectra (I_0) to derive the absorbance of PnSCs.

Figure 1 shows a typical FIR spectrum of PnSC in a region where prominent peaks were observed. A persistent background modulation of a "frequency" at (5.9 ± 0.2) cm^{-1} is filtered out for further analyses. The spectral feature can be attributed to two vibration modes predicted to be at 476.9 cm^{-1} and 491.7 cm^{-1}. In the present measurements, twenty vibration modes were assignable in the spectra. Energy deviations of the experimental vibration peaks with respect to the theoretical values calculated in the B3-LYP/6-31g(d) level are plotted in Fig. 2, where a recommended "scale factor" for the calculated wavenumbers [2] is indicated as a standard. As the vibration mode #88 (in-plane scissoring of the backbone) exhibited the best match, the relative intensity for each spectral peak is derived with respect to the mode #88 intensity and plotted as a function of the corresponding calculated relative intensity in Fig. 3. Further discussion on the results is yet under consideration.

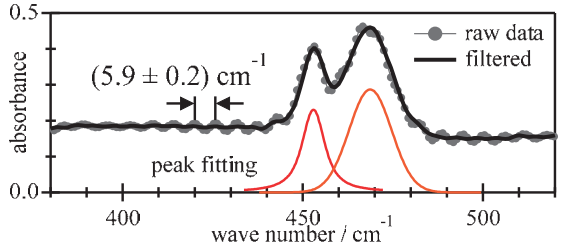

Fig. 1. FIR absorption spectrum on the PnSC.

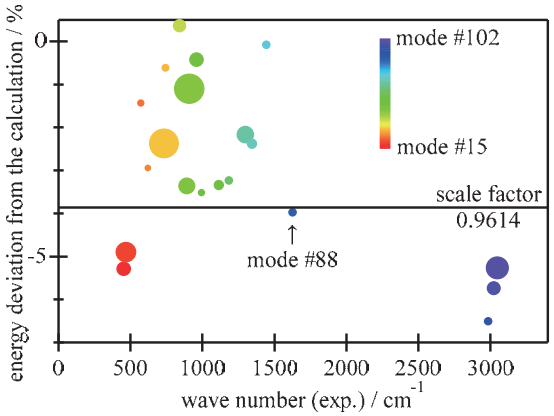

Fig. 2. Energy deviation of the experimental peak positions with respect to the calculated values. The size of the symbols indicates the peak intensity.

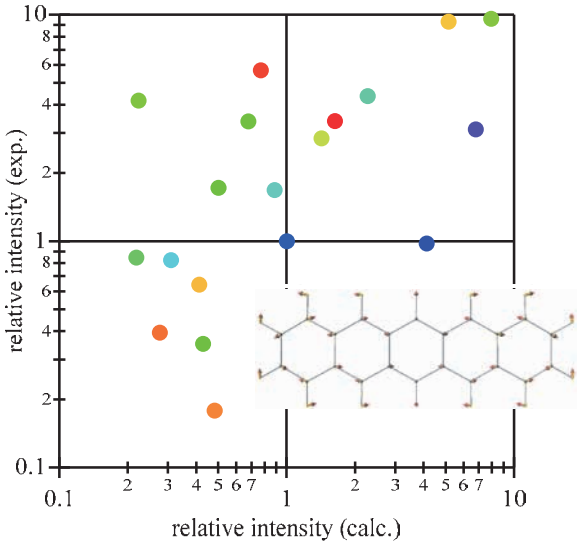

Fig. 3. Experimental relative peak intensity plotted as a function of the calculated magnitudes. The color of the symbols corresponds to the mode number indicated in Fig. 2. The inset image shows the mode #88 vibration of the pentacene molecule.

[1] Y. Nakayama and J. Miyamoto, UVSOR Activity Report 2020 (2021) 83.
[2] J. P. Merrick, D. Moran and L. Radom., J. Phys. Chem. A **111** (2007) 11683.

BL7U

ARPES Study of a chalcopyrite-type Topological Insulator Candidate

T. Iwaya[1], A. Honma[1], K. Nakayama[1], K. Sugawara[1,2], S. Souma[2,3], K. Tanaka[4,5], T. Takahashi[1], K. Segawa[6] and T. Sato[1,2,3,7]

[1]*Department of Physics, Graduate School of Science, Tohoku University, Sendai 980-8578, Japan*
[2]*Advanced Institute for Materials Research (WPI-AIMR), Tohoku University, Sendai 980-8577, Japan*
[3]*Center for Science and Innovation in Spintronics (CSIS), Tohoku University, Sendai 980-8577, Japan*
[4]*UVSOR Synchrotron Facility, Institute for Molecular Science, Okazaki 444-8585, Japan*
[5]*School of Physical Sciences, The Graduate University for Advanced Studies (SOKENDAI), Okazaki 444-8585, Japan*
[6]*Department of Physics, Kyoto Sangyo University, Kyoto 603-8555, Japan*
[7]*International Center for Synchrotron Radiation Innovation Smart (SRIS), Tohoku University, Sendai 980-8577, Japan*

Three-dimensional topological insulators (3D TIs) are a novel quantum state of matter where the bulk band gap induced by a strong spin-orbit coupling leads to the appearance of gapless Dirac-cone surface states protected by time-reversal symmetry. The discovery of 3D TIs has further stimulated the search for novel topological materials. From the viewpoint of the crystal symmetry, most of the 3D TIs so far discovered, e.g., Bi_2Se_3, Bi_2Te_3, and $TlBiSe_2$, have the spatial inversion symmetry in the crystal. On the other hand, there are several theoretical proposals of TI candidates with broken inversion symmetry. There is a demand to experimentally discov such symmetry-broken phase because a peculiar phenomenon which cannot be realized in inversion-symmetric TIs is predicted to emerge.

Here we focus on $CdGeAs_2$ which crystalizes in a chalcopyrite structure with $I\bar{4}2d$ space group. As seen from Fig. 1(a), the crystal consists of a stack of zinc blend structure and hence breaks the inversion symmetry. Recent theoretical study predicted $CdGeAs_2$ to be a topological insulator [1]. Owing to the inversion symmetry breaking, $CdGeAs_2$ can have nontrivial Fermi arc surface states and lead to a giant magnetoelectric effect. To establish a material platform of such exotic phenomena, experimental elucidation of the topological properties in $CdGeAs_2$ is highly desired.

In this study, we have performed high-resolution angle-resolved photoemission spectroscopy (ARPES) of $CdGeAs_2$ at BL7U. Single crystals of $CdGeAs_2$ were grown by the vapor-phase growth method. Clean surfaces for ARPES were obtained by *in situ* cleaving of the crystals. By x-ray laue diffraction, the cleaved surface was determined to be (101) plane. ARPES measurements were performed by using a MBS-A1 spectrometer at BL7U with linearly-polarized energy-tunable photons.

Figure 1(b) shows the ARPES intensity plot along a momentum cut crossing the Γ point of the bulk Brillouin zone. We observed several highly dispersive hole-like bands centered at the Γ point. These bands are reproduced by the band calculations shown by red curves and attributed to the bulk valence bands with dominant As 4*p* orbital character. We further performed detailed measurements over the entire Brillouin zone with tuning photon energies to find a signature of the topological surface states.

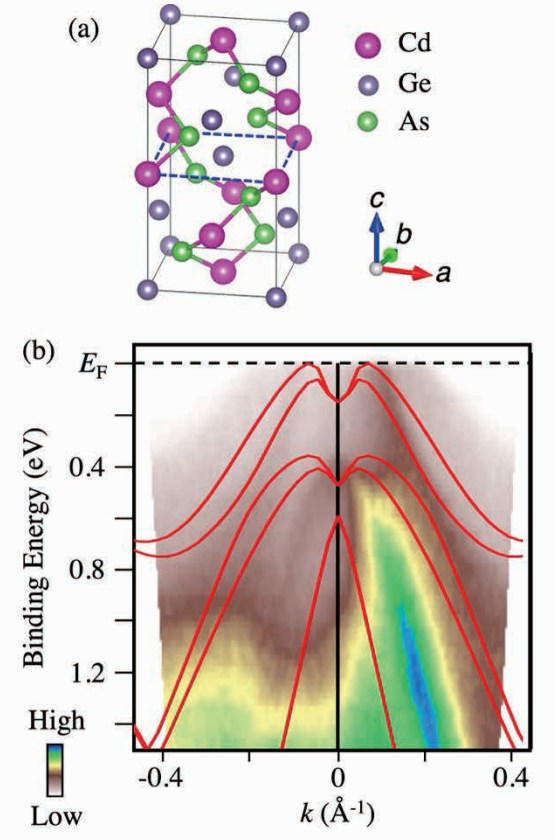

Fig. 1. (a) Three-dimensional view of the crystal structure of $CdGeAs_2$. (b) ARPES intensity plotted as a function of binding energy and wave vector measured in $CdGeAs_2$. Red curves are the result of first-principles band structure calculations.

[1] K. Osumi *et al.*, Commun. Phys. **4** (2021) 211.

BL7U

Electronic Structure of the five-fold oxygen-coordinated Cuprate Superconductor

M. Horio [1], M. Miyamoto[1], X. Peiao[2], K. Tanaka[3], T. Taniguchi[2], M. Fujita[2] and I. Matsuda[1]
[1]*Institute for Solid State Physics, The University of Tokyo, Kashiwa, Chiba 277-8581, Japan*
[2]*Institute for Materials Research, Tohoku University, Katahira, Sendai 980-8577, Japan*
[3]*UVSOR Facility, Institute for Molecular Science, Okazaki 444-8585, Japan*

Structural isomers of so-called 214-type cuprates provide a unique platform for studying the effect of oxygen coordination on the electronic structure of cuprate superconductors. The local oxygen coordination around copper can be varied from a six-fold octahedron (T-type) to a four-fold square plane (T'-type). It is known that a decrease in the oxygen coordination number leads to a decrease in the charger-transfer gap and hence electron correlation [1]. However, while the T-type cuprates can be doped only with holes, the T'-type cuprates do not usually accept hole doping [2], preventing direct comparisons. On the other hand, T*-type cuprates with five-fold pyramidal oxygen coordination can be hole-doped and are directly comparable to the T-type one [3]. Optical conductivity studies of the parent compound suggest that T*-type cuprates have a smaller charge transfer gap than T-type [1]. As-grown samples of the T*-type cuprates are known to have oxygen defects in the apical site, and in order to induce superconductivity, post-growth high-pressure oxygen annealing is required [3,4]. Recent oxygen K-edge x-ray absorption spectroscopy (XAS) studies [5] found a dramatic increase in doped holes upon oxygen annealing, consistent with compensation of oxygen defects. The T_c of O_2-annealed T*-$SmLa_{1-x}Sr_xCuO_4$ (SLSCO) monotonically increases with decreasing Sr concentration [6], in contrast to the dome-like behavior of the T-type $La_{2-x}Sr_xCuO_4$ (LSCO). The different superconducting properties between T*- and T-type cuprates suggest a significant difference in the electronic structure associated with a change in the coordination number of oxygen. However, the electronic structure of T*-type cuprates, including its evolution by annealing, is still largely unknown [7], even 35 years after its discovery. In this work, we performed angle-resolved photoemission spectroscopy (ARPES) measurements on the T*-type cuprates T*-SLSCO.

Single crystals of T*-SLSCO (x = 0.25) were grown by the travelling-solvent floating-zone method. After post-growth O_2 annealing at 500 °C and 45 MPa for 72 hours, the sample showed superconductivity below T_c = 17 K. ARPES measurements were performed at BL7U of UVSOR at T = 7 K and $h\nu$ = 18 eV.

Fig. 1 presents ARPES spectra obtained from T*-SLSCO. While the spectral weight becomes diminishingly small as approaching the Fermi level, Fermi crossing is observed for the nodal spectrum (#1). As moving away from the nodal region, the band become gapped with a strong suppression of the spectral weight, signifying the opening of a pseudogap. According to a previously reported phase diagram for T*-SLSCO, x = 0.25 corresponds to deep in the overdoped region. This is apparently incompatible with the present observation of the robust pseudogap, which is typical of underdoped or optimally doped samples. The result suggests a potentially unique phase diagram of T*-type cuprates, which deserves further systematic investigations with varying hole concentrations.

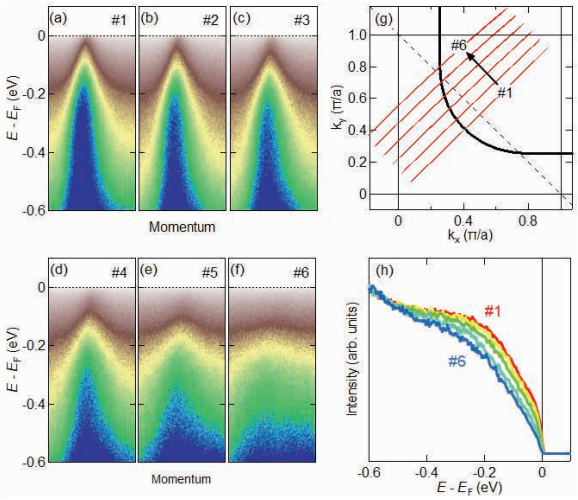

Fig. 1. ARPES spectra of O_2-annealed T*-SLSCO (x = 0.25). (a)-(f) Energy-momentum maps from the nodal to antinodal regions. Cut positions are indicated in (g). (h) Energy distribution curves at each k_F point.

[1] Y. Tokura *et al.*, Phys. Rev. B **41** (1990) 11657.
[2] N. P. Armitage *et al.*, Rev. Mod. Phys. **82** (2010) 2421.
[3] J. Akimitsu *et al.*, Jpn. J. Appl. Phys. **27** (1988) L1859.
[4] F. Izumi *et al.*, Physica C **158** (1989) 440.
[5] S. Asano *et al.*, J. Phys. Soc. Jpn. **89** (2020) 075002.
[6] T. Kakeshita *et al.*, J. Phys.: Conf. Ser. **150** (2009) 052089.
[7] A. Ino *et al.*, Physica B **351** (2004) 274.

BL7U

Angle-Resolved Photoemission Study of Solid Electrolytes $Li_{3x}La_{2/3-x}TiO_3$ Bulk Single Crystal

S. Koyama[1], M. Nakatake[2], S. Takakura[3], K. Tanaka[4,5], Y. Fujiwara[6], T. Taishi[6], H. Moriwake[7], Y. Iriyama[1] and T. Ito[1,3]

[1]*Graduate School of Engineering, Nagoya University, Nagoya 464-8603, Japan*
[2]*Aichi Synchrotron Radiation Center, Seto, 489-0965, Japan*
[3]*Synchrotron radiation Research center, Nagoya University, Nagoya 464-8603, Japan*
[4]*UVSOR Facility, Institute for Molecular Science, Okazaki 444-8585, Japan*
[5]*The Graduate University for Advanced Studies, Okazaki 444-8585, Japan*
[6]*Faculty of Engineering, Shinshu University, Nagano 380-8553, Japan*
[7]*Nanostructures Research Laboratory, Japan Fine Ceramics Center, Nagoya 456-8587, Japan*

With the recent expansion of the use of lithium-ion secondary batteries, development of all-solid-state batteries using lithium-ion conductive inorganic solid electrolytes has been progressing to realize further safety, high energy density, and high output, etc. On the other hand, the valence-band electronic structure, which is essential to understand the relation between lithium-ion and electron conductivity in inorganic solid electrolytes, has not been well elucidated yet, though the chemical analysis using operand X-ray photoemission has intensively been applied on the system [1,2]. In this study, we have performed angle-resolved photoemission spectroscopy (ARPES) measurements on $Li_{3x}La_{2/3-x}TiO_3$ (LLTO) bulk single crystals to clarify the effect of lithium on the electronic structure of solid electrolytes. The results were compared with the ARPES study on $Li_xLa_{(1-x)/3}NbO_3$ (LLNbO) in which relatively lower Li ion conductivity has been reported [3].

ARPES measurements were performed at the UVSOR-III BL7U. Data were acquired with hν = 18 eV at room temperature. To minimize spectral modification due to photo-irradiation, photon flux was sufficiently reduced (<3E+10 photons/s) during all measurements. Single crystals were cleaved in situ along (100) plane, where La/Li rich (A1) and La/Li poor layers (A2) appear alternately (inset: Fig.2 (a)).

Figure 1 (a) and (b) show ARPES spectra and band structure along the ΓX line of LLTO, respectively. The observed band structure mainly consists of two peaks around 4 and 7 eV with the band gap about 3 eV. From the comparison with DFT calculation (Fig. 2(a)) [4], we found that the valence band width (~5 eV) seems to be similar between the ARPES and calculation.

When we compare the ARPES band structure between LLTO and LLNbO bulk single crystals [3], we found that the valence band width of LLTO becomes about 1 eV narrower than LLNbO, while the band gap size observed as almost the same. In Fig. 2(a) and (b), the observed differences of band width as well as the spectral features between LLTO and LLNbO are qualitatively reproduced by the DFT calculations. The results indicate the applicability of ARPES to study the electronic structure of solid electrolytes single-crystal.

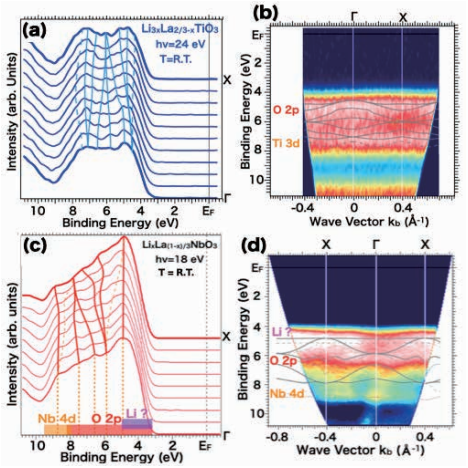

Fig. 1. ARPES spectra (a,c) and band structures (b,d) along the ΓX line of $Li_{3x}La_{2/3-x}TiO_3$ (a,b) and $Li_xLa_{(1-x)/3}NbO_3$ (c,d), respectively. Solid and dashed lines are guides for eyes.

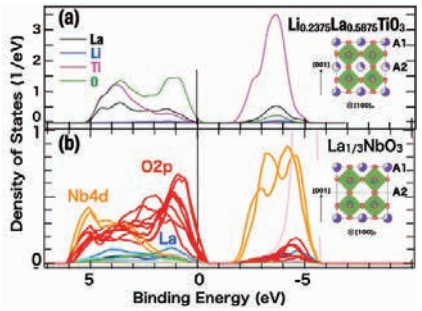

Fig. 2. The partial density of states of $Li_{0.2375}La_{0.5875}TiO_3$ [4] (a) and $La_{1/3}NbO_3$ (b), respectively. Inset of each panel shows average crystal structures of LLTO and LLNbO, respectively.

[1]K. Hikima *et al*., Commn. Chem. **5** (2022) 52.
[2]K. N. Wood *et al*., Nature Commun. **9** (2018) 2490.
[3]Y. Fujiwara *et al*., J. Cryst. Growth **433**, 48-53 (2016); Y. Fujiwara *et al*., Jpn. J. Appl. Phys. **55**, 090306 (2016).
[4]K. Dai *et al*., J. Mater. Sci. **57** (2022) 2825.

BL7U

Electronic Structure of Layered Nitride Chloride ZrNCl by ARPES

N. Kataoka[1], R. Saitou[1], M. Tanaka[2] and T. Yokoya[1,3]

[1]*Graduate School of Natural Science and Technology, Okayama University, Okayama 700-8530, Japan*

[2]*Graduate School of Engineering, Kyushu Institute of Technology, Kitakyushu 804-8550, Japan*

[3]*Research Institute for Interdisciplinary Science, Okayama University, Okayama 700-8530, Japan*

Electron-doped layered nitride chloride ZrNCl shows superconductivity of $T_c \sim 16$ K by intercalating alkali metals between the layers[1]. Observed exotic properties have suggested that its superconducting properties are difficult to be explained by the BCS theory[2]. Theoretical studies have proposed a model mediated by spin fluctuations[2] and a superconducting mechanism with a BCS-BEC crossover[3]. However, there are no experimental observations of the electronic structure by ARPES measurements, and the superconducting mechanism has remained undetermined. This is due to the fact that alkali metal-inserted ZrNCl is easily oxidized in the atmosphere and that it is difficult to obtain large single-crystal samples. In this study, we prepare electron-doped ZrNCl by depositing alkali metals in vacuum on a relatively large parent material. The electronic structure of ZrNCl before and after alkali metal deposition is studied by ARPES.

Samples were prepared by vacuum evaporation on cleaved ZrNCl single crystals at room temperature in ultrahigh vacuum using a Potassium(K) deposition source. The samples were transferred from the evaporation chamber to the measurement chamber. ARPES measurements were performed at BL7U of UVSOR III with 28–40 eV photons and an energy resolution of 15~20 meV. The measurement temperature was 40 K.

Figures 1(a) and 1(b) show the band dispersion of Γ-M line in ZrNCl before and after K deposition. Before deposition, the top of the valence band was located at ~ 3.0 eV at the Γ point and the bottom of the valence band was located at ~ 8.3 eV at the M point. After K deposition, the band near the Γ point, the top of the valence band, is shifted to the higher binding energy side by about 100 meV. The energy position of the bottom of the valence band at the M point did not change significantly. A theoretical study predicted a bandwidth of 6.1 eV[4] for ZrNCl and significant expansion of the valence band width by alkali metal intercalation. This is different from nearly the same band width between before and after K deposition. Regarding the change of the bandwidth by K evaporation, it is possible that the result is not an intrinsic change in electronic structure, but rather reflect an effect of the surface state formed by the deposition. For near the Fermi energy (E_F), after deposition, a clear dispersive band was not observed at the K point, where electron pockets are expected to appear theoretically. On the other hand, angle integrated spectrum near E_F shows a small structure, whose energy position and spectral shape are similar to the structure before K deposition (Figure 2), although the intensity increases after K deposition. Based on previous studies, the structure before evaporation may be a state caused by hydrogen impurities[5]. Further studies, including comparison with theoretical studies that also take the surface state into account, are necessary to understand these observations.

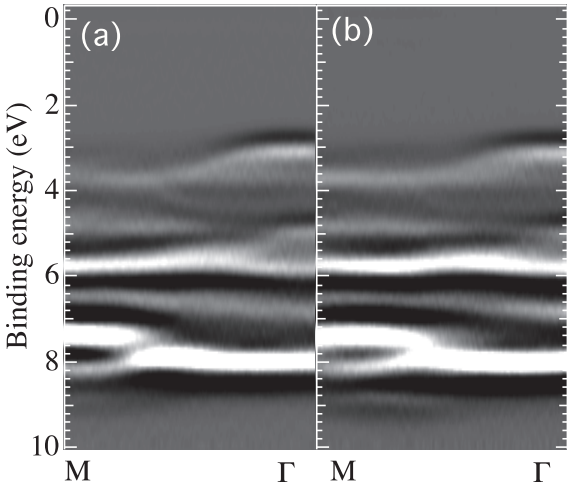

Fig. 1. 2nd-derivative ARPES intensity maps along Γ-M of ZrNCl before (a) and after (b) K deposition.

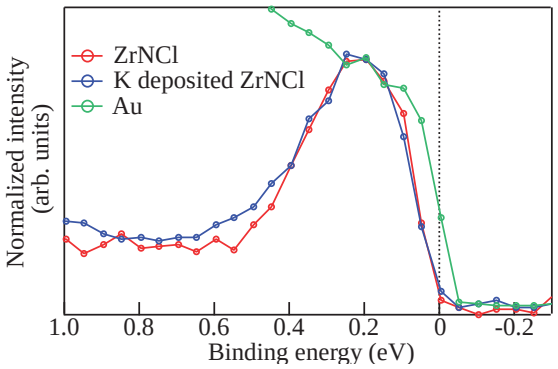

Fig. 2. Angle-integrated spectra near E_F of ZrNCl before and after K deposition, compared with Au.

[1] Y. Kasahara *et al.*, Physica C **514** (2015) 354.
[2] K. Kuroki, Phys. Rev. B **81** (2010) 104502.
[3] Y. Nakagawa *et al.*, Science **372** (2021) 190.
[4] Z. P. Yin *et al.*, Phys. Rev. X **3** (2013) 021011.
[5] T. Yokoya *et al.*, Phys. Rev. B **70** (2004) 193103.

BL7U

Low-Energy ARPES Study on the Electronic Structure of Cr_2Se_3

C.-W. Chuang[1], T. Kawakami[1], T. Kato[1], K. Sugawara[1,2], K. Nakayama[1], S. Souma[2,3], K. Tanaka[4,5], A. Chainani[6], T. Takahashi[1], K. Segawa[7] and T. Sato[1,2,3,8]

[1]*Department of Physics, Graduate School of Science, Tohoku University, Sendai 980-8578, Japan*
[2]*Advanced Institute for Materials Research (WPI-AIMR), Tohoku University, Sendai 980-8577, Japan*
[3]*Center for Science and Innovation in Spintronics (CSIS), Tohoku University, Sendai 980-8577, Japan*
[4]*UVSOR Synchrotron Facility, Institute for Molecular Science, Okazaki 444-8585, Japan*
[5]*School of Physical Sciences, The Graduate University for Advanced Studies (SOKENDAI), Okazaki 444-8585, Japan*
[6]*National Synchrotron Radiation Research Center, Hshinchu, 30077, Taiwan ROC*
[7]*Department of Physics, Kyoto Sangyo University, Kyoto 603-8555, Japan*
[8]*International Center for Synchrotron Radiation Innovation Smart (SRIS), Tohoku University, Sendai 980-8577, Japan*

Transition metal chalcogenides (TMCs) are a group of materials that have been intensively studied for long time because of a wide variety of physical properties depending on their crystal structure and composition, including superconductivity, metal-insulator transition, and three-dimensional topological insulators. Recently, TMCs have attracted even more attention because their atomic layer films show dramatically different properties from those of bulk counterparts, such as Ising superconductivity, spin-valley Hall effect, two-dimensional topological insulators. To understand and control these exotic properties, an experimental study on the electronic structure of TMCs is of crucial importance.

Here we focus on a chromium-based TMC, Cr_2Se_3 with the two-dimensional rhombohedral crystal structure (NiAs type; $P6_3/mmc$). Bulk Cr_2Se_3 is known as a thermoelectric material with a large figure of merit. This material is attracting attention because of intriguing magnetic properties; bulk Cr_2Se_3 exhibits a collinear antiferromagnetic order with T_N ~ 45 K, followed by a successive transition to a non-collinear antiferromagnetic phase [1], whereas monolayer Cr_2Se_3 was predicted to be a ferromagnet which potentially hosts a half metallic ground state [2]. To clarify the interplay between these magnetic orders and the electronic structure, we have performed angle-resolved photoemission spectroscopy (ARPES) measurements of bulk and monolayer Cr_2Se_3.

High-quality bulk Cr_2Se_3 was grown by flux method. Monolayer Cr_2Se_3 was grown on graphene/SiC by molecular-beam epitaxy method. High-resolution ARPES measurements were performed by using a MBS-A1 spectrometer at BL7U with linearly-polarized energy-tunable photons.

Figure 1 shows representative ARPES results in the antiferromagnetic state of bulk Cr_2Se_3, i.e. ARPES spectra measured along a momentum cut crossing the Γ point [Fig. 1(a)] and the corresponding intensity plot [Fig. 1(b)]. We observed several band dispersions in the energy range of the Fermi level (E_F) to 5 eV, such as a relatively flat hole-like band near E_F and a highly dispersive hole-like band topped at 2 eV below E_F at the Γ point. Upon increasing the temperature, we found a finite change in spectral intensity across T_N, indicative of magnetism-induced electronic reconstructions. We also measured the photon-energy dependence of the band dispersion and determined the three-dimensional bulk band structure. In addition, we found a clear difference in the band structure and its temperature dependence between bulk and monolayer Cr_2Se_3. The obtained ARPES results were compared with first-principles band structure calculations to understand the temperature- and thickness-dependent changes in the band structure.

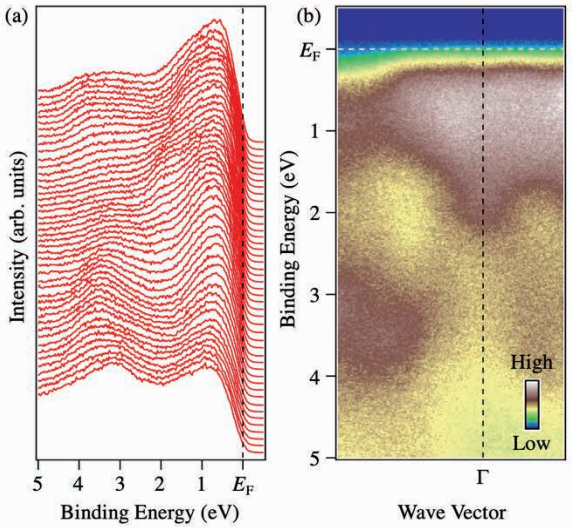

Fig. 1. (a) ARPES spectra in the valence band region of bulk Cr_2Se_3 measured at T = 30 K with 21-eV photons, and (b) corresponding intensity plot as a function of binding energy and wave vector.

[1] Y. Adachi *et al.*, J. Phys. Soc. Jpn. **63** (1994) 1548.
[2] J.-Y. Chen *et al.*, Adv. Electron. Mater. **6** (2020) 2070001.

BL7U

Polarization-Dependent Photoemission from the Folded Band of $TiSe_2$

S. Tanaka[1], K. Ueno[2], K. Fukutani[3] and K. Tanaka[3]
[1]*Sanken, Osaka University, Ibaraki 567-0047, Japan.*
[2]*Graduate School of Science and Engineering Saitama University, Saitama 338-8570, Japan.*
[3]*UVSOR Synchrotron Facility, Institute for Molecular Science, Okazaki 444-8585, Japan.*

It is crucial for the creation of symmetry-broken collective phases, such as charge density waves and topological and superconducting states of matter, that crystalline solids have a momentum-dependent orbital structure. Measurements with the polarization-dependent angle-resolved photoelectron spectroscopy (ARPES) can provide important details on the material's orbital texture. Layered material $TiSe_2$, one of the transition-metal-dichalcogenide (TMDC) and known as a model system of the charge-density wave (CDW) transition, is a good candidate to make such a study, since $TiTe_2$, which has a similar electronic structure to $TiSe_2$ but does not exhibit the CDW transition, has been recently well studied by similar method[1].

Fig. 1 shows ARPES spectra near the Γ point at 10K taken using the vertically polarized photon of 7eV. The cutting plane along the kx (at ky=0) and ky (at kx=0) axes is shown in the lower panels, while the upper panel displays the photoelectron intensity map along the kx-ky plane at the Fermi level. The band below the BE~0.07eV is the Se4p/Ti3d valence band, and the band near the Fermi level is the replica of the Ti3d-derived conduction band originally located at the M point, which is caused by the formation of the (2x2x2) superlattice as a result of the CDW transition. The assignment can be confirmed by the observation of the extinction of this feature at higher temperatures. The photoelectron intensity distribution, however, is different from the original Ti3d conduction band at M. White dot lines represent the replica's anticipated traces, which originate from the six nearby M points, and only a portion of them have photoelectrons visible. This must be due to the matrix element effect, which relates to the orbital texture and also discerning structural and collective phases of the material in the CDW transition.

We measure the polarization-dependent ARPES by rotating the sample along the surface normal to provide information about the matrix element effect (azimuthal rotation). The vertically-polarized photon was used, and the polarization vector is always parallel to the sample surface. The variation in the photoelectron distribution as a result of azimuthal angle is depicted in Figure 2. Shiny branches shift as the polarization vector's angle with the sample axis changes. It makes it evident that the matrix element is crucial, and the in-depth research, currently underway, will yield information regarding the orbital texture of the replica band formed by the CDW transition.

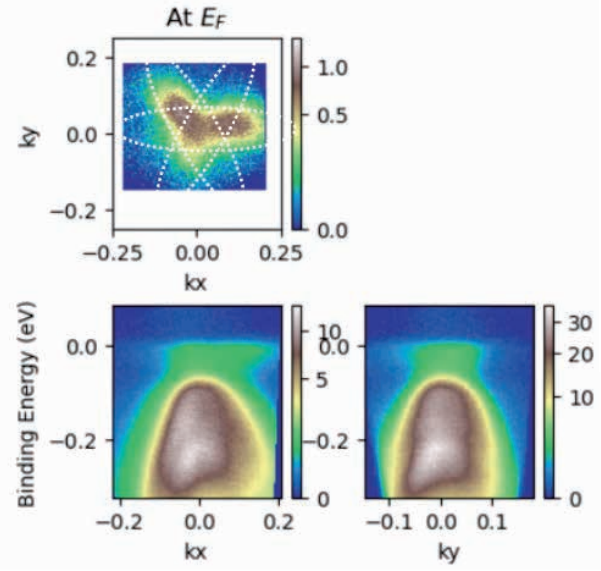

Fig. 1. ARPES spectra of $TiSe_2$ at 10K. The photon energy taken was 7eV of vertical polarization.

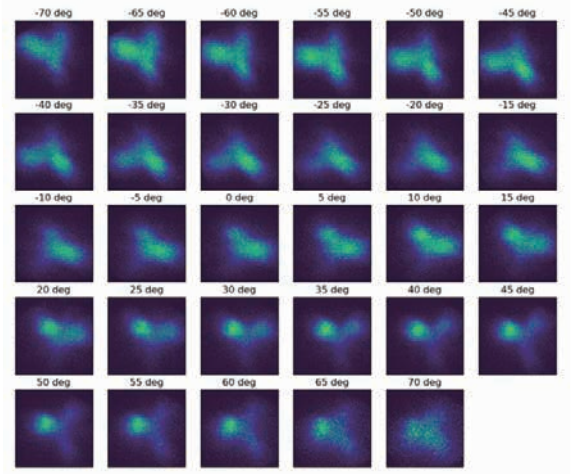

Fig. 2. ARPES intensity maps near the Fermi level as a function of the azimuth rotation. The photon of 7eV with a vertical polarization is used.

[1] S. Beaulieu *et.al.*, npj Quantum Materials **6** (2021) 93.

BL7U

Momentum Dependence of the Spectral Weight in the Single Layer High-T_c Cuprate $Bi_2Sr_2CuO_{6+\delta}$ Studied by ARPES

Y. Onishi[1], Y. Miyai[1], Y. Tsubota[1], S. Kuma[2], M. Atira[2], K. Tanaka[3], H. Eisaki[4], S. Ishida[4], K. Shimda[1,2] and S. Ideta[1,2]

[1]*Graduate School of Advanced Science and Engineering, Hiroshima Univ., Japan*
[2]*Hiroshima Synchrotron Radiation Center (HiSOR), Hiroshima Univ., Japan*
[3] *UVSOR-III Synchrotron, Institute for Molecular Science (IMS), Japan.*
[4] *National Institute of Advanced Industrial Science and Technology (AIST), Japan*

Spectral weight (SW) directly observed by angle-resolved photoemission spectroscopy (ARPES) has the information of the electronic structure which is related to the mechanism of high-transition temperature (T_c) cuprate superconductivity [1-3]. Nonetheless extensive experimental and theoretical studies have been reported, the mechanism of high-T_c cuprates have not been clear yet, why their T_c exceeds above ~40 K which cannot be explained by the BCS theory [4]. To understand the mechanism of high T_c in cuprate superconductivity, one of the essential physical parameters is superfluid density (ρ_s) which plays an important role in determining T_c and might be proportional to SW observed by ARPES [1,2,5,6]. In this study, we have performed an ARPES study to investigate the relationship between coherent spectral weights (SW) on the Fermi surface directly and T_c in cuprates, which seem to correspond to the magnitude of ρ_s and T_c [5].

We measure the electronic structure of the single-layer Bi-based high-T_c cuprate superconductor, $Bi_2Sr_2CuO_{6+d}$ (Bi2201), which has one CuO_2 layer in the unit cell and shows a high T_c of 35-40 K at optimal doping [7]. We have performed ARPES measurements systematically to directly investigate the electronic structure of the optimally doped (T_c ~ 35 K) and overdoped (T_c ~ 30 K) Bi2201. ARPES were carried out at BL7U, and temperature was set at ~10 K (< T_c) and 1.5T_c to measure the electronic structure in the superconducting and normal states, respectively. The photon energy was $h\nu$ = 17 eV. High-quality single crystals of Bi2201 were cleaved *in-situ* in the ultrahigh vacuum ~5×10^{-9} Pa.

In this study, We have clearly observed Fermi surface (FS) on Bi2201 in the *s* polarization above and below T_c. Energy distribution curves (EDCs) are symmetrized and we have estimated the Fermi momentum (k_F) on the entire FS, where the k_F is determined by minimum gap locus method. Compared with EDC in the supercondcuting and normal states, we have successfully observed difference of the spectral weight even though the nodal region in contrast with the previous study [6]. We will systematically measured doping dependence of SW in the nodal direction. From the present study, we found that the even in the nodal region which shows the zero sueprconducting gap, the nodal region should contirbute to the supercondcutivity in cuprates. As a next step ,we will measure the momentum dependence on the entire FS and discuss the distribution of SW on FS. We will also study the relationship between pseudogap and the distribution of SW.

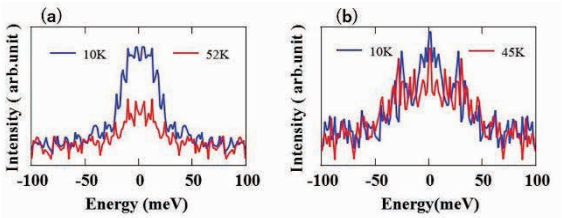

Fig. 1. Symmetrized EDC of OPT35K (a) and OD30K (b).

[1] D. L. Feng *et al*., Science **289** (2000) 277.
[2] H. Ding *et al.*, Phys. Rev. Lett. **87** (2001) 227001.
[3] K. M. Shen *et al*., Science **307** (2005) 901.
[4] W. L. McMillan, Phys. Rev. **167** (1968) 331.
[5] Y. J. Uemura *et al*., Phys. Rev. Lett. **66** (1991) 2665.
[6] T. Kondo *et al*., Nature **457** (2009) 296.
[7] A. Iyo *et al*., J. Phys. Soc. Jpn. **76** (2007) 094711.

BL7B

Excitation Spectra of Plastic Scintillators in the Vacuum Ultraviolet Region

M. Koshimizu[1], Y. Fujimoto[2] and K. Asai[3]

[1]*Research Institute of Electronics, Shizuoka University, Hamamatsu 432-8011, Japan*

[2]*Department of Applied Chemistry, Graduate School of Engineering, Tohoku University, Sendai 980-8579, Japan*

Plastic scintillators consist of host polymer and organic phosphor molecules and are widely used owing to their fast response and easy fabrication at large scale. The scintillation process in the plastic scintillators is roughly described as initial formation of ionization and electronic excitation and subsequent transfer of the excitation energy to the phosphor molecules. In the consideration of the scintillation process, we have to consider two kinds of electronic excitations: singlet and triplet states. The triplet states are formed in two processes: one is the intersystem crossing from the singlet to the triplet states, and the other is the direct formation of the triplet states upon recombination of ionization. To analyze the contribution of the latter process, we consider that the excitation in the vacuum ultraviolet (VUV) light may be a convenient tool, because the excitation by the VUV light produces ionization at higher probability with the excitation photon energy. In this study, we measured the excitation spectra of the plastic scintillators at 50–200 nm.

Plastic scintillators were fabricated using polystyrene as the host polymer and DPO and POPOP as the primary and secondary phosphors, respectively. The samples having different phosphor concentrations were fabricated. The photoluminescence spectra of the samples were obtained with VUV excitation at BL7B, UVSOR. The excitation spectra were obtained as the emission intensity in the photoluminescence spectra as functions of the excitation wavelength.

The photoluminescence spectra of the samples are presented in Figure 1. The emission bands are derived from the singlet excitation of POPOP. The spectra were similar at different excitation wavelengths. The excitation spectra of the samples with different DPO-POPOP concentrations are presented in Figures 2 and 3. The photoluminescence intensity increased and subsequently decreased as the excitation wavelength became shorter. The increase in the intensity down to 150 nm can be attributed to production of secondary excitation. The decrease in the intensity can be attributed to the enhanced probability of the triplet formation.

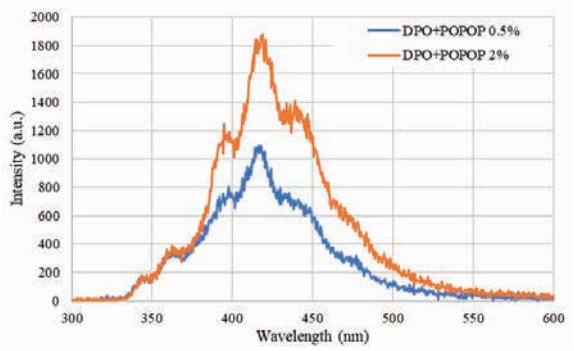

Fig. 1. Photoluminescence spectra of the plastic scintillators with excitation at 150 nm.

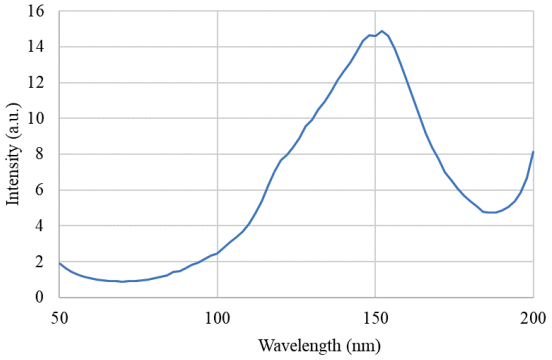

Fig. 2. Excitation spectrum of the plastic scintillators having DPO-POPOP concentration of 0.5 wt%.

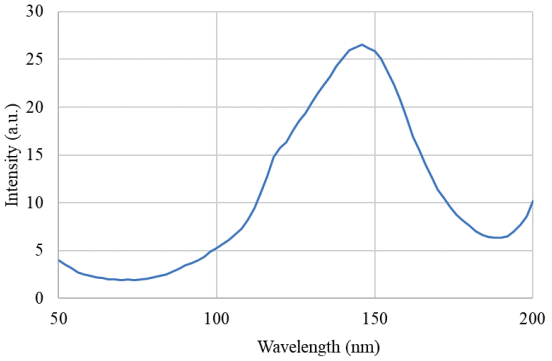

Fig. 3. Excitation spectrum of the plastic scintillators having DPO-POPOP concentration of 2 wt%.

BL7B

Mineral Analysis for Resource Exploration by Deep Ultraviolet Spectroscopy

T. Shimizu, K. Shinohara, K. Yamanoi and N. Sarukura
Institute of Laser Engineering, Osaka University, 2-6 Yamadaoka Suita, Osaka 565-0875 Japan

Vacuum ultraviolet (VUV) light has important technological applications in photochemical processing, surface treatment, optical cleaning of semiconductor substrates, and sterilization. In particular, it has been suggested that non-contact sterilization, treatment, and processing may be advanced by using VUV in the current coronavirus pandemic. To keep pace with the rapid progress in VUV research and application, it is essential to develop detectors in the short wavelength range. Conventional detectors are mainly sensitive only to visible light, and therefore VUV scintillators based on rare-earth ions and wide bandgap materials have been investigated for the detection of VUV. In our research group, we have developed scintillators with rare-earth ions doped in fluoride materials using wide bandgap materials and have achieved good results.

Currently, there is a need to develop a spectrometer for two-dimensional analysis of broadband light, which is required in the fields of industrial technology, energy, and the environment. Imaging spectroscopy is widely used for the identification of molecular species of gases and nondestructive analysis of liquids and solids, and is beginning to be applied to environmental measurements and resource surveys. In addition to the sorting by visible light imaging called color sorting, multi-wavelength imaging measurement is becoming a key to solving social problems in the future. In addition, the non-destructive nature of the measurement reduces the environmental burden, and research that integrates the humanities and sciences, such as the non-contact analysis of cultural assets, is also expected. If this imaging spectroscopic measurement can be performed in a large space, it is expected to make it possible to estimate the location of buried resources without digging, and to analyze tiles and paints on the walls of valuable old temples and shrines.

In the case of resource survey as one of the goals, the deep ultraviolet region, such as VUV, is compatible with the absorption and emission of quartz, the most common mineral on earth, for observation, and its characteristics are well represented. On the other hand, the practical application of imaging spectroscopy systems, for which technology has been accumulated in the visible light region, has not progressed due to the lack of optical elements that are compatible with non-visible light. The applicant has focused on the applicability of imaging spectroscopy measurement and has so far succeeded in developing a lens that can be applied up to deep UV, also using UVSOR [1][2]. Since the preparation of the elements around the measurement device has progressed significantly up to this point, the next step is to start evaluating the VUV properties of the actual minerals.

Typical minerals are known to exhibit fluorescence. Minerals contain a variety of impurities, which are the active factors that give rise to fluorescence. In other words, by observing fluorescence, it is possible to evaluate the quality of a mineral, making it a powerful tool for resource exploration and environmental measurement. However, fluorescence observation requires excitation in the deep ultraviolet. In this study, we used UVSOR-BL7B to demonstrate whether typical mineral impurities can be evaluated by PL (photo luminescence) spectra and PLE (photo luminescence excitation) spectra.

Fig. 1 shows the measurement results of fluorite. It is conventionally believed that europium is contained in fluorite as an impurity. The measurement data this time shows a peak that is certainly derived from europium. Although the data shown here are for general fluorite, other minerals were also analyzed in the same way, and impurities were confirmed. It was found that the deep ultraviolet analysis technique is effective for mineral evaluation. In the future, we will combine this technique with our spectroscopic technology and put it to practical use as a new technology for resource exploration and environmental measurement.

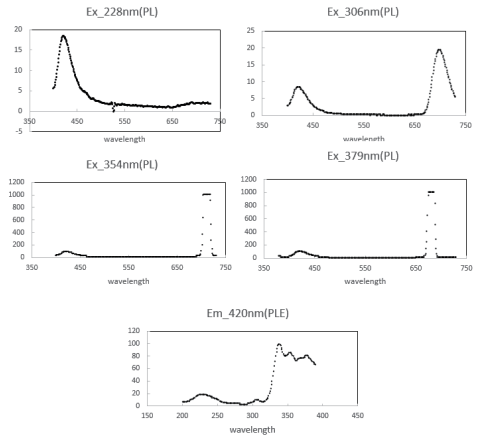

Fig. 1. PL spectra and PLE spectra of fluorite.

[1] T. Shimizu *et al.*, *UVSOR Activity Report 2019*, **47** (2020) 100.
[2] Y. Minami *et al.*, Phys. Status Solidi B, **257**(2020) 1900480.

Optical Reflectivity Study of Au-Al-Yb Quasicrystals

H. Okamura[1], A. Kamiki[1], K. Namba[2], S. Hirokawa[2] and K. Deguchi[2]
[1]*Department of Applied Chemistry, Tokushima University, Tokushima 770-8506, Japan*
[2]*Graduate School of Science, Nagoya University, Nagoya 464-8602, Japan*

Since its discovery, quasicrystals (QCs) have attracted a lot of interest for their unique properties [1]. For example, they do not have a translational symmetry in the crystal structure but show a clear rotational order in the measured diffraction pattern. Recently, Yb-containing QCs have been studied in detail [2,3], and they have revealed a singular behavior of the average Yb valence as a function of a_{6D}, a six-dimensional lattice parameter of the QC [3]. Namely, the average Yb valence of a series of Au-Al-Yb QC samples showed a sudden and steep drop, from 2.82 to 2.31, when a_{6D} of the sample was increased through a critical value of 0.74 nm by about 0.01 nm. Valence transitions or crossovers have been observed in many Yb-containing crystalline materials such as heavy fermion and intermediate-valence compounds. It is quite interesting whether or not the singular behavior of the Yb valence in QCs shares any common feature with the Yb-based heavy fermion compounds.

To investigate the interesting electronic structures of Yb-containing QCs, we have been measuring the optical reflectivity spectra [$R(\omega)$] of Au-Al-Yb QCs that show the above-mentioned valence-transition-like behavior. In our experimental method, $R(\omega)$ of a sample is measured over a wide spectral range between infrared and vacuum UV, and the Kramers-Kronig (KK) analysis is used to obtain the dielectric function $\epsilon(\omega)$ or the optical conductivity $\sigma(\omega)$ from the measured $R(\omega)$. At BL7B of UVSOR, we have measured $R(\omega)$ between 40 and 600 nm on the six samples indicated in Table 1. Note that Sample C has the critical value of a_{6D}, and that the average Yb valence rapidly decreases from Sample C to F.

Figure 1 indicates the $R(\omega)$ spectra of Samples A-F measured at room temperature. All the samples show increase of $R(\omega)$ toward longer wavelength, with an onset at around 150-200 nm. Samples C, D and E also show a clear minimum of $R(\omega)$ at 160-200 nm range. Samples A, B and F, on the other hand, do not show a clear minimum. Namely, there seems to be some qualitative difference between the two groups of samples. The difference in the onset wavelength between Samples B and C is particularly clear, although they are next to each other in Table 1. An onset of high reflectivity in a metallic compound is usually associated with the plasma frequency, and is related with the density of free electrons. However, to make a detailed analysis on the electronic structures, we need to obtain $\epsilon(\omega)$ and $\sigma(\omega)$ via the KK analysis of $R(\omega)$. To do so, we are currently extending the measurement to the infrared range, since a wide spectral range of $R(\omega)$ is required to perform a reliable KK analysis. The spectra in Fig. 1 will be connected to those in the infrared range to obtain $R(\omega)$ in a wide spectral range, and will be used for the KK analysis.

Table 1. Measured QC samples.

Sample label	Chemical formula	Average Yb valence
A	$(Au_{0.5}Cu_{0.5})_{49}Al_{34}Yb_{17}$	2.90
B	$(Au_{0.9}Cu_{0.1})_{49}Al_{34}Yb_{17}$	2.83
C	$Au_{49}Al_{34}Yb_{17}$	2.82
D	$Au_{49}(Al_{0.9}Ga_{0.1})_{34}Yb_{17}$	2.73
E	$Au_{49}(Al_{0.7}Ga_{0.3})_{34}Yb_{17}$	2.66
F	$Au_{56}Ga_{28}Yb_{16}$	2.31

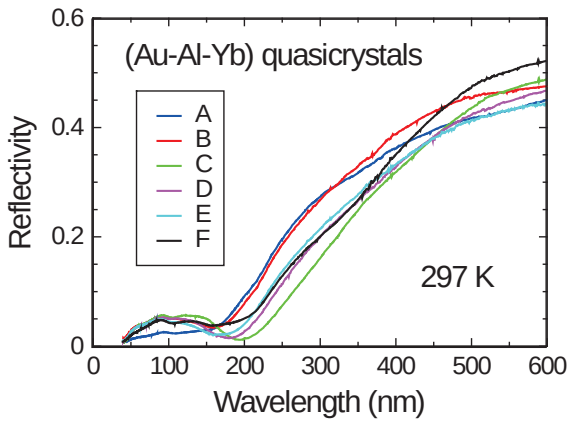

Fig. 1. Optical reflectivity spectra of Au-Cu-Yb quasicrystal samples A to F at room temperature measured at BL7B.

[1] D. Shechtman *et al.*, Phys. Rev. Lett. **53** (1984) 1951.
[2] K. Deguchi *et al.*, Nat. Mater. **11** (2012) 1013.
[3] K. Imura *et al.*, Sci. Rep. **10** (2020) 17116.

UVSOR User 4

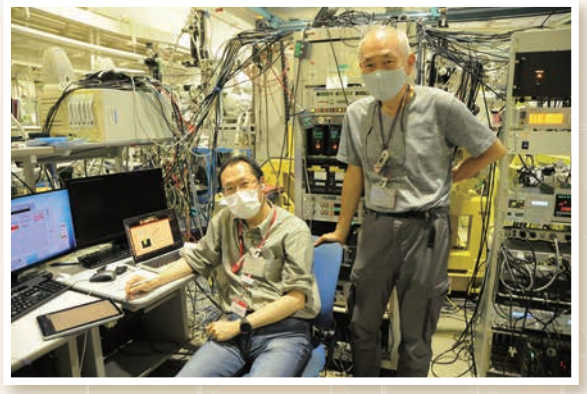

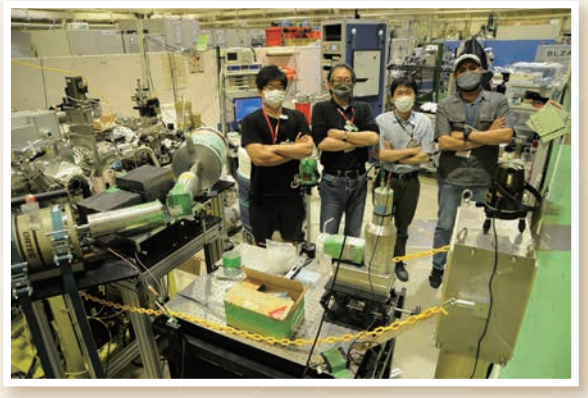

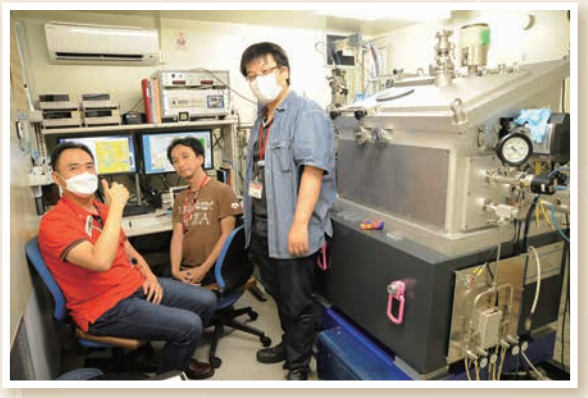

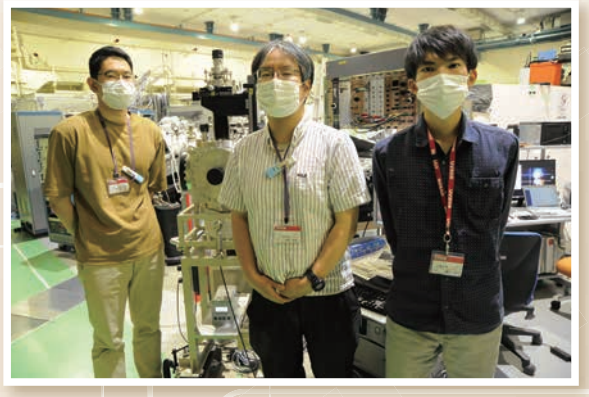

UVSOR User 5